
超微細シリコンLSIに用いられる
高誘電率薄膜中の欠陥の構造と生成機構の解明

16360160

平成16年度～18年度科学研究費補助金
[基盤研究(B)]研究成果報告書

平成19年4月

研究代表者 大木義路
早稲田大学理工学術院教授

は し が き

本報告書は下記の課題で助成を受けた平成16年度～平成18年度科学研究費補助金[基盤研究(B)(2)]に関わる研究成果をまとめたものである。

研究課題

超微細シリコンLSIに用いられる高誘電率薄膜中の欠陥の構造と生成機構の解明
課題番号 16360160

研究組織

研究代表者：大木義路（早稲田大学理工学術院教授）
研究分担者：浜義昌（早稲田大学理工学術院教授）
研究分担者：宗田孝之（早稲田大学理工学術院教授）

交付決定額（配分額）

（金額単位：円）

	直接経費	間接経費	合計
平成16年度	7,300,000	0	7,300,000
平成17年度	4,700,000	0	4,700,000
平成18年度	2,900,000	0	2,900,000
総計	14,900,000		14,900,000

研究発表

(1)学会誌等

1. T. Ito, H. Kato, T. Nango and Y. Ohki “Energy Band Profile of Hafnium Silicates Estimated by X-Ray Photoelectron Spectroscopy”, Japanese Journal of Applied Physics, Vol. 43, 8199-8202, 2004.12
2. Kwang Soo Seol, Kazuo Takeuchi, and Yoshimichi Ohki “Ferroelectricity of single-crystalline, monodispersed lead zirconate titanate nanoparticles of 9 nm in diameter”, Appl. Phys. Lett., Vol. 85, 2325-2327, 2004
3. Kristina E. Lipinska-Kalita, Yoshimichi Ohki, et al. (5名中5番目), “Temperature effects on luminescence properties of Cr³⁺ ions in alkali gallium silicate nanostructured media”, J. Appl. Phys. Vol.98,.054302-1 -.05302-6, 2005
4. Kristina E. Lipinska-Kalita, Yoshimichi Ohki, et al. (6名中6番目), “Synthesis and characterization of metal-dielectric composites with copper nanoparticles embedded in a glass matrix:A multitechnique approach”, J. Appl. Phys, Vol.98, 054301-1 -.05301-6, 2005
5. Kristina E. Lipinska-Kalita, Yoshimichi Ohki, et al. (4名中2番目), “Effects of High Pressure on Stability of the Nanocrystalline LiAlSi₂O₆ Phase of a Glass-Ceramic Composite: a Synchrotron X-Ray Diffraction Study”, Physica B Condensed Matter, No.365, 155 – 162, 2005

は し が き

本報告書は下記の課題で助成を受けた平成16年度～平成18年度科学研究費補助金[基盤研究(B)(2)]に関わる研究成果をまとめたものである。

研究課題

超微細シリコンLSIに用いられる高誘電率薄膜中の欠陥の構造と生成機構の解明

課題番号 16360160

研究組織

研究代表者：大木義路（早稲田大学理工学術院教授）

研究分担者：浜義昌（早稲田大学理工学術院教授）

研究分担者：宗田孝之（早稲田大学理工学術院教授）

交付決定額（配分額）

（金額単位：円）

	直接経費	間接経費	合計
平成16年度	7,300,000	0	7,300,000
平成17年度	4,700,000	0	4,700,000
平成18年度	2,900,000	0	2,900,000
総計	14,900,000		14,900,000

研究発表

(1)学会誌等

1. T. Ito, H. Kato, T. Nango and Y. Ohki “Energy Band Profile of Hafnium Silicates Estimated by X-Ray Photoelectron Spectroscopy”, Japanese Journal of Applied Physics, Vol. 43, 8199-8202, 2004.12
2. Kwang Soo Seol, Kazuo Takeuchi, and Yoshimichi Ohki “Ferroelectricity of single-crystalline, monodispersed lead zirconate titanate nanoparticles of 9 nm in diameter”, Appl. Phys. Lett., Vol. 85, 2325-2327, 2004
3. Kristina E. Lipinska-Kalita, Yoshimichi Ohki, et al. (5名中5番目), “Temperature effects on luminescence properties of Cr³⁺ ions in alkali gallium silicate nanostructured media”, J. Appl. Phys, Vol.98, 054302-1 -.05302-6, 2005
4. Kristina E. Lipinska-Kalita, Yoshimichi Ohki, et al. (6名中6番目), “Synthesis and characterization of metal-dielectric composites with copper nanoparticles embedded in a glass matrix: A multitechnique approach”, J. Appl. Phys, Vol.98, 054301-1 -.05301-6, 2005
5. Kristina E. Lipinska-Kalita, Yoshimichi Ohki, et al. (4名中2番目), “Effects of High Pressure on Stability of the Nanocrystalline LiAlSi₂O₆ Phase of a Glass-Ceramic Composite: a Synchrotron X-Ray Diffraction Study”, Physica B Condensed Matter, No.365, 155 – 162, 2005

6. Koichi Awazu, Yoshimichi Ohki, et al. (7名中6番目), "Fabrication of two- and three-dimensional photonic crystals of titania with sub-micrometer resolution by deep X-ray lithography", J. Vacuum Science and Technology B, Vol.23, 934-939, 2005
7. T. Ito, M. Maeda, K. Nakamura, H. Kato, and Y. Ohki, "Similarities in photoluminescence in hafnia and zirconia induced by ultraviolet photons", J. Appl. Phys., Vol.97, 054104-1 - 054104-7, 2005
8. S. Kashiwagi, Y. Hama, et al. (11名中7番目), "Compact soft x-ray source using Thompson scattering", J. Appl. Phys., Vol.98, 123302-1 - 123302-6, 2005
9. SF. Chichibu, T. Sota, et al. (11名中10番目), "Exciton-polariton spectra and limiting factors for the room-temperature photoluminescence efficiency in ZnO", Semicond. Sci. Tech., Vol. 20, S67-S77, 2005
10. T. Ito, H. Kato, T. Nango, and Y. Ohki "Improvement in electrical properties of hafnium and zirconium silicates by postnitriding", Journal of Physics: Condensed Matter, Vol. 18, 6009-6016, 2006
11. T. Ito, H. Kato, and Y. Ohki "Mechanisms of several photoluminescence bands in hafnium and zirconium silicates induced by ultraviolet photons", J. Appl. Phys., Vol. 99, 0941061-0941069, 2006
12. 及川圭太、伊藤俊秀、高瀬雅之、大木義路、加藤宙光, "プラズマ化学気相堆積により成膜した high-k 膜の X 線光電子分光", 放電研究, Vol. 49, 39-42, 2006

(2)国際学会口頭発表

1. T. Ito, M. Maeda, K. Nakamura, M. Takase, H. Kato, and Y. Ohki, "Two inherent photoluminescence bands in hafnia and zirconia", Proceedings of 4th International Symposium on Dry Process, 71-76, , 2004
2. Masato Murai, Yoshimichi Ohki, et al., "Irradiation Effects on Silica Glass by Ion Microbeam for Fabrication of Optical Elements", Proceedings of 2005 International Symposium on Electrical Insulating Materials, B3-7, 210-213, 2005

(3)出版物

なし

研究成果による工業所有権の出願・取得状況

なし

研究成果

1. 研究目的

電子デバイス用無機絶縁膜では、デバイスの微細化に伴う様々な問題が生じている。例えば、次世代 CMOS のゲート絶縁 SiO_2 膜には、1nm 以下の膜厚が要求され、リーク電流の増加やデバイスの信頼性低下という問題が生じている。これに対し、より誘電率の高い (high-k) 材料としてハフニウムシリケート ($\text{Hf}_x\text{Si}_{(1-x)}\text{O}_y$)、ハフニア (HfO_y)、ジルコニウムシリケート ($\text{Zr}_x\text{Si}_{(1-x)}\text{O}_y$)、ジルコニア (ZrO_y) などが検討されている。これらの物質の禁制帯内部に欠陥や不純物などによる局在準位が存在すれば、リーク電流、絶縁破

壊、閾値変動などの原因となる。

こうした観点から、本研究では上記 high-k 絶縁膜に対して、フォトルミネセンス (PL) を調べ、発光原因や局在準位について論じた。また、X 線光電子分光法 (XPS) によりバンドプロファイルを調べ、さらに成膜後熱処理によりリーク電流の低減を試みた。

2. 研究成果

平成 16 年度は、有力候補材料であるハフニウムシリケート ($\text{Hf}_x\text{Si}_{(1-x)}\text{O}_y$)、ジルコニウムシリケート ($\text{Zr}_x\text{Si}_{(1-x)}\text{O}_y$)、ハフニア (HfO_y)、ジルコニア (ZrO_y) をプラズマ化学気相堆積法により成膜し、フォトルミネセンス法を用いて膜中欠陥および不純物が形成するエネルギー準位を調べた。また、成膜後熱処理が電気特性に与える影響を調べた。

1. フォトルミネセンス法による膜内欠陥および不純物の解析：シンクロトロン放射 (SR) 光を用いた真空紫外域の光吸収測定より、 $\text{Hf}_x\text{Si}_{(1-x)}\text{O}_y$ ($\text{Zr}_x\text{Si}_{(1-x)}\text{O}_y$) の光学的禁制帯幅 E_{opt} は組成比 x の減少と共に HfO_y (ZrO_y) の 5.9eV (5.5eV) から SiO_y の 8.8eV まで増加することを明らかにした。SR 光励起により $\text{Hf}_x\text{Si}_{(1-x)}\text{O}_y$ 、 $\text{Zr}_x\text{Si}_{(1-x)}\text{O}_y$ 、 HfO_y 、 ZrO_y において 2.8eV にピークを持つ発光帯が観測された。この発光は基板材料によらず観測されるので、膜中からの発光であることが示された。また、この発光は原料ガス、成膜法に拘らず観測されることから、発光に寄与する禁制帯内部の局在準位の原因が不純物ではなく、試料自身に起因する内因的なものであることが示唆された。

2. 成膜後熱処理による電気特性改善： $\text{Hf}_x\text{Si}_{(1-x)}\text{O}_y$ 、 $\text{Zr}_x\text{Si}_{(1-x)}\text{O}_y$ に NO、 O_2 、 N_2 雰囲気中において成膜後熱処理を加え、処理前後のリーク電流値を比較した。両物質においてリーク電流は、NO 中熱処理により最も低減される一方、 N_2 中では増加した。ESR 測定による処理前後での電子スピン数の変化がリーク電流値の変化と良く似ていることから、ESR 観測可能なラジカル性欠陥がリーク電流の原因となると推定した。

平成 17 年度は、平成 16 年度に引き続き、有力候補材料であるハフニウムシリケート、ジルコニウムシリケート、ハフニア、ジルコニアをプラズマ化学気相堆積法により成膜し、フォトルミネセンス法 (PL) を用いて膜中欠陥および不純物が形成する禁制帯中のエネルギー準位を調べ、さらに電子スピン共鳴法 (ESR) によりラジカル性欠陥を調べた。さらに、比較試料として、単結晶かつバルク試料であるイットリア安定化ジルコニアについても同様に PL 法と ESR 法により禁制帯内のエネルギー準位とラジカル性欠陥について調べた。

1. PL 法による膜内欠陥および不純物の解析：シンクロトロン放射光を用いた PL スペクトル解析、PL 寿命測定ならびに真空紫外域の光吸収測定より、ハフニア、ジルコニア、ハフニウムシリケート、ジルコニウムシリケートに共通する PL が見られること、PL 発光の原因は、禁制帯内部の局在準位や不純物ではなく、試料自身に起因する内因的なものであることを示した。

2. イットリア安定化ジルコニアの紫外光誘起欠陥：上記試料に紫外光を照射すると、2種類の常磁性欠陥が生成され、3.3eV 付近の吸収が増加することを見出した。さらに、これらの変化は光子エネルギー依存性を持ち、4.0eV より大きいエネルギーでのみ生じることから、伝導帯の裾に励起された電子により、これらの変化が生じていることを明らかにした。

平成 18 年度は、候補材料であるハフニウムシリケート、ジルコニウムシリケート、ハフニア、ジルコニアをプラズマ化学気相堆積法、上記の一部をスピコート法より成膜した。薄膜試料は、分析機器による系統的な研究を行うのが難しいため、比較試料として、単結晶バルク試料であるイットリア安定化ジルコニア、ランタンアルミネート及びアルファアルミナも用いた。フォトルミネセンス法(PL)、電子スピン共鳴法(ESR)、光電子スペクトル法により電子状態を調べた。

1. PL 法による膜内欠陥および不純物の解析：シンクロトロン放射光を用いた PL スペクトル解析、PL 寿命測定ならびに真空紫外域の光吸収測定より、ハフニア、ジルコニア、ハフニウムシリケート、ジルコニウムシリケートに共通する PL 発光の原因は、バンド裾準位が関与した励起電子の緩和過程において生じることを明らかにした。

2. ランタンアルミネート及びアルファアルミナ単結晶の光電子スペクトルにおける化学シフトの考察：光電子スペクトル測定からアルファアルミナの酸素 1s 電子の束縛エネルギーはランタンアルミネートより 1.4eV 大きいことが分かった。この化学シフトの原因の一つと考えられる緩和エネルギーの寄与を、理論式より見積もり、化学シフト +1.4eV のうち、+1.2eV であることを明らかとした。

[3 年間の成果のまとめ]

本研究以前の研究も合わせ、シリカ、シリコンオキシナイトライド、シリコンナイトライド、ハフニウムシリケート、ジルコニウムシリケート、ハフニア、ジルコニア、ランタンアルミネート及びアルミナよりなる一連の無機絶縁性薄膜の禁制帯中局在準位および電子状態を系統的に明らかに出来たことになる。これは、所望の性質を具備した膜の堆積につながる優れた知見であると考えている。

[Abstract in English]

1. RESEARCH INSTITUTION NUMBER : 3 2 6 8 9

2. RESEARCH INSTITUTION : Waseda University

3. CATEGORY : Grant - in - Aid for Scientific Research (B)

4. TERM OF PROJECT (2004 - 2006)

5. PROJECT NUMBER : 16360160

6. TITLE OF PROJECT : Structures and Generation Mechanisms of Defects in High-k Dielectric Films for Silicon ULSIs

7. HEAD INVESTIGATOR

REGISTERED NUMBER	NAME	INSTITUTION, DEPARTMENT, TITLE OF POSITION
70103611	OHKI, Yoshimichi	Faculty of Science and Engineering, Professor

8. INVESTIGATORS

REGISTERED NUMBER	NAME	INSTITUTION, DEPARTMENT, TITLE OF POSITION
(1)40063680	HAMA, Yoshimasa	Faculty of Science and Engineering, Professor
(2)90171371	SOTA, Takayuki	Faculty of Science and Engineering, Professor

9. SUMMARY OF RESEARCH RESULTS

For the coming sub-65 nm complementary metal-oxide-semiconductor (CMOS) technology, high-k materials such as hafnia (HfO_y), hafnium silicate ($\text{Hf}_x\text{Si}_{1-x}\text{O}_y$), zirconia (ZrO_y), and zirconium silicate ($\text{Zr}_x\text{S}_{(1-x)}\text{O}_y$) are expected to take the place of SiO_2 as the basic material for gate dielectrics. However, there is a high possibility that a lot of localized states due to defects are present in the band gap of these high-k candidates. These localized states are assumed to cause various dielectric malfunctions such as high leakage current, low breakdown voltage, and threshold variation. Therefore, detailed and systematic research on the localized states is indispensable to understand the effects of the defects on electrical properties.

From this viewpoint, we have carried out basic studies on HfO_y , $\text{Hf}_x\text{Si}_{(1-x)}\text{O}_y$, ZrO_y , and $\text{Zr}_x\text{Si}_{1-x}\text{O}_y$, using photoluminescence (PL) as a common tool that can provide fundamental information about the band gap energy and localized states. X-ray photoelectron spectroscopy (XPS) analyses were also carried out to investigate the band profiles. Furthermore, the effects of postannealing on the electrical properties of the high-k materials were also studied.

Energy band profiles were investigated by XPS for amorphous hafnia and hafnium silicate films sandwiched between an evaporated Au electrode and a Si substrate. Valence band offset and conduction band offset decrease until they become almost constant with an increase in hafnium content at both Si and Au sides. In literature, similar decrease in the valence band offset was reported in zirconium silicate.

Photoluminescence spectra induced by UV photons were measured for amorphous hafnia and zirconia deposited by plasma-enhanced chemical-vapor deposition, amorphous hafnia deposited by pulse laser deposition, and crystalline yttria-stabilized zirconia (YSZ). A PL peak appears around 2.7 to 2.9 eV similarly in all hafnia and zirconia samples, irrespective of the difference in crystallinity, oxygen deficiency, source alkoxide, deposition method, or the substrate material. The decay profile of the PL is also similar in all the samples. These results indicate that the PL is inherent in hafnia and zirconia, and is not due to impurities, oxygen vacancy, or interface defects between the sample and the substrate. From PL excitation (PLE) and vacuum-ultraviolet (VUV) absorption measurements, the PL was found

to be excited by UV photons to tail states at the band edges. When the samples were annealed at 900°C, a new PL peak appears around 4.2 eV in all the samples except YSZ. The PLE and VUV absorption measurements indicate that the 4.2-eV PL is excited due to the interband absorption.

Mechanisms of PLs induced in hafnium and zirconium silicates were also discussed. A broad PL spectrum was observed from 2.0 to 5.0 eV similarly in both silicates. This PL has two components with peaks around 2.8 to 3.0 eV and 3.8 eV for hafnium silicates and those around 2.7 to 3.0 eV and 3.8 eV for zirconium silicates. Time-resolved PL and PL decay measurements indicate that the origin of the PL component around 2.7(2.8) to 3.0 eV is the same as that of the PL component around 2.7 to 2.9 eV in hafnia and zirconia. Furthermore, PLE and VUV absorption measurements show that both the PL components around 2.7(2.8) to 3.0 eV and 3.8 eV are excited to tail states at the band edges. Through these studies, it is assumed that hafnium silicate, zirconium silicate, hafnia, and zirconia have luminescent centers in their band gaps with their respective upper and lower states that have a certain fixed energy difference irrespective of the hafnium or zirconium content.

Furthermore, effects of postannealing on the electrical properties of hafnium and zirconium silicates were investigated. When the samples were postannealed in nitrogen monoxide (NO), leakage current and capacitance-voltage (C-V) hysteresis width are decreased drastically. From ESR measurement, it is assumed that paramagnetic defects at the interface between the sample and the Si substrate are responsible for the leakage current and the C-V hysteresis. Furthermore, depth profile by XPS shows that the postnitridation effectively terminates these interface defects and contributes to the improvement in electrical properties.

10. KEY WORDS

(1)gate insulator	(2)high-k dielectrics	(3)hafnium silicate
(4)zirconium silicate	(5)hafnia	(6)zirconia
(7)plasma CVD	(8)photoluminescence	

11. REFERENCES

AUTHORS , TITLE OF ARTICLE	JOURNAL, VOLUME-NUMBER,PAGES CONCERNED, YEAR
T. Ito, H. Kato, T. Nango and <u>Y. Ohki</u> "Energy Band Profile of Hafnium Silicates Estimated by X-Ray Photoelectron Spectroscopy"	Japanese Journal of Applied Physics, 2004. 12, Vol. 43, pp. 8199-8202.
T. Ito, M. Maeda, K. Nakamura, M. Takase, H. Kato, and <u>Y. Ohki</u> , "Two inherent photoluminescence bands in hafnia and zirconia"	Proceedings of 4th International Symposium on Dry Process, 2004, pp. 71-76
Kwang Soo Seol, Kazuo Takeuchi, and Yoshimichi <u>Ohki</u> "Ferroelectricity of single-crystalline, monodispersed lead zirconate titanate nanoparticles of 9 nm in diameter"	Appl. Phys. Lett., 2004, Vol. 85, pp. 2325-2327.
Kristina E. Lipinska-Kalita, <u>Yoshimichi Ohki</u> , et al., "Temperature effects on luminescence properties of	J. Appl. Phys, 2005, Vol.98, pp. 054302-1 -05302-6.

<p>Cr³⁺ ions in alkali gallium silicate nanostructured media” Kristina E. Lipinska-Kalita, <u>Yoshimichi Ohki</u>, et al., “Synthesis and characterization of metal-dielectric composites with copper nanoparticles embedded in a glass matrix: A multitechnique approach” Kristina E. Lipinska-Kalita, <u>Yoshimichi Ohki</u>, et al., “Effects of High Pressure on Stability of the Nanocrystalline LiAlSi₂O₆ Phase of a Glass-Ceramic Composite: a Synchrotron X-Ray Diffraction Study” Koichi Awazu, <u>Yoshimichi Ohki</u>, et al., “Fabrication of two- and three-dimensional photonic crystals of titania with sub-micrometer resolution by deep X-ray lithography” T. Ito, M. Maeda, K. Nakamura, H. Kato, and <u>Y. Ohki</u>, “Similarities in photoluminescence in hafnia and zirconia induced by ultraviolet photons” S. Kashiwagi, <u>Y. Hama</u>, et al., “Compact soft x-ray source using Thompson scattering” SF. Chichibu, <u>T. Sota</u>, et al., “Exciton-polariton spectra and limiting factors for the room-temperature photoluminescence efficiency in ZnO” Keita Oikawa, Toshihide Ito, Masayuki Takase, <u>Yoshimichi Ohki</u>, and Hiromitsu Kato, “X-ray photoelectron spectroscopy of high-k dielectric films synthesized by plasma-enhanced chemical-vapor deposition”,</p>	<p>J. Appl. Phys, 2005, Vol.98, pp. 054301-1 - 05301-6.</p> <p>Physica B Condensed Matter, 2005, No.365, pp. 155 – 162.</p> <p>J. Vacuum Science and Technology B, 2005, Vol.23, pp. 934-939.</p> <p>J. Appl. Phys., 2005, Vol.97, pp. 054104-1 - 054104-7.</p> <p>J. Appl. Phys., 2005, Vol.98, pp. 123302-1 - 123302-6.</p> <p>Semicond. Sci. Tech. , 2005, Vol. 20, S67-S77.</p> <p>JIEED Japan, 2006, Vol. 49, pp. 39-42</p>
--	--

研究成果の概要

次章に発表済原著論文のうち主なものを掲載する。ここでは、その概要を述べる。

(1) “Energy band profiles of hafnia and hafnium silicates estimated by x-ray photoelectron spectroscopy”では、 HfO_y および $\text{Hf}_x\text{Si}_{1-x}\text{O}_y$ を Au と *p* 型 Si でサンドウィッチした構造のバンドプロファイルを XPS により調べ、これらの膜の絶縁膜としての有望性を評価した。

アモルファスの HfO_y および組成比を系統的に変化させた $\text{Hf}_x\text{Si}_{1-x}\text{O}_y$ 膜を *p* 型 Si 基板上に成膜したのち、真空蒸着法により Au 蒸着を行い、MOS 構造を形成した。まず、XPS における $\text{O}1s$ 電子のロススペクトルから各試料の禁制帯幅 E_g を見積った。Hf の含有量 x の増加に伴い E_g は減少し、その後一定値に近づく。次に、XPS の価電子帯スペクトルより正孔に対するエネルギー障壁高さを見積り、この値と既に見積った E_g と合わせて電子に対する障壁高さを計算した。その結果、*p*-Si および Au との両界面において、電子および正孔に対する障壁高さは、 E_g と同様に x の増加に伴い一定値まで減少することを明らかにした。

これまでに ZrO_y 、 $\text{Zr}_x\text{Si}_{1-x}\text{O}_y$ について類似の結果が、XPS とオージェ電子分光に基づき報告されている。Hf と Zr は同族元素であり、バンド構造も HfO_y と ZrO_y 、あるいは $\text{Hf}_x\text{Si}_{1-x}\text{O}_y$ と $\text{Zr}_x\text{Si}_{1-x}\text{O}_y$ で良く似ていることを考慮すれば、この結果は妥当である。 HfO_y 、 $\text{Hf}_x\text{Si}_{1-x}\text{O}_y$ 、 ZrO_y 、 $\text{Zr}_x\text{Si}_{1-x}\text{O}_y$ の価電子帯上端は SiO_2 と同様に $\text{O}2p$ 電子の非結合軌道で形成されているが、 $\text{Zr}_x\text{Si}_{1-x}\text{O}_y$ において、 x の増加に伴い O 原子の配位数が増加し、 $\text{O}2p$ 軌道のエネルギー準位が上昇することが実験的に報告されている。 $\text{Hf}_x\text{Si}_{1-x}\text{O}_y$ においても同様のことが起こり、正孔に対する障壁高さが減少したと考えられる。一方、 SiO_2 の伝導帯下端は $\text{Si}3s$ 電子の反結合性軌道であるが、 HfO_y 、 ZrO_y ではそれぞれ $\text{Hf}5d$ 電子、 $\text{Zr}4d$ 電子の反結合性軌道である。これらの d 軌道は $\text{Si}3s$ 軌道よりも低エネルギー側に存在するため、組成比 x が増加すると、 d 軌道の伝導帯への寄与が増加し、電子に対する障壁高さが低下したと考えられる。High- k 絶縁膜が優れた絶縁性能を維持するには、電子・正孔に対し 1.0eV 以上のエネルギー障壁を持つ必要があるが、すべての試料について得られた値は 1.0eV よりも大きく、 HfO_y および $\text{Hf}_x\text{Si}_{1-x}\text{O}_y$ がゲート絶縁膜として有望であることが示された。

(2) “Similarities in photoluminescence in hafnia and zirconia induced by ultraviolet photons”では、 HfO_y および ZrO_y 膜で観測される紫外光誘起 PL の類似性について論じている。

試料として、 HfO_y 、 ZrO_y それぞれに対し異なる原料を用いてプラズマ化学気相堆積法により成膜された2種類のアモルファス膜、パルスレーザー堆積法により成膜されたアモルファス HfO_y 、イットリア安定化 ZrO_y (YSZ) 結晶を用意し、エキシマレーザーおよびシンクロトン放射 (SR) 光を励起光源として PL を測定した。結晶性、酸素の多寡、原料の種類、成膜方法、基板材料にかかわらず、すべての HfO_y 、 ZrO_y 膜において 2.7–2.9eV 付近に PL が観測され、単一光子計数法で測定した PL 減衰挙動も類似している。これより、この PL の原因は HfO_y 、 ZrO_y に不可避免的に内包される欠陥などであると考えられる。さらに、発光励起 (PLE) 測定と吸収測定より、この PL はバンド裾準位が関与した励起電子の緩和過程において生じることを明らかにした。さらに、900°C で熱処理を施すと、YSZ を除く試料で 4.2eV 付近に新たな PL が観測されるが、この PL はバンド間基礎吸収によって励起された電子の緩和過程において生じることを明らかにした。

上述の結果は、PL の原因として従来提唱されてきた不純物や酸素欠乏性欠陥の可能性を否定しているという意味において重要である。 HfO_y と ZrO_y とで、観測される PL が類似している主な理由は、(1) でも述べた両者のバンド構造の類似性であると考えられる。

(3) “Mechanisms of several photoluminescence bands in hafnium and zirconium silicates induced by ultraviolet photons”では、組成比の異なる $\text{Hf}_x\text{Si}_{1-x}\text{O}_y$ および $\text{Zr}_x\text{Si}_{1-x}\text{O}_y$ 膜の PL について、単一光子計数法による寿命測定と時間分解 PL 測定を併用した寿命解析などにより、発光機構を調べた。

$\text{Hf}_x\text{Si}_{1-x}\text{O}_y$ および $\text{Zr}_x\text{Si}_{1-x}\text{O}_y$ 膜に共通して、2.7–3.0eV および 3.8eV 付近に PL が観測される。寿命解析により、2.7–3.0eV 付近の PL の起源が、(2) で報告した HfO_y 、 ZrO_y 膜において観測される 2.7–2.9eV 付近の PL のものと類似していることを明らかにした。また、PLE 測定、吸収測定より 2.7–3.0eV および 3.8eV 付近の PL はともに、バンド裾準位へ励起された電子の脱励起により生じていることを明らかにした。組成比 x の増加に伴い E_g は減少する一方、これら2つの PL のピークエネルギーは変化しないことより、これらの PL に与かる準位は、Hf および Zr の含有量にかかわらず禁制帯中で一定のエネルギー差を持つことが示唆される。(1)、(2) の結果を合わせて、 HfO_y 、 $\text{Hf}_x\text{Si}_{1-x}\text{O}_y$ 、 ZrO_y 、 $\text{Zr}_x\text{Si}_{1-x}\text{O}_y$ においては、基板との界面や不純物には関連しない内因的欠陥による局在準位が禁制帯中に存在し、それらが PL の原因となっていると考えられる。

(4) “Improvement in electrical properties of hafnium and zirconium silicates by postnitriding”では、 $\text{Hf}_x\text{Si}_{1-x}\text{O}_y$ 、 $\text{Zr}_x\text{Si}_{1-x}\text{O}_y$ に成膜後熱処理を施し、電気特性の向上を試みた。

p 型 Si 基板上に成膜したアモルファス $\text{Hf}_x\text{Si}_{1-x}\text{O}_y$ および $\text{Zr}_x\text{Si}_{1-x}\text{O}_y$ に NO、 O_2 、 N_2 雰囲気において 900°C、60s の熱処理を加え、熱処理前後のリーク電流値および容量-電圧 (*C-V*) ヒステリシス幅を比較した。両物質のリーク電流は、NO 中熱処理により 1 桁以上低くなり、効果は最も顕著である。リーク電流は O_2 中熱処理でも低くなるが、 N_2 中熱処理では増加する。同じ傾向は、*C-V* ヒステリシス幅に関しても観測される。熱処理によるリーク電流およびヒステリシス幅の変化の原因を調べるために電子スピン共鳴 (ESR) 測定を行ったところ、Si-SiO₂ 界面から観測される P_b センターに類似のシグナルが観測された。熱処理前後でのこのシグナルのスピンの数の変化がリーク電流およびヒステリシス幅の変化と類似していることから、ESR 観測可能なラジカル性欠陥がリーク電流およびヒステリシス幅の原因であると考えられる。さらに、XPS の深さ方向分析により、NO 中熱処理が上述の欠陥を窒化し効果的に終端していることを明らかにした。

Outline of Important Research Results

In “Energy band profiles of hafnia and hafnium silicates estimated by x-ray photoelectron spectroscopy”, energy band profiles were investigated by XPS for amorphous hafnia and hafnium silicate films sandwiched between an evaporated Au electrode and a Si substrate. Valence band offset and conduction band offset decrease until they become almost constant with an increase in hafnium content at both Si and Au sides. In literature, similar decrease in the valence band offset was reported in zirconium silicate. This is reasonable since the two silicates have similar electronic structures. In both silicates, the highest portion of the valence band is composed of nonbonding O $2p$ states as in the cases of silica, hafnia, and zirconia, and the O-atom coordination increases with an increase in hafnium or zirconium content. According to literature, this O-atom coordination increase is responsible for the decrease in the valence band offset in zirconium silicate. Therefore, the same explanation seems possible for the decrease in the valence band offset in hafnium silicate. On the other hand, the bottom of the conduction band of silica is associated with Si $3s$ antibonding states, while that of hafnia is associated with Hf $5d$ antibonding states. The Hf $5d$ antibonding states lie below the Si $3s$ states. Therefore, the decrease in conduction band offset with an increase in the hafnium content is considered to be due to the increase in the number of Hf d -state electrons. Both the valence band offset and conduction band offset hold values higher than 1.0 eV in all the deposited samples, which indicates that they should possess a good insulating performance for a high- k dielectric material.

In “Similarities in photoluminescence in hafnia and zirconia induced by ultraviolet photons”, photoluminescence spectra induced by UV photons were measured for amorphous hafnia and zirconia deposited by plasma-enhanced chemical-vapor deposition, amorphous hafnia deposited by pulse laser deposition, and crystalline yttria-stabilized zirconia (YSZ). A PL peak appears around 2.7 to 2.9 eV similarly in all hafnia and zirconia samples, irrespective of the difference in crystallinity, oxygen deficiency, source alkoxide, deposition method, or the substrate material. The decay profile of the PL is also similar in all the samples. These results indicate that the PL is inherent in hafnia and zirconia, and is not due to impurities, oxygen vacancy, or interface defects between the sample and the substrate. From PL excitation (PLE) and vacuum-ultraviolet (VUV) absorption measurements, the PL was found to be excited by UV photons to tail states at the band edges. When the samples were annealed at 900°C, a new PL peak appears around 4.2 eV in all the samples except YSZ. The PLE and VUV absorption measurements indicate that the 4.2-eV PL is excited due to the interband absorption.

In “Mechanisms of several photoluminescence bands in hafnium and zirconium silicates

induced by ultraviolet photons”, mechanisms of PLs induced in hafnium and zirconium silicates were discussed. A broad PL spectrum was observed from 2.0 to 5.0 eV similarly in both silicates. This PL has two components with peaks around 2.8 to 3.0 eV and 3.8 eV for hafnium silicates and those around 2.7 to 3.0 eV and 3.8 eV for zirconium silicates. Time-resolved PL and PL decay measurements indicate that the origin of the PL component around 2.7(2.8) to 3.0 eV is the same as that of the PL component around 2.7 to 2.9 eV in hafnia and zirconia. Furthermore, PLE and VUV absorption measurements show that both the PL components around 2.7(2.8) to 3.0 eV and 3.8 eV are excited to tail states at the band edges. Through the above-mentioned research, it is assumed that hafnium silicate, zirconium silicate, hafnia, and zirconia have luminescent centers in their band gaps with their respective upper and lower states that have a certain fixed energy difference irrespective of the hafnium or zirconium content.

In “Improvement in electrical properties of hafnium and zirconium silicates by postnitriding”, effects of postannealing on the electrical properties of hafnium and zirconium silicates were investigated. When the samples were postannealed in nitrogen monoxide (NO), leakage current and capacitance-voltage ($C-V$) hysteresis width are decreased drastically. From ESR measurement, it is assumed that paramagnetic defects at the interface between the sample and the Si substrate are responsible for the leakage current and the $C-V$ hysteresis. Furthermore, depth profile by XPS shows that the postnitridation effectively terminates these interface defects and contributes to the improvement in electrical properties.

主な研究成果の詳細（英文）

Details of Important Research Results

Energy Band Profile of Hafnium Silicates Estimated by X-Ray Photoelectron Spectroscopy

Toshihide ITO¹, Hiromitsu KATO^{1,2,3}, Tomohiro NANGO¹ and Yoshimichi OHKI^{1,3}

¹Department of Electrical Engineering and Bioscience, Waseda University, Shinjuku-ku, Tokyo 169-8555, Japan

²Diamond Research Center, National Institute of Advanced Industrial Science and Technology, Umezono, Tsukuba-shi, Ibaraki 305-8565, Japan

³Advanced Research Institute for Science and Engineering, Waseda University, Shinjuku-ku, Tokyo 169-8555, Japan

(Received March 17, 2004; revised July 5, 2004; accepted September 9, 2004; published December 9, 2004)

Amorphous hafnium silicate films with several composition ratios were deposited on Si substrates by plasma-enhanced chemical vapor deposition, and their energy band profiles were studied by X-ray photoelectron spectroscopy. The band gap energy estimated from the energy loss spectrum of O 1s electrons decreases monotonically and then approaches a constant value with an increase in hafnium content. The valence band offset and the conduction band offset were estimated using the sample sandwiched between an evaporated Au electrode and the Si substrate. Although the two offsets decrease until they become almost constant with an increase in hafnium content at both silicate/Si and silicate/Au interfaces, they hold values higher than that necessary for a high-*k* dielectric material to maintain a good insulating performance for all the deposited silicates. [DOI: 10.1143/JJAP.43.8199]

KEYWORDS: hafnium silicate, energy band profile, band gap energy, band offset, X-ray photoelectron spectroscopy, high-*k* dielectric material, gate insulating material, plasma-enhanced chemical vapor deposition

1. Introduction

With the recent higher integration of complementary metal oxide semiconductors, even a smaller thickness is required for silicon dioxide used as a gate dielectric. Its thickness is expected to be scaled down to a value less than 1 nm in the near future.¹⁾ In this region, silicon dioxide would not maintain the insulating property, since direct tunneling dominates the leakage current.^{2–4)} In order to overcome this difficulty, several attempts of increasing the physical thickness have been carried out using materials with permittivity values higher than silicon dioxide, while keeping the equivalent thickness unchanged.^{5–9)} In this regard, many oxides such as HfO₂, ZrO₂, Ta₂O₅ and Al₂O₃, silicates such as hafnium silicate and zirconium silicate, and aluminates such as hafnium aluminate have been attracting considerable attention as promising candidates for alternative gate dielectrics.^{10–19)}

For such alternative dielectrics, a large band gap energy is desirable. However, it is generally the case that the material with a higher permittivity has a smaller band gap energy.¹²⁾ This lowers the energy barrier for conduction electrons or holes at the dielectric/metal or dielectric/semiconductor interface, which in turn increases the leakage current. From this viewpoint, the energy barrier in addition to the band gap energy must be precisely estimated for these alternative dielectrics. Considerable work has been carried out to estimate the energy barrier for HfO₂,¹³⁾ ZrO₂,^{14,15)} Ta₂O₅,¹⁶⁾ Al₂O₃,¹⁷⁾ zirconium silicate¹⁸⁾ and hafnium aluminate.¹⁹⁾ However, no work has been reported for hafnium silicate. Therefore, we have deposited hafnium silicates with several composition ratios by plasma-enhanced chemical vapor deposition (PECVD), and have examined their energy band profiles by X-ray photoelectron spectroscopy (XPS).

2. Experimental Procedures

The samples are hafnium silicate films, Hf_xSi_(1-x)O_y, deposited by PECVD. The source materials are tetraethoxysilane [TEOS: Si(OC₂H₅)₄] and a hafnium alkoxide [Hf(O-*i*-C₃H₇)₄]. Oxygen, used as a carrier and oxidation gas, was excited with an RF power of 13.56 MHz by capacitive coupling. The TEOS was vaporized and transported at 70°C

into the “tail flame” of the oxygen plasma. The TEOS flow rate was controlled with a mass-flow controller (Hitachi Metal: SFC-670). The hafnium alkoxide was vaporized and transported at 220°C into the oxygen plasma. Argon was used as a carrier and diluent gas for the alkoxide vapor and its flow rate was controlled with a mass-flow controller (Brooks 5850TR). A silicon (100) monocrystal wafer was used as a substrate. The substrate temperature was kept constant at 400°C during the deposition. No postdeposition annealing was given to the samples.

The elemental composition of the sample was examined by XPS (JEOL JPS-9010TR) using standard Mg K α X-rays with an energy of 1253.6 eV, while the thickness was measured by ellipsometry (ULVAC ESM-1) at a wavelength of 632.8 nm. In order to examine the energy band profile, XPS spectra were obtained using monoenergetic Al K α X-rays with an energy of 1486.6 eV. The band gap energy was estimated from the energy loss spectrum of O 1s electrons. Furthermore, the conduction band offset and the valence band offset were estimated using the samples with the structure shown in Fig. 1. The left half has a metal-insulator-semiconductor structure composed of an evaporated Au electrode, the hafnium silicate and the Si substrate, while the right half consists of the hafnium silicate and Si.

3. Results and Discussion

Table I shows the names of the deposited samples, their deposition conditions and their elemental compositions measured by XPS. Hafnium silicates with various compositions were successfully deposited. Hereafter, the samples are named after their hafnium contents. Namely, sample H40 means that it is hafnium silicate with the formula

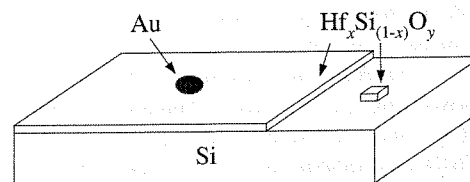


Fig. 1. Sample structure used to examine the energy band profile.

Table I. Deposition conditions and elemental ratios of the deposited films.

Sample	Deposition condition	Elemental ratio (atomic %)			$\text{Hf}_x\text{Si}_{(1-x)}\text{O}_y$	
		Hf	Si	O	x	y
S	T ^{a)}	—	33	67	0	2.0
H06	HA ^{b)} , T	1.8	30	69	0.06	2.2
H27	HA, T	8.6	23	68	0.27	2.2
H40	HA, T	13	19	69	0.40	2.2
H75	HA, T	26	8.0	66	0.75	1.9
H87	HA, T	31	5.0	65	0.87	1.9
H	HA	34	—	66	1.0	2.0

a) T: TEOS

b) HA: hafnium alkoxide

$\text{Hf}_{0.40}\text{Si}_{0.60}\text{O}_{2.2}$. From the ellipsometry measurements, it was found that the sample thickness was around 90 nm. No crystalline peaks appeared in X-ray diffraction spectra, which indicates that the present samples are amorphous. No apparent peaks related to impurities were observed in XPS spectra, except for that due to C 1s electrons. In order to examine whether the detected C 1s peak really originates from the samples, yttria-stabilized zirconia, which is believed to be totally carbon-free by its synthesis method, was analyzed by XPS. It was found that the carbon contents of the present samples were lower than that of the zirconia. This result indicates that the carbon-related XPS signal does not originate from the samples.

Figure 2 shows the energy loss spectrum of O 1s electrons observed in sample H40. The onset of the loss peak indicated by the arrow corresponds to the band gap energy E_g .^{16,20)} Therefore, E_g of this sample is estimated to be 6.38 eV. By carrying out similar observations for all the samples, the dependence of E_g on the hafnium content x was obtained as shown in Fig. 3. E_g decreases monotonically with an increase in x up to $x = 0.75$ and then remains almost constant. The decrease in E_g is reasonable since E_g of HfO_2 is far lower than that of SiO_2 .²¹⁾ Furthermore, the E_g values of samples S and H are lower than those reported for

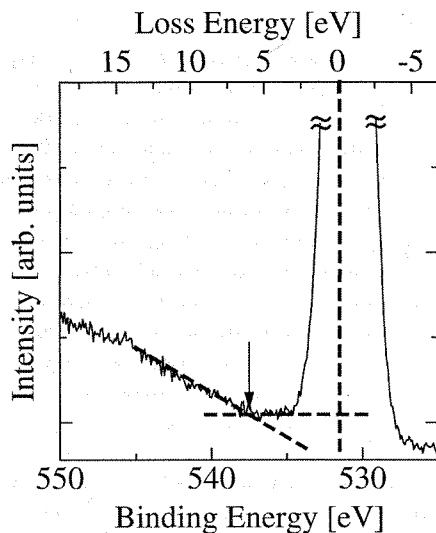


Fig. 2. Energy loss spectrum of O_{1s} electrons observed in sample H40. The arrow indicates the onset of the loss increase.

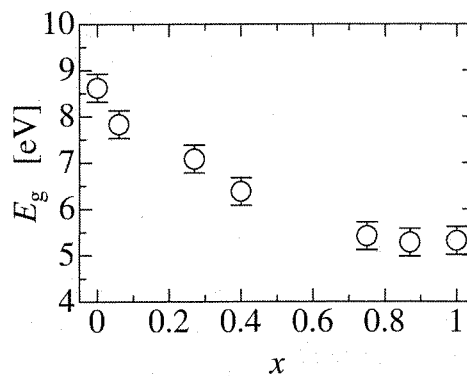


Fig. 3. Band gap energy (E_g) estimated from the XPS analysis as a function of the composition x .

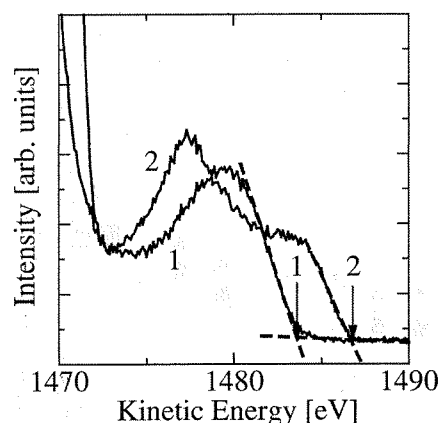


Fig. 4. XPS valence band spectra for H40 (curve 1) and H40/Si (curve 2). Arrows 1 and 2 indicate the onsets of the curves 1 and 2, respectively. Broken lines are drawn as guides for the eyes.

crystal SiO_2 and HfO_2 , 8.9 eV²²⁾ and 5.7 eV,²³⁾ respectively. This is conceivable if we take account of the fact that the present samples are amorphous with considerable structural randomness.

Figure 4 shows the XPS spectra obtained for sample H40 at the right portion of the structure shown in Fig. 1. Curve 1 represents the spectrum obtained from the silicate (H40), while curve 2 represents that obtained by irradiating the silicate and the Si substrate simultaneously with X-rays. The horizontal axis or the kinetic energy of electrons was calibrated by matching the Hf 4f peaks of the two curves, the shoulders of which are seen on the left corners, exactly at the same position. Although curve 2 mainly consists of the spectrum from the Si substrate, it also contains that from the silicate. Therefore, the difference in onset energy at which the spectrum begins to increase between curves 1 and 2 corresponds to the valence band offset or the difference in energy at the top of the valence band between the silicate and the Si substrate. The valence band offset is thus estimated to be 3.06 eV for this sample H40.

Based on the obtained values of E_g and valence band offset, the conduction band offset of sample H40 was calculated to be about 2.20 eV by assuming 1.12 eV for the gap energy of Si. In this manner, the energy band profile for the present H40/Si system can be estimated as shown in

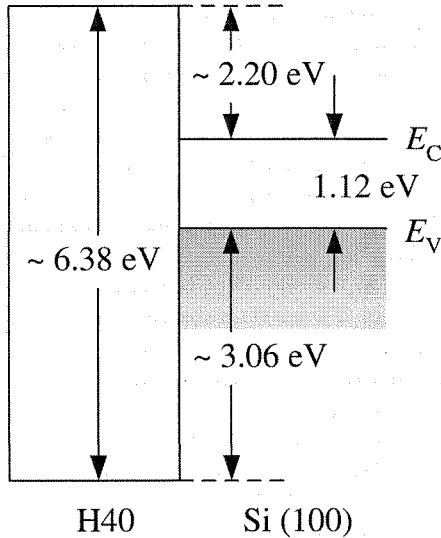


Fig. 5. Energy band profile for H40/Si.

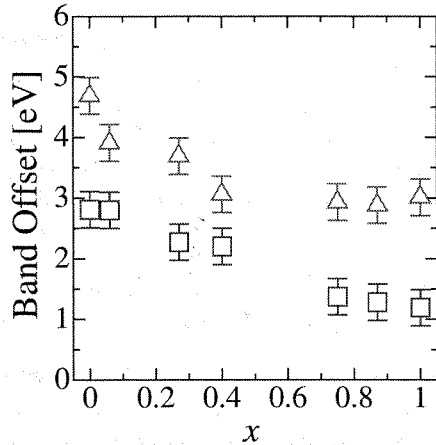


Fig. 6. Energy offsets for the conduction band (squares) and for the valence band (triangles) at the silicate/Si interface, each as a function of the hafnium content x .

Fig. 5. Figure 6 shows the energy offsets at the silicate/Si interfaces for the conduction band and for the valence band, each as a function of the hafnium content x . Both offsets decrease with an increase in hafnium content until they become almost constant at the contents x higher than 0.75.

Similar observations were performed for silicate/Au using the left portion of the structure shown in Fig. 1. Curves 1 and 2 in Fig. 7 show the XPS spectra obtained for H40 and H40/Au, respectively. While the peak around 1480 eV seen in curve 1 corresponds to the maximum in the valence band spectrum of H40, two peaks seen in curve 2 correspond to the maxima in the valence band spectra of H40 and Au. As in the case of Fig. 4, the difference between the onset energies of curves 1 and 2 represents the valence band offset between H40 and Au. The valence band offset is thus estimated to be 3.42 eV. Similarly to the case of H40/Si, the conduction band offset of H40/Au was calculated to be about 2.96 eV. Figure 8 shows the energy offsets at the silicate/Au interfaces for the conduction band and for the

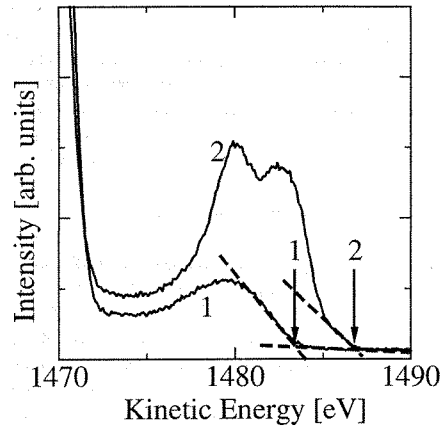


Fig. 7. XPS valence band spectra for H40 (curve 1) and H40/Au (curve 2). Arrows 1 and 2 indicate the onsets of curves 1 and 2, respectively. Broken lines are drawn as guides for the eyes.

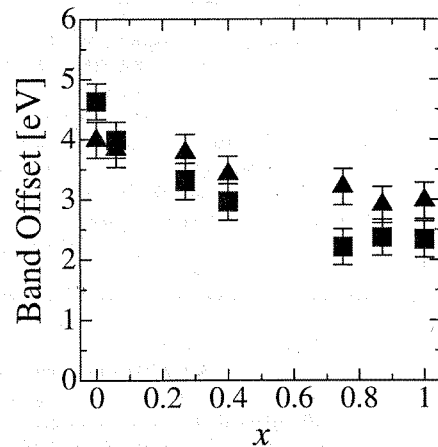


Fig. 8. Energy offsets for the conduction band (squares) and for the valence band (triangles) at the Au/silicate interface, each as a function of the hafnium content x .

valence band, each as a function of the hafnium content x . The valence band offset and the conduction band offset decrease with an increase in hafnium content in a manner very similar to those at the silicate/Si interfaces.

It has been shown experimentally that the valence band offset of zirconium silicate decreases as the zirconium content increases.^{18,24} This result is similar to the present result for hafnium silicate. This is reasonable since the electronic structures of the two silicates are similar.¹¹ In both zirconium and hafnium silicates, the highest portion of the valence band is composed of nonbonding O $2p$ states as in the cases of SiO_2 , HfO_2 and ZrO_2 ,^{11,18,25} and the O-atom coordination increases with an increase in Hf or Zr content.²⁶ This O-atom coordination increase is reported to be responsible for the decrease in valence band offset in zirconium silicate.¹⁸ Furthermore, the valence band offset of zirconium silicate, which shows a monotonic decrease as the zirconium content x increases, approaches a constant value when x becomes larger than about 0.8.¹⁸ This change to a constant offset value is ascribed to a discrete increase in O-atom coordination due to the change of the bonding form

from dative to ionic.¹⁸⁾ If the O-atom coordination changes similarly in hafnium silicate, the same explanation seems possible for the changes in valence band offset shown in Figs. 6 and 8.

On the other hand, the bottom of the conduction band of SiO₂ is associated with Si 3s antibonding states, while that of HfO₂ is associated with Hf 5d antibonding states.^{11,25)} The Hf 5d antibonding states lie below the Si 3s states.^{11,25)} Therefore, the decrease in conduction band offset with an increase in x is considered to be due to the increase in the number of Hf d -state electrons. When x is higher than 0.75, it seems that the bottom of the conduction band is fully formed by the Hf d -states, resulting in a constant conduction band offset. Moreover, since both conduction band offset and valence band offset approach their respective constant values, E_g also approaches a constant value as shown in Fig. 3 when x becomes larger than 0.75.

In order to maintain a good insulating performance for a high- k dielectric material, both conduction band offset and valence band offset must be higher than 1.0 eV.²¹⁾ Figures 6 and 8 show that all the silicates examined in the present work pass the above criteria.

4. Conclusion

The band profiles of hafnium silicates deposited by PECVD were examined. All the values of the band gap energy, valence band offset and conduction band offset decrease monotonically and then become constant with an increase in hafnium content. However, both valence band offset and conduction band offset still hold values higher than 1.0 eV in all the deposited silicates. This result indicates that the silicates deposited should possess a good insulating performance for a high- k dielectric material.

Acknowledgments

This work was partly supported by Grants-in-Aid from the Japan Society for the Promotion of Science (JSPS) for JSPS Fellows (No. 1205733) and for Scientific Research (B) (No. 12450132). A High-Tech Research Grant from the Ministry of Education, Culture, Sports, Science and Technology of Japan is also appreciated.

- 1) International Technology Roadmap for Semiconductors, International Sematech (2002).
- 2) D. A. Muller, T. Sorsch, S. Morrio, F. H. Baumann, K. E. Lutterodt and G. Timp: *Nature* **399** (1999) 758.
- 3) J. H. Stathis and D. J. DiMaria: *International Electron Device Meeting Tech. Dig.* (1998) p. 167.
- 4) B. Brar, G. D. Wilk and A. C. Seabaugh: *Appl. Phys. Lett.* **69** (1996) 2728.
- 5) G. D. Wilk, R. M. Wallace and J. M. Anthony: *J. Appl. Phys.* **87** (2000) 484.
- 6) G. D. Wilk and R. M. Wallace: *Appl. Phys. Lett.* **76** (2000) 112.
- 7) B. H. Lee, L. Kang, R. Nieh, W. J. Qi and J. C. Lee: *Appl. Phys. Lett.* **76** (2000) 1926.
- 8) W. J. Qi, R. Nieh, B. H. Lee, L. Kang, Y. Jeon, K. Onishi, T. Ngai, S. Banerjee and J. C. Lee: *International Electron Device Meeting Tech. Dig.* (1999) p. 145.
- 9) Y. H. Wu, M. Y. Yang, A. Chin, W. J. Chen and C. M. Kwei: *IEEE Electron Device Lett.* **21** (2000) 341.
- 10) M. A. Quevedo-Lopez, M. El-Bouanani, R. M. Wallace and B. E. Gnade: *J. Vac. Sci. & Technol. A* **20** (2002) 1891.
- 11) N. Ikarashi and K. Manabe: *J. Appl. Phys.* **94** (2003) 480.
- 12) A. Kawamoto, K. Cho, P. Griffin and R. Dutton: *J. Appl. Phys.* **90** (2001) 1333.
- 13) W. J. Zhu, T. P. Ma, T. Tamagawa, J. Kim and Y. Di: *IEEE Electron Device Lett.* **23** (2002) 97.
- 14) S. Miyazaki, M. Narasaki, M. Ogasawara and M. Hirose: *Microelectron. Eng.* **59** (2001) 373.
- 15) S. Miyazaki, M. Narasaki, M. Ogasawara and M. Hirose: *Solid-State Electron.* **46** (2002) 1679.
- 16) S. Miyazaki: *Appl. Surf. Sci.* **190** (2002) 66.
- 17) S. Miyazaki: *J. Vac. Sci. & Technol. B* **19** (2001) 2212.
- 18) G. Lucovsky, G. B. Rayner Jr., Y. Zhang, C. C. Fulton, R. J. Nemanich, G. Appel, H. Ade and J. L. Whitten: *Appl. Surf. Sci.* **212–213** (2003) 563.
- 19) H. Y. Yu, M. F. Li, B. J. Cho, C. C. Yeo, M. S. Joo, D. L. Kwong, J. S. Pan, C. H. Ang, J. Z. Zheng and S. Ramanathan: *Appl. Phys. Lett.* **81** (2002) 376.
- 20) H. Kato, T. Nango, T. Miyagawa, T. Katagiri, K. S. Seol and Y. Ohki: *J. Appl. Phys.* **92** (2002) 1106.
- 21) J. Robertson: *J. Vac. Sci. & Technol. B* **18** (2000) 1785.
- 22) R. B. Laughlin: *Phys. Rev. B* **22** (1980) 3021.
- 23) G. D. Wilk, R. M. Wallace and J. M. Anthony: *J. Appl. Phys.* **89** (2001) 5243.
- 24) G. Lucovsky, J. L. Whitten and Y. Zhang: *Solid-State Electron.* **46** (2002) 1687.
- 25) R. S. Johnson, J. G. Hong, C. Hinkle and G. Lucovsky: *J. Vac. Sci. & Technol. B* **20** (2002) 1126.
- 26) G. Lucovsky: *J. Vac. Sci. & Technol. A* **19** (2001) 1553.

Similarities in photoluminescence in hafnia and zirconia induced by ultraviolet photons

Toshihide Ito,^{a)} Motohiro Maeda, and Kazuhiko Nakamura

Department of Electrical Engineering and Bioscience, Waseda University, Shinjuku-ku, Tokyo 169-8555, Japan

Hiroimitsu Kato

Diamond Research Center, National Institute of Advanced Industrial Science and Technology, Umezono, Tsukuba-shi, Ibaraki 305-8565, Japan

Yoshimichi Ohki

Department of Electrical Engineering and Bioscience, Waseda University, Shinjuku-ku, Tokyo 169-8555, Japan

(Received 4 August 2004; accepted 2 December 2004; published online 14 February 2005)

Photoluminescence (PL) spectra induced by ultraviolet photons were measured for amorphous hafnia and zirconia deposited by plasma-enhanced chemical-vapor deposition (PECVD), amorphous hafnia deposited by pulse laser deposition, and crystalline yttria-stabilized zirconia. Two kinds of samples were prepared for both hafnia and zirconia deposited by PECVD using different source alkoxides in different deposition chambers. A PL peak was observed around 2.8 eV similarly in all hafnia and zirconia samples, irrespective of the difference in crystallinity, oxygen deficiency, source alkoxide, deposition method, or the substrate material. The decay profile of this PL is also similar in all the samples. These facts clearly show that neither impurities, oxygen vacancy, nor defects at the interface between the sample and the substrate are responsible for the PL. It is a luminescence inherent in hafnia and zirconia and is most likely due to radiative recombination between localized states at the band tails. When the samples were annealed in oxygen, a new PL peak appeared around 4.2 eV in all the amorphous samples. Its decay profile is also in common with these samples. Vacuum-ultraviolet absorption measurements and PL excitation measurements indicate that the 4.2-eV PL is excited due to the interband absorption. © 2005 American Institute of Physics. [DOI: 10.1063/1.1856220]

I. INTRODUCTION

It is commonly recognized that the thickness of the silicon dioxide or silica as a gate dielectric for complementary metal-oxide-semiconductor devices will be scaled down in near future to a value below its thinnest limit, where the direct tunneling dominates the leakage current.¹⁻⁴ Therefore, materials with higher permittivities are required in order to maintain a proper thickness of the gate dielectric.⁵⁻⁹ The candidates are oxides, silicates, and aluminates, such as hafnia,¹⁰⁻¹² zirconia,^{11,13,14} tantala,^{15,16} alumina,^{17,18} hafnium silicate,¹⁹⁻²¹ zirconium silicate,¹⁹⁻²² hafnium silicon oxynitride,²³ and hafnium aluminate.^{24,25} However, there is a high possibility that a lot of localized states due to defects are present in the band gap of these materials.^{26,27} These localized states are assumed to cause leakage current.²⁸ From this viewpoint, detailed and systematic studies on the localized states are indispensable to understand the effects of the defects on electrical properties.

We have shown that photoluminescence (PL) is a very effective method to examine the localized states present in insulating materials, such as bulk and thin-film silica,²⁹ silicon nitride,^{30,31} and silicon oxynitride.^{31,32} In the present research, we apply the PL method to hafnia and zirconia syn-

thesized with various methods and their PL spectra, PL excitation (PLE) spectra, and PL decay profiles are compared. As a result, it has become clear that hafnia and zirconia have very similar PL characteristics regardless of the synthesizing methods.

II. EXPERIMENTAL PROCEDURES

The samples examined are hafnia (HCA, HCB, and HP) and zirconia (ZCA, ZCB, and ZY), as listed in Table I. The samples HCA and HCB were deposited by plasma-enhanced chemical-vapor deposition (PECVD) using $\text{Hf}(\text{O}-i\text{-C}_4\text{H}_9)_4$ and $\text{Hf}(\text{O}-i\text{-C}_3\text{H}_7)_4$, respectively, as source hafnium alkoxides, while ZCA and ZCB were deposited similarly by PECVD using $\text{Zr}(\text{O}-t\text{-C}_4\text{H}_9)_4$ and $\text{Zr}(\text{O}-i\text{-C}_3\text{H}_7)(\text{C}_{11}\text{H}_{19}\text{O}_2)_3$, respectively. Oxygen, used as an oxidation gas, was excited with a rf power of 13.56 MHz through capacitive coupling. For HCA and ZCA, the alkoxide was vaporized and transported at 150 °C into the oxygen plasma by controlling its flow rate with a mass-flow controller. In about 20 min, an amorphous film about 100 nm thick was deposited on a substrate when the substrate temperature was kept constant at 500 °C. The substrate used was a *p*-type Si monocrystal wafer, unless otherwise stated. For HCB and ZCB, the alkoxide was vaporized and transported at 220 °C into the oxygen plasma

^{a)}Electronic mail: prince@suou.waseda.jp

TABLE I. Samples examined, their elemental compositions, and synthesis methods.

Name	Composition	Synthesis method	Thickness (nm)
HCA	$a\text{-HfO}_{1.39}$	PECVD	88
HCB	$a\text{-HfO}_{1.43}$	PECVD	130
HP	$a\text{-HfO}_{1.10}$	PLD	1.1×10^3
ZCA	$a\text{-ZrO}_{1.77}$	PECVD	130
ZCB	$a\text{-ZrO}_{2.13}$	PECVD	98
ZY	$c\text{-Y}_{0.20}\text{Zr}_{0.80}\text{O}_{1.68}$	Yttria-stabilized zirconia	4.5×10^5

Note: a : amorphous, c : crystalline, and source alkoxides: $[\text{Hf}(\text{O}-i\text{-C}_4\text{H}_9)_4]$ for HCA, $[\text{Hf}(\text{O}-i\text{-C}_3\text{H}_7)_4]$ for HCB, $[\text{Zr}(\text{O}-i\text{-C}_4\text{H}_9)_4]$ for ZCA, and $[\text{Zr}(\text{O}-i\text{-C}_3\text{H}_7)(\text{C}_{11}\text{H}_{19}\text{O}_2)_3]$ for ZCB.

using argon as a carrier and diluent gas. In about 40 min, an amorphous 100-nm-thick film was deposited on the substrate at 400 °C.

The sample HP was deposited on a SiO_2 substrate at 200 °C with a pulse laser deposition (PLD) method by irradiating KrF excimer laser photons onto a hafnia target. The deposited film is amorphous with a thickness of about 1.1 μm . The sample ZY is an yttria-stabilized zirconia (100) crystal plate, about 0.45 mm thick with both sides polished, and was synthesized by Nakazumi Crystal Laboratory.

Using synchrotron radiation (SR) under multibunch operation at the BL1B line of UVSOR Facility (Institute for Molecular Science, Okazaki, Japan, beam energy: 750 MeV) or an ArF excimer laser (photon energy: 6.4 eV, pulse width: ca 25 ns, power: ca 150 mJ/pulse, and pulse repetition frequency: 1 Hz, Lambda Physik Compex 205) as a photon source, PL, PLE, and vacuum-ultraviolet (VUV) absorption spectra were measured. The PL decay characteristics were measured by a single-photon counting method using SR under single-bunch operation (SR duration: ~ 400 ps and interval: 176 ns). The PL, PLE, and PL decay were measured at the liquid-helium temperature, while VUV absorption spectra were measured at room temperature. These PL characteristics were also obtained for the samples postannealed at various temperatures for 10–20 min in a rapid thermal annealing apparatus filled with oxygen gas at a pressure of $\sim 1.0 \times 10^5$ Pa.

In order to study the elemental composition, the samples were examined by x-ray photoelectron spectroscopy (XPS) (JEOL JPS-9010TR or JEOL JPS-90MX) using $\text{Mg } K\alpha$ ($h\nu = 1253.6$ eV) x rays. Furthermore, only the sample ZY was examined by x-ray fluorescence (XRF) spectroscopy (RIX-2100) and electron probe microanalysis (EPMA) (JEOL JAX-8600), since the other samples were too thin for XRF and EPMA. The thickness was measured by ellipsometry (ULVAC ESM-1) at a wavelength of 632.8 nm.

III. RESULTS AND DISCUSSION

Figures 1, 2(a), and 2(b) show the XPS O 1s, Hf 4f, and Zr 3d photoelectron spectra, respectively. By integrating these spectral areas, the samples except ZY were found to be represented by the formula HfO_x or ZrO_x with the elemental compositions shown in Table I. As for ZY, the yttrium content was estimated by the XPS Y 3d spectrum, and the values of x and y of the formula $\text{Y}_x\text{Zr}_{1-x}\text{O}_y$ were decided, as shown

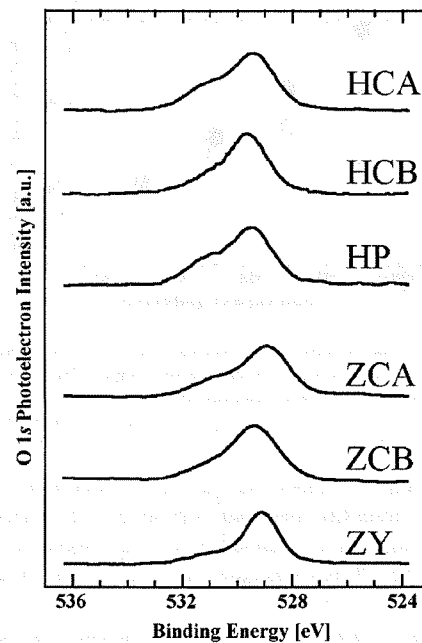


FIG. 1. O 1s photoelectron spectra obtained for the samples.

in Table I. Furthermore, from XPS C 1s spectra, the carbon content was estimated to be fairly high in all the samples. However, XPS measures only the surface layer as thin as ~ 5 nm. Therefore, it is most likely that the carbon is only abundant at the sample surface. In order to confirm this, ZY was analyzed by XRF and EPMA, which measure the

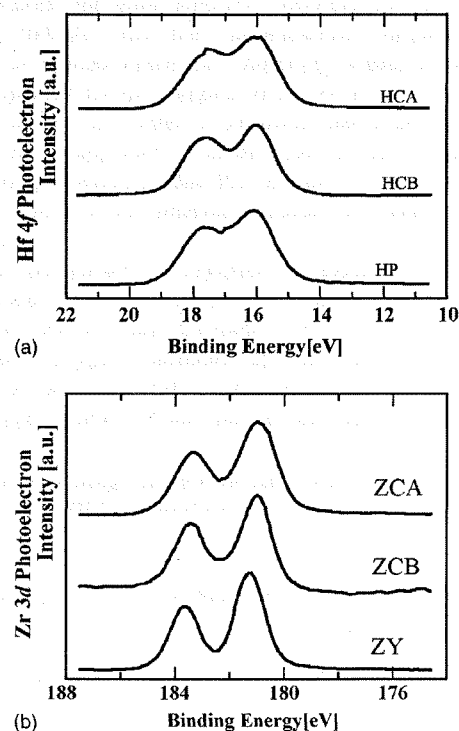


FIG. 2. Hf 4f photoelectron spectra obtained for HCA, HCB, and HP (a) and Zr 3d photoelectron spectra obtained for ZCA, ZCB, and ZY (b).

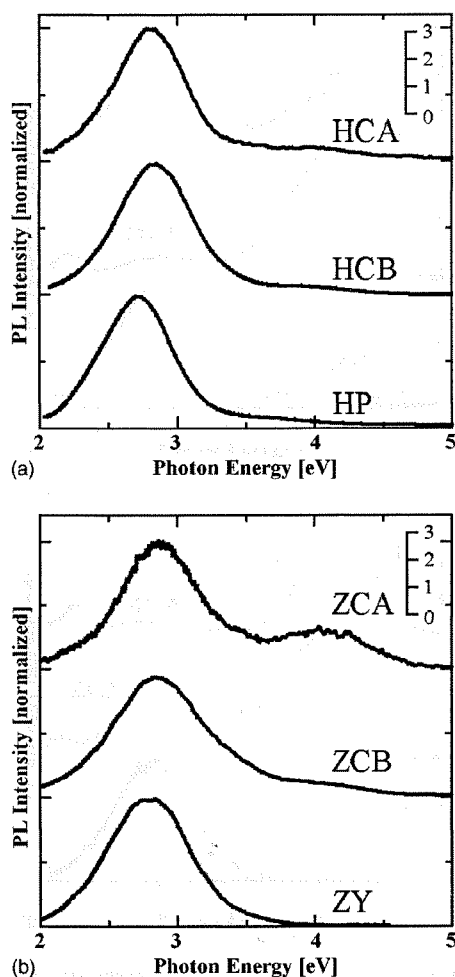


FIG. 3. PL spectra induced by 6.0-eV photons in HCA, HCB, and HP (a) and those induced by 6.4-eV photons in ZCA, ZCB, and ZY (b).

sample as deep as $\sim 1 \mu\text{m}$ and no carbon was detected by the two methods. This means that the carbon detected by XPS was not present inside the sample. It was on the sample surface and/or on the wall of the XPS sample chamber as a contaminant. As clearly shown in Table I, the samples studied in the present research have a wide variation in many respects; amorphous and crystalline, thin and thick, oxygen surplus and deficient, and different synthesizing methods.

Figure 3(a) shows the PL spectra induced in the samples HCA, HCB, and HP by the irradiation of SR photons at 6.0 eV. The measured intensity of a PL peak generally depends on various hardly controllable factors, such as a subtle difference in the mutual angles among the photon source, the sample, and the detector. This sometimes makes it difficult to compare the PL intensities among different samples. Therefore, in Fig. 3 and subsequent figures, except for Fig. 4, the PL intensity is shown after being normalized by the highest peak height. The samples HCA, HCB, and HP have a PL peak around 2.8 eV, which is hereafter referred to as PL β_H . When the PL measurements were repeated, the spectrum almost coincided with the previous ones. This indicates that the PL measurements were reproducible with a fluctuation smaller than 10 meV. The peak energy and full width at half

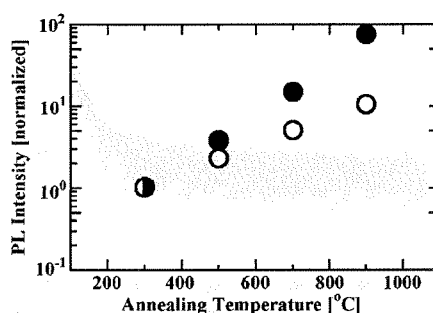


FIG. 4. Change in PL intensity around 4.2 eV with the annealing temperature observed in HCA (open circles) and ZCA (solid circles). Note that the PL intensity was normalized by the intensity observed in the samples treated at 300 °C for both HCA and ZCA.

maximum (FWHM) of PL β_H are listed in Table II for the three samples. It is clear that the many different points seen among the samples give no influences on the shape and peak energy of PL β_H . This in turn suggests that PL β_H is intrinsic to hafnia.

Figure 3(b) shows the PL spectra induced in the samples ZCA, ZCB, and ZY by 6.4-eV photons. A PL peak, which looks similar to PL β_H , is seen in all the three samples. The peak energy and FWHM of this PL listed in Table II show that these values are in common with PL β_H . Therefore, this PL is hereafter referred to as PL β_Z . That the values of peak energy and FWHM of PL β_Z agree with each other among the samples ZCA, ZCB, and ZY indicates that PL β_Z is independent of the difference in source alkoxide or deposition method, similar to the case of PL β_H . This indicates that the PLs β_H and β_Z are inherent PL bands in hafnia and zirconia. Furthermore, the good similarity between the two PLs β_H and β_Z indicates that their luminescence mechanisms are similar or basically identical. Moreover, similar experiments were repeated for the samples HCA, HCB, ZCA, and ZCB using CaF₂ crystal plates as substrates and exactly the same PL β_H or β_Z appeared as in the cases of the Si substrates. This strongly indicates that PLs β_H and β_Z are certainly not due to defects at the interface between the sample and the substrate.

Previous papers³³⁻³⁶ reported the appearance of a broad PL around 2.7 eV and a small PL around 2.0 eV in yttria-stabilized zirconia and attributed the former PL to yttria-associated oxygen vacancies and the latter to Pr³⁺ and Tb³⁺.³⁶ As shown in Table I, the present samples have various oxygen contents, from oxygen deficient to oxygen sur-

TABLE II. Peak energies and FWHM values of PLs β_H and β_Z .

Sample	PL β_H or β_Z	
	Peak energy (eV)	FWHM (eV)
HCA	2.8	0.7
HCB	2.8	0.7
HP	2.7	0.7
ZCA	2.9	0.7
ZCB	2.9	0.8
ZY	2.8	0.7

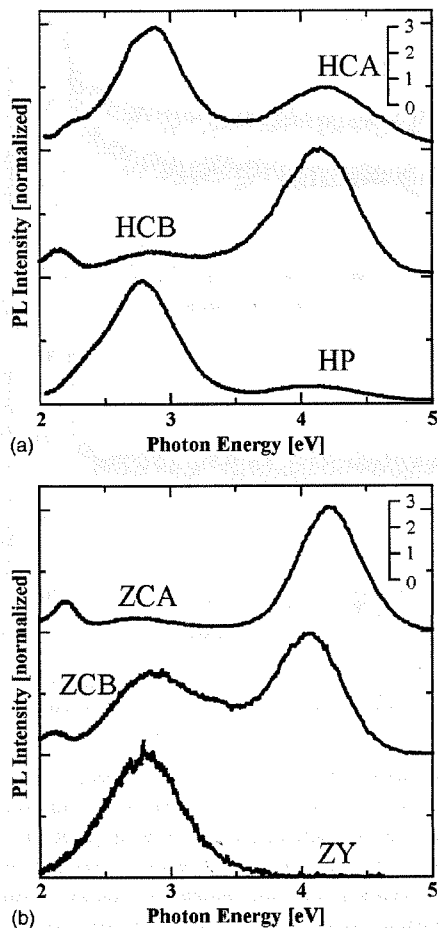


FIG. 5. PL spectra induced by 6.0-eV photons in HCA, HCB, and HP (a) and those induced by 6.4-eV photons in ZCA, ZCB, and ZY (b) after thermal annealing.

plus. However, this difference in oxygen content is not reflected in the PL properties. Therefore, the present PLs β_H and β_Z are not due to oxygen vacancies. Impurities are certainly not responsible for the present PLs, since it is very unlikely that common impurities are present in all the samples studied. Therefore, PLs β_H and β_Z are truly intrinsic to hafnia and zirconia.

If we observe the PL spectra shown in Fig. 3(b) carefully, we notice the presence of a small hump around 4.2 eV on the PL spectrum of the sample ZCA. The presence of this hump is not limited to ZCA, and its height grows when the sample was thermally annealed. Figure 4 shows typical examples of this growth observed for the samples HCA and ZCA. Here, all the measurements were done in sequence using the samples mounted on a vertically movable nonrotating rod in the PL measurement chamber so that comparison of the PL intensities among different samples became possible.

In order to examine this new PL band more in detail, all the samples were annealed thermally at 900 °C in oxygen. Figure 5 shows the PL spectra observed in the thermally annealed samples, excited by SR photons at 6.0 eV for HCA, HCB, and HP or at 6.4 eV for ZCA, ZCB, and ZY. A similar

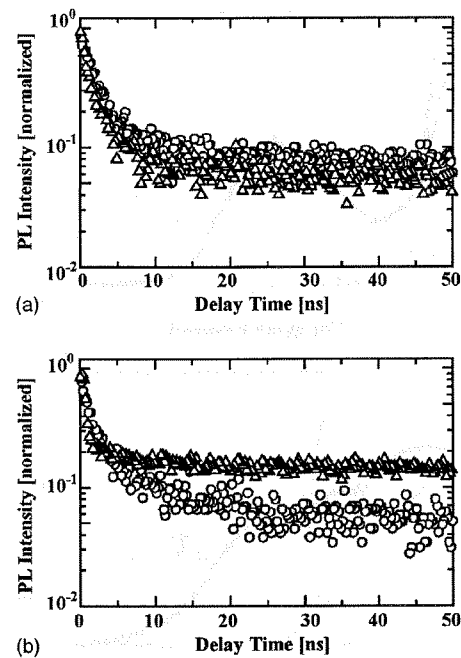


FIG. 6. Decay profiles of PL β_H observed in HCA (circles) and HP (triangles) (a) and those of PL β_Z observed in ZCA (circles) and ZY (triangles) (b).

PL peak is seen around 4.2 eV in the five kinds of samples, except for ZY. This PL is hereafter referred to as α_H or α_Z , depending on whether the sample is hafnia or zirconia. Note that the apparent peak around 2.1 eV is not a real PL peak but a stray or fake replica of the 4.2-eV peak. As in the case of PL β_H or β_Z , the peak energy and shape of PL α_H are independent of the source alkoxide, the deposition method, and the substrate material and are similar to those of PL α_Z . These results certainly give clues to a study on the PL mechanism. Note that similar results, such as the appearance of PL around 4.2 eV in hafnia by a heat treatment, were observed by cathodoluminescence.³⁷

The similarity in the PL characteristics is further investigated. Figure 6 shows the decay profiles of PLs β_H and β_Z observed in all the samples, except for HCB and ZCB. Note that HCB and ZCB were deposited using our old CVD apparatus that was replaced by our new one for HCA and ZCA before the measurements of the PL decay characteristics. The PL decay curve apparently consists of a fast component with a lifetime less than 2 ns and a slow one with a lifetime longer than 50 ns for all the samples. Here, the PL was excited repeatedly by the SR pulses once every 176 ns. Therefore, there is a possibility that the longer component does not represent the real decay profile due to the overlap of the preceding PLs. Although the ratio between the fast and slow components differs slightly among the samples, this small difference is considered to be negligible, since there could be many nonessential extraneous factors that affect the ratio. Thus, it is confirmed that all the four kinds of samples, HCA, HP, ZCA, and ZY, have essentially the identical PL decay profile. Figure 7 shows the decay profiles of α_H and α_Z observed for the heat-treated HCA, HP, and ZCA samples.

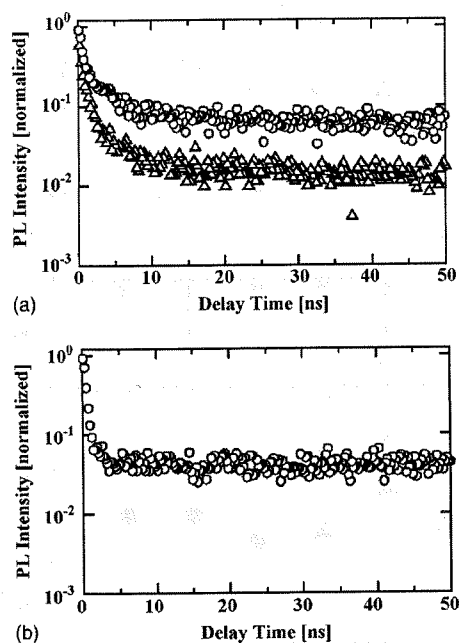


FIG. 7. Decay profiles of PL α_H observed in HCA (circles) and HP (triangles) (a) and that of PL α_Z in ZCA (b) after thermal annealing.

Similar to the case of PLs β_H and β_Z , the examined three kinds of samples show essentially the same PL decay profile. Namely, the decay profiles are independent of the kind of the sample or deposition method for both two PL peaks. This fact is also a strong indication that the presently observed PLs β_H , β_Z , α_H , and α_Z certainly reflect some intrinsic nature in common with hafnia and zirconia.

In order to further obtain information about the excitation of respective PLs, their PLE spectra were measured. Here, the samples used for PLs α_H and α_Z had been thermally treated. Figure 8(a) shows a typical PLE spectrum for PL β_H monitored at 2.8 eV and the one for PL α_H monitored at 4.4 eV observed in HCA. The PLE spectrum for PL β_H has two components; one showing the maximum around 5.1 eV and the other showing a steep rise around 5.7 eV. The location of the latter component is similar to the location of the onset of the PLE spectrum for PL α_H . This indicates that PL β_H has two PL origins; one is in common with PL α_H and the other is different. Similar PLE spectra were observed in the samples HCB and HP. Furthermore, the PLE spectra for PLs β_Z and α_Z observed in ZCA are shown in Fig. 8(b). Similar PLE spectra were obtained in ZCB. Note that PL α_Z does not appear in ZY even after the heat treatment.

The VUV absorption spectra were also measured. Here, Si substrates of the samples HCA, HCB, ZCA, and ZCB were replaced by CaF_2 substrates, since Si is opaque to VUV photons. As typical examples, the VUV absorption spectra obtained in HCA and ZCA are shown in Fig. 9. In common with the five samples other than ZY, the onset portion of the interband photon absorption between the valence band and the conduction band is not a steep curve. It spreads out over a wide energy range, which indicates that these five deposited film samples have much structural randomness. For ZY, only the initial portion of the absorption onset was measur-

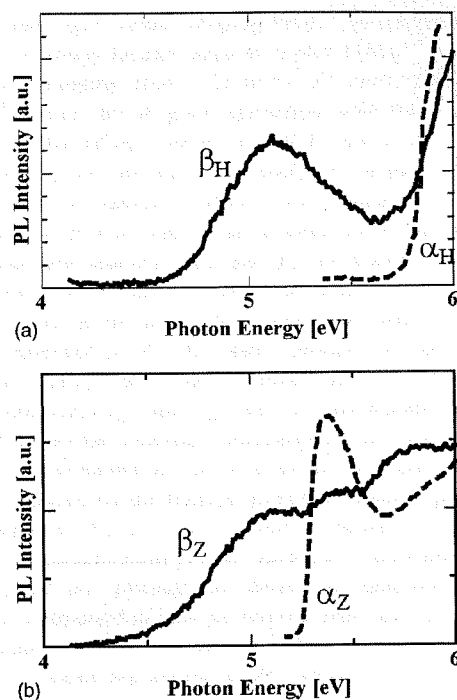


FIG. 8. PLE spectrum for PL β_H or α_H detected at 4.4 eV (broken curve) and that for PL β_Z or α_Z detected at 2.8 eV (solid curve), observed in HCA (a) and ZCA (b).

able due to its too thick thickness. However, the onset is located at an energy far lower than the band-gap energy of 4.9 eV.³⁶ This indicates that ZY has also a structural disorder. In such a material, the presence of two kinds of threshold energies is generally assumed. One is the band-gap energy due to interband photon absorption, which is hereafter referred to as E_{opt} . The other is due to photon absorption

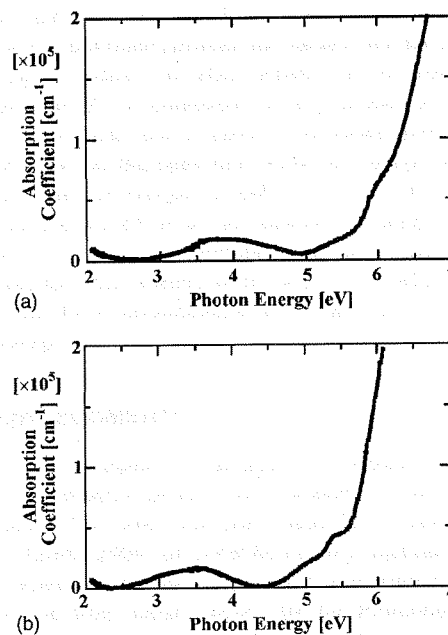


FIG. 9. VUV absorption spectra measured for HCA (a) and ZCA (b).

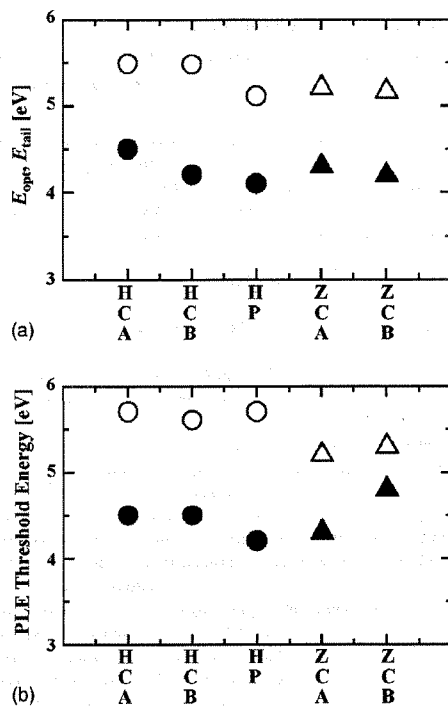


FIG. 10. (a) E_{opt} (open circles and triangles) and E_{tail} (solid circles and triangles). (b) PLE threshold energies E_{α} (open circles and triangles) and E_{β} (solid circles and triangles) of PL α_H , α_Z , β_H , or β_Z .

between tail states below the conduction band and those above the valence band, which is referred to as E_{tail} . For the five amorphous samples other than ZY, the photon absorption can be expressed by the following equation:³⁸

$$\alpha h\nu \propto (h\nu - E_g)^2, \quad (1)$$

where α , $h\nu$, and E_g are the absorption coefficient, photon energy, and band-gap energy, respectively. Assuming that both E_{opt} and E_{tail} can be estimated by Eq. (1) by substituting E_{opt} or E_{tail} for E_g , the two values are estimated, as shown in Fig. 10(a). Here, in replotting the absorption curves in accordance with Eq. (1), the initial onset portion and the next rising portion were used to estimate E_{tail} and E_{opt} , respectively. Furthermore, by assuming that a similar relationship holds between the threshold energy of PLE and the PLE spectrum, the threshold energies E_{α} for PLs α_H and α_Z and E_{β} for PLs β_H and β_Z are estimated, as shown in Fig. 10(b). In the PLE and VUV absorption measurements, the width of the monochromated SR photons would give influences to their onset energies. However, this width is as small as about 20 meV. Therefore, the estimated values of E_{opt} , E_{tail} , E_{α} , and E_{β} should be close to the real values.

Next, the E_{opt} value is compared with those reported in literature. Based on quantum chemical calculations, the band gap of zirconia was estimated to be 3.40–3.90 eV.³⁹ However, these values are too small as the authors themselves abandoned them to estimate the band offset.³⁹ Instead, they estimated the value by XPS to be 5.65 eV, which is slightly larger than the E_{opt} values of 5.21 eV for ZCA and 5.17 eV for ZCB.^{39,40} This difference between 5.17–5.21 and 5.65 eV should be regarded as small, since even crystal zirconia has

various band-gap values ranging from 5.83 to 7.09 eV, depending on many factors, such as crystal phase.⁴¹ For hafnia, the values ranging from 5.25 to 5.7 eV were estimated by XPS,^{42,43} which are in good agreement with the E_{opt} values of 5.49 eV for HCA, 5.48 eV for HCB, and 5.11 eV for HP.

From Fig. 10, the threshold energy E_{α} is quite similar to E_{opt} for all the samples, while E_{β} is similar to E_{tail} . This indicates that PLs α_H and α_Z are excited due to the interband absorption and that PLs β_H and β_Z are excited by photon absorption due to the excitation of electrons to localized states located at the tail of the conduction band. As for the PL β_Z observed in ZY, the same process can be assumed since the sample also has localized states, as mentioned above, although E_{tail} and E_{opt} were not measurable. Furthermore, the thermal treatment increases the intensities of PLs α_H and α_Z , as shown in Fig. 4. It seems that some structural change induced by the thermal treatment opens a path to the upper states of PLs α_H and α_Z . Another possibility is that the thermal treatment extinguishes localized states that quench PLs α_H and α_Z , although the details are unknown. Crystal zirconia is reported to have an indirect band gap according to a quantum chemical calculation.⁴⁴ This explains the reason that PL α_Z does not appear in ZY which is an only crystal among the samples tested.

IV. CONCLUSION

We investigated PL characteristics induced by ultraviolet photons for six hafnia and zirconia samples having a wide variation in many aspects, such as the synthesizing condition. A PL peak was observed around 2.8 eV in common with all the hafnia and zirconia samples. Moreover, the decay profile of this PL is also similar in all the samples. Namely, very similar phenomena are observed, irrespective of the difference in crystallinity and oxygen content of the sample, source alkoxide, deposition method, or the substrate material. This indicates that the PL is not due to impurities or defects at the interface between the sample and the substrate. The oxygen vacancy is also unlikely to be responsible. Therefore, this PL is considered to be intrinsic to hafnia or zirconia, most likely due to radiative recombination between localized states at the band tails. After the sample was thermally annealed in oxygen at 900 °C, a new PL peak appeared around 4.2 eV in all the amorphous samples. Its decay profile is also in common with these samples. By comparing the PLE spectra of the 4.2-eV PL with the VUV spectra, this PL is considered to be excited due to the interband absorption.

ACKNOWLEDGMENTS

We want to thank S. Yamazaki of National Institute of Advanced Industrial Science and Technology for providing HP samples. This work was partly done in the Joint Studies Program (2000–2004) of UVSOR Facility, Institute for Molecular Science, Okazaki, Japan and was supported by a Grant-in-Aid from Japan Society for the Promotion of Science for Scientific Research (B) Grant No. 16360160. A grant from Mizuho Foundation for the Promotion of Sci-

ences and a High-Tech Research Grant from the Ministry of Education, Culture, Sports, Science and Technology of Japan are also appreciated.

- ¹International Technology Roadmap for Semiconductors, International Sematech <http://public.itrs.net/> (2002).
- ²D. A. Muller, T. Sorsch, S. Morrio, F. H. Baunann, K. E. Lutterodt, and G. Timp, *Nature (London)* **399**, 758 (1999).
- ³J. H. Stathis and D. J. DiMaria, *Tech. Dig. - Int. Electron Devices Meet.* **1998**, 167.
- ⁴B. Brar, G. D. Wilk, and A. C. Seabaugh, *Appl. Phys. Lett.* **69**, 2728 (1996).
- ⁵G. D. Wilk, R. M. Wallace, and J. M. Anthony, *J. Appl. Phys.* **89**, 5243 (2001).
- ⁶G. D. Wilk and R. M. Wallace, *Appl. Phys. Lett.* **76**, 112 (2000).
- ⁷B. H. Lee, L. Kang, R. Nieh, W. J. Qi, and J. C. Lee, *Appl. Phys. Lett.* **76**, 1926 (2000).
- ⁸W. J. Qi *et al.*, *Tech. Dig. - Int. Electron Devices Meet.* **1999**, 145.
- ⁹Y. H. Wu, M. Y. Yang, A. Chin, W. J. Chen, and C. M. Kwei, *IEEE Electron Device Lett.* **21**, 341 (2000).
- ¹⁰H. H. Tseng *et al.*, *Tech. Dig. - Int. Electron Devices Meet.* **2003**, 83.
- ¹¹D. A. Neumayer and E. Cartier, *J. Appl. Phys.* **90**, 1801 (2001).
- ¹²W. J. Zhu, T. P. Ma, T. Tamagawa, J. Kim, and Y. Di, *IEEE Electron Device Lett.* **23**, 97 (2002).
- ¹³J. P. Chang and Y. S. Lin, *J. Appl. Phys.* **90**, 2964 (2001).
- ¹⁴M. Matsuoka, S. Isotani, J. F. D. Chubaci, S. Miyake, Y. Setsuhara, K. Ogata, and N. Kuratani, *J. Appl. Phys.* **88**, 3773 (2000).
- ¹⁵S. Miyazaki, *Appl. Surf. Sci.* **190**, 66 (2002).
- ¹⁶D. Park, Y. C. King, Q. Lu, T. J. King, C. Hu, A. Kalnitsky, S. P. Tay, and C. C. Cheng, *IEEE Electron Device Lett.* **19**, 441 (1998).
- ¹⁷S. Miyazaki, *J. Vac. Sci. Technol. B* **19**, 2212 (2001).
- ¹⁸Y. I. Ogita, S. Iehara, and T. Tomita, *Thin Solid Films* **430**, 161 (2003).
- ¹⁹H. Kato, T. Nango, T. Miyagawa, T. Katagiri, K. S. Seol, and Y. Ohki, *J. Appl. Phys.* **92**, 1106 (2002).
- ²⁰G. D. Wilk, R. M. Wallace, and J. M. Anthony, *J. Appl. Phys.* **87**, 484 (2000).
- ²¹N. Ikarashi and K. Manabe, *J. Appl. Phys.* **94**, 480 (2003).
- ²²J. Morais, E. B. O. da Rosa, L. Miotti, R. P. Pezzi, I. J. R. Baumvol, A. L. P. Rotondaro, M. J. Bevan, and L. Colombo, *Appl. Phys. Lett.* **78**, 2446 (2001).
- ²³M. Koike *et al.*, *Tech. Dig. - Int. Electron Devices Meet.* **2003**, 107.
- ²⁴H. Y. Yu *et al.*, *Appl. Phys. Lett.* **81**, 376 (2002).
- ²⁵R. S. Johnson, J. G. Hong, C. Hinkle, and G. Lucovsky, *J. Vac. Sci. Technol. B* **20**, 1126 (2002).
- ²⁶W. J. Zhu, T. P. Ma, S. Zafar, and T. Tamagawa, *IEEE Electron Device Lett.* **23**, 597 (2002).
- ²⁷J. F. Conley, Y. Ono, R. Solanki, G. Stecker, and W. Zhuang, *Appl. Phys. Lett.* **82**, 3508 (2003).
- ²⁸A. Y. Kang, P. M. Lenahan, and J. F. Conley, *Appl. Phys. Lett.* **83**, 3407 (2003).
- ²⁹H. Nishikawa, T. Shiroyama, R. Nakamura, and Y. Ohki, *Phys. Rev. B* **45**, 586 (1992).
- ³⁰K. S. Seol, T. Watanabe, M. Fujimaki, H. Kato, Y. Ohki, and M. Takiyama, *Phys. Rev. B* **62**, 1532 (2000).
- ³¹H. Kato, N. Kashio, Y. Ohki, K. S. Seol, and T. Noma, *J. Appl. Phys.* **93**, 239 (2003).
- ³²T. Noma, K. S. Seol, H. Kato, M. Fujimaki, and Y. Ohki, *Appl. Phys. Lett.* **79**, 1995 (2001).
- ³³M. Kunz, H. Kretschmann, W. Assmus, and C. Klingshirn, *J. Lumin.* **37**, 123 (1987).
- ³⁴P. Camagni, P. Galinetto, and G. Samoggia, *Solid State Commun.* **83**, 943 (1992).
- ³⁵S. E. Paje and J. Llopis, *Appl. Phys. A: Solids Surf.* **57**, 225 (1993).
- ³⁶H. Nakajima, T. Mori, S. Itoh, and M. Watanabe, *Solid State Commun.* **129**, 421 (2004).
- ³⁷S. Yamasaki, N. Mizuochi, T. Yasuda, J. Isoya, S. Sakai, M. Kadoshima, and T. Nabatame, *Extended Abstracts of the 49th Spring Meeting 2002 of the Japan Society of Applied Physics and Related Societies* (Japan Society of Applied Physics, Tokyo, 2002), Vol. 2, p. 821.
- ³⁸N. F. Mott and E. A. Davis, in *Electronic Processes in Non-Crystalline Materials*, 2nd ed. (Clarendon, Oxford, 1979), p. 289.
- ³⁹R. Puthenkovilakam, E. A. Carter, and J. P. Chang, *Phys. Rev. B* **69**, 155329 (2004).
- ⁴⁰R. Puthenkovilakam and J. P. Chang, *Appl. Phys. Lett.* **84**, 1353 (2004).
- ⁴¹R. H. French, S. J. Glass, F. S. Ohuchi, Y. N. Xu, and W. Y. Ching, *Phys. Rev. B* **49**, 5133 (1994).
- ⁴²R. Puthenkovilakam and J. P. Chang, *J. Appl. Phys.* **96**, 2701 (2004).
- ⁴³R. G. Vitchev, J. J. Pireaux, T. Conard, H. Bender, J. Wolstenholme, and C. Defranoux, *Appl. Surf. Sci.* **235**, 21 (2004).
- ⁴⁴B. Kralik, E. K. Chang, and S. G. Louie, *Phys. Rev. B* **57**, 7027 (1998).

Mechanisms of several photoluminescence bands in hafnium and zirconium silicates induced by ultraviolet photons

Toshihide Ito^{a)}

Department of Electrical Engineering and Bioscience, Waseda University, Shinjuku-ku, Tokyo 169-8555, Japan

Hirimitsu Kato

Diamond Research Center, National Institute of Advanced Industrial Science and Technology, Umezono, Tsukuba-shi, Ibaraki 305-8565, Japan

Yoshimichi Ohki

Department of Electrical Engineering and Bioscience, Waseda University, Shinjuku-ku, Tokyo 169-8555, Japan

(Received 19 August 2005; accepted 31 March 2006; published online 15 May 2006)

Two photoluminescence (PL) components with peaks around 2.8–3.0 and 3.8 eV were induced in hafnium silicates by the irradiation of synchrotron radiation photons at 8.0 eV, while two similar ones were induced in zirconium silicates around 2.7–3.0 and 3.8 eV. By examining PL excitation spectra, PL decay characteristics, and vacuum-ultraviolet absorption spectra, it is assumed that the origin of the PL component around 2.7(2.8)–3.0 eV is the same as that of the PL component around 2.7–2.9 eV observed in hafnia and zirconia. In the band gaps of hafnium silicates, zirconium silicates, hafnia, and zirconia, luminescent centers responsible for the PL components around 2.7(2.8)–2.9(3.0) eV have their respective upper and lower states with a certain constant energy difference that does not change by the hafnium or zirconium content. Electrons (or holes) excited by ultraviolet photons to tail states at the band edges first relax to the upper state of the luminescent centers, and then they are deexcited to the lower state, which induces the PL components. © 2006 American Institute of Physics. [DOI: 10.1063/1.2199977]

I. INTRODUCTION

With the miniaturization of silicon-based electronic devices, the thickness of silicon dioxide as a gate dielectric for complementary metal oxide semiconductor devices is about to reach a value below its thinnest limit in near future.¹ In this region, direct tunneling dominates the leakage current and silicon dioxide would not maintain its insulating property.^{2–4} In order to solve this problem and to maintain a proper thickness of the gate dielectric, materials with higher permittivities are being considered as replacements.^{5–9} Numerous materials such as hafnia,^{10–12} zirconia,^{11,13,14} hafnium silicate,^{15–17} zirconium silicate,^{15–18} hafnium silicon oxynitride,¹⁹ and hafnium aluminate^{20,21} are examined as a candidate. However, there is a high possibility that a lot of localized states due to defects are present in the band gap of these materials.^{22,23} These localized states are assumed to cause leakage current.²⁴ From this viewpoint, detailed and systematic studies on the localized states are indispensable to understand the effects of the defects on electrical properties and to suppress the leakage current.

In our previous paper,²⁵ we reported photoluminescence (PL) characteristics in hafnia and zirconia. In the present research, we apply the PL method to a series of hafnium silicate samples with different hafnium contents synthesized with plasma-enhanced chemical-vapor deposition (PECVD), and to a similar series of zirconium silicate samples.

II. EXPERIMENTAL PROCEDURES

The samples examined are hafnium silicate (HSA12-HSA81 and HSB12-HSB81) and zirconium silicate (ZSA06-ZSA78) as listed in Table I. The samples HSA12-HSA81 were deposited by PECVD using tetraethoxysilane [TEOS:Si(OC₂H₅)₄] and a hafnium alkoxide [Hf(O-*t*-C₄H₉)₄] as source alkoxides, while HSB12-HSB81 were deposited using TEOS and another hafnium alkoxide [Hf(O-*i*-C₃H₇)₄]. The samples ZSA06-ZSA78 were deposited similarly by PECVD using TEOS and a zirconium alkoxide [Zr(O-*t*-C₄H₉)₄]. Oxygen, used as an oxidation gas, was excited with a rf power of 13.56 MHz through capacitive coupling.

For HSA12-HSA81 or ZSA06-ZSA78, the hafnium or zirconium alkoxide was vaporized and transported at 150 °C into the oxygen plasma by controlling its flow rate with a mass-flow controller. A TEOS gas vaporized at 70 °C was also transported into the oxygen plasma. In about 20 min, a film about 100 nm thick was deposited on a substrate when the substrate temperature was kept constant at 500 °C. A CaF₂ crystal transparent to 9.9 eV (125 nm) was used as a substrate for vacuum-ultraviolet (VUV) absorption measurements, while a *p*-type silicon monocrystal wafer (100) was used for other measurements. For HSB12-HSB81, the hafnium alkoxide was vaporized and transported at 220 °C into the oxygen plasma using argon as a carrier and diluent gas, while TEOS was vaporized and transported at 70 °C. In about 40 min, a 100 nm thick film was deposited on the substrate at 400 °C. Two kinds of hafnia films (HA and HB) and

^{a)}Electronic mail: prince@suou.waseda.jp

TABLE I. Samples examined with their elemental compositions and thicknesses.

Sample	Elemental ratio (at. %)			$\text{Hf}_x\text{Si}_{(1-x)}\text{O}_y$		Thickness (nm)
	Hf	Si	O	x	y	
HSA12	3.6	27	69	0.12	2.3	72
HSA37	12	21	67	0.37	2.0	96
HSA55	20	16	64	0.55	1.8	115
HSA81	31	7.2	62	0.81	1.6	123
HA	40	0	60	1.0	1.5	103
HSB12	3.7	28	69	0.12	2.2	192
HSB42	15	21	64	0.42	1.8	185
HSB69	25	12	63	0.69	1.7	169
HSB81	30	7.2	63	0.81	1.7	137
HB	41	0	59	1.0	1.4	130

Sample	Elemental ratio (at. %)			$\text{Zr}_x\text{Si}_{(1-x)}\text{O}_y$		Thickness (nm)
	Zr	Si	O	x	y	
ZSA06	1.9	29	69	0.06	2.2	144
ZSA15	4.7	27	69	0.15	2.2	210
ZSA31	9.9	22	68	0.31	2.1	105
ZSA51	17	16	67	0.51	2.0	106
ZSA64	22	12	66	0.64	1.9	104
ZSA78	27	7.6	65	0.78	1.9	38
ZA	35	0	65	1.0	1.8	130

one kind of zirconia film (ZA) deposited without using TEOS were also prepared as references. All the samples were postannealed at 500 °C for 10–20 min in a rapid thermal annealing apparatus filled with oxygen gas at a pressure of $\sim 1.0 \times 10^5$ Pa. In addition, some samples were postannealed again at 900 °C for 20 min in a similar oxygen atmosphere.

Using synchrotron radiation (SR) under multibunch operation at the BL1B line of UVSOR Facility (Institute for Molecular Science, Okazaki, Japan, beam energy: 750 MeV) as a photon source, PL, PL excitation (PLE), and VUV absorption spectra were measured. The PL decay characteristics were examined by a single-photon counting method using SR under single-bunch operation (SR duration of ~ 400 ps and interval of 176 ns). We also measured time-resolved PL using an ArF excimer laser (photon energy of 6.4 eV, pulse width of ca. 25 ns, power of ca. 150 mJ/pulse, and pulse repetition frequency of 1 Hz, Lambda Physik Compex 205) and a monochromator equipped with an intensified charge-coupled device (ICCD) array. The ICCD array was gated by a pulse generator connected to a delay circuit, and the delay time between the laser pulse and the gate-on pulse was monitored with an oscilloscope. The gate-on period or the PL observation period was adjusted to 40 ns. The PL, PLE, and PL decay were measured at the liquid-helium temperature, while VUV absorption and time-resolved PL were measured at room temperature.

In order to study the elemental composition, the samples were examined by x-ray photoelectron spectroscopy (XPS) (JEOL JPS-9010TR or JEOL JPS-90MX) using Mg $K\alpha$ ($h\nu = 1253.6$ eV) x rays. The thickness was measured by ellipsometry (Ulvac ESM-1) at a wavelength of 632.8 nm.

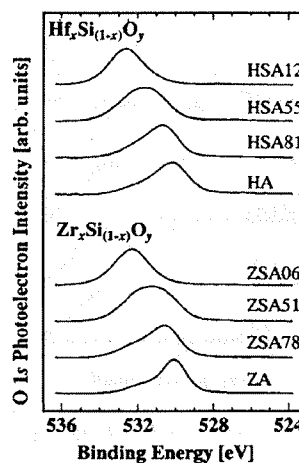


FIG. 1. O 1s photoelectron spectra obtained for the samples.

III. RESULTS AND DISCUSSION

Four kinds of hafnium silicates and six kinds of zirconium silicates with various compositions were successfully deposited for each source alkoxide. Hereafter, the samples are named after their hafnium or zirconium contents. Namely, sample HSA12 means that it is hafnium silicate with the formula $\text{Hf}_{0.12}\text{Si}_{0.88}\text{O}_{2.3}$. Figures 1, 2, 3(a), and 3(b) show XPS O 1s, Si 2p, Hf 4f, and Zr 3d photoelectron spectra, respectively. By integrating these spectral areas, the elemental compositions were calculated as shown in Table I. When the elemental composition is expressed by $\text{Hf}_x\text{Si}_{(1-x)}\text{O}_y$ for hafnium silicates or $\text{Zr}_x\text{Si}_{(1-x)}\text{O}_y$ for zirconium silicates, the samples are stoichiometric if y is equal to 2. According to Table I, y decreases with an increase in x , which means that the sample becomes oxygen deficient from oxygen surplus.

Figure 4(a) shows PL spectra induced in the samples HSA12-HSA81 and HA by the irradiation of SR photons at 8.0 eV, while Fig. 4(b) shows those similarly induced in the samples HSB12-HSB81 and HB. The measured intensity of a PL peak generally depends on various hardly controllable factors, such as a subtle difference in the mutual angles among the photon source, the sample, and the detector. This

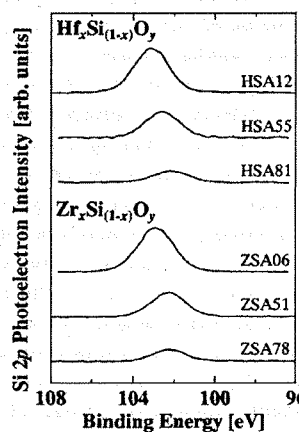


FIG. 2. Si 2p photoelectron spectra obtained for the samples.

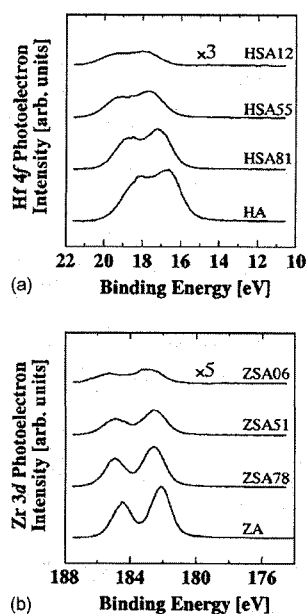


FIG. 3. Hf 4f photoelectron spectra obtained for hafnium silicates (a) and Zr 3d photoelectron spectra obtained for zirconium silicates (b).

sometimes makes it difficult to compare the PL intensities among different samples. Therefore, in all the figures, except for Figs. 8 and 14, the PL intensity is shown after being normalized by the highest peak height. In Fig. 4(a), all the

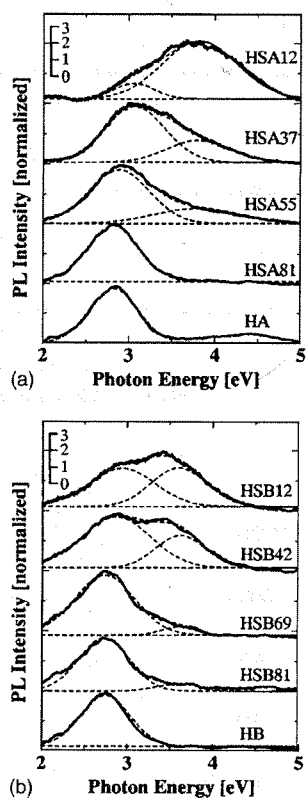


FIG. 4. PL spectra induced by 8.0 eV photons from SR in hafnium silicates deposited using $\text{Hf}(\text{O}-i-\text{C}_4\text{H}_9)_4$ (a) and $\text{Hf}(\text{O}-i-\text{C}_3\text{H}_7)_4$ (b) as a hafnium alkoxide.

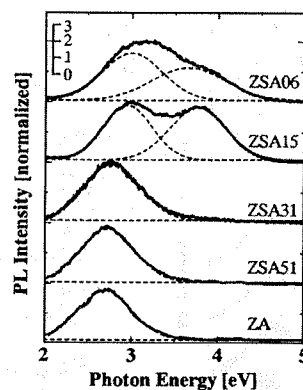


FIG. 5. PL spectra induced by 8.0 eV photons from SR in zirconium silicates.

hafnium silicate samples have a broad PL band around 2.0–5.0 eV. Each PL spectrum is Gaussian-fitted with two components around 2.8–3.0 and 3.8 eV as shown with broken curves. Similar PL spectra were observed regardless of the difference in source alkoxide as shown in Fig. 4(b). As clearly shown in our previous paper,²⁵ PLs observed in hafnia and zirconia are independent of the difference in crystallinity or oxygen content of the sample, source alkoxide, deposition method, or the substrate material. Therefore, we have concluded that the PLs in hafnia and zirconia are attributable to their intrinsic nature. In the same context, the present result strongly indicates that the two PL components at 2.8–3.0 and 3.8 eV are not due to impurities but intrinsic to hafnium silicates.

Figure 5 shows PL spectra excited by 8.0 eV photons in all the zirconium silicate and zirconia samples, except for ZSA64 and ZSA78. A broad PL spectrum, which looks similar to the one induced in hafnium silicates, is seen in all the samples. These PL spectra are Gaussian-fitted with two components around 2.7–3.0 and 3.8 eV similarly as in the case of hafnium silicates. Note that the 3.8 eV component was not observed when x is not less than 0.31. For all the hafnium and zirconium silicate samples, the peak energy of the lower-energy PL component at 2.7(2.8)–3.0 eV slightly shifts toward a lower energy with an increase in x .

Figure 6 shows PL spectra induced in all the hafnia and hafnium silicate samples by the irradiation of 6.4 eV SR photons, while Fig. 7 shows similar spectra induced by 6.4 eV photons in all the zirconia and zirconium silicate samples, except for ZSA64 and ZSA78. All the PL spectra have a PL component around 2.8–2.9 eV. This PL component is similar to the one around 2.7(2.8)–3.0 eV observed in the case of the excitation by 8.0 eV photons. However, the peak energy shift as a function of x observed in Figs. 4 and 5 seems to disappear in the case of 6.4 eV excitation. Moreover, the intensity of the 3.8 eV component excited by 6.4 eV photons is far smaller than that excited by 8.0 eV photons in both the hafnium and zirconium silicates.

As reported in our previous paper,²⁵ hafnia and zirconia exhibit similar PL spectra with similar characteristics around 2.7–2.9 eV. Judging from their behavior, it is highly probable that the PLs in hafnia and zirconia are not due to impu-

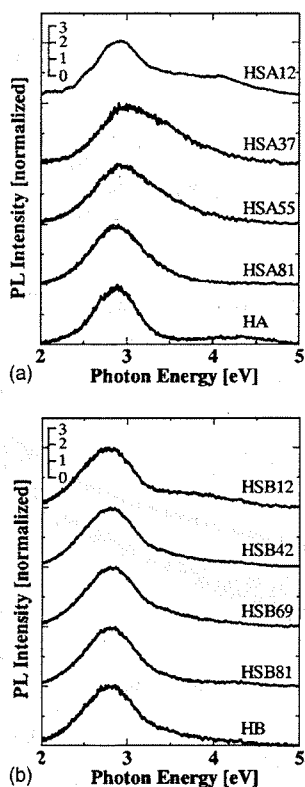


FIG. 6. PL spectra induced by 6.4 eV photons from SR in hafnium silicates deposited using $\text{Hf}(\text{O}-t\text{-C}_3\text{H}_7)_4$ (a) and $\text{Hf}(\text{O}-i\text{-C}_3\text{H}_7)_4$ (b) as a hafnium alkoxide.

rities or defects at the interface between the sample and the substrate. They are thus considered to be intrinsic in common with hafnia and zirconia. We referred to these PLs as β_H or β_Z depending on whether the sample is hafnia or zirconia. We also reported that a new PL peak appeared around 4.2 eV in hafnia and zirconia after the samples had been thermally annealed in oxygen at 900 °C.²⁵ This new PL was referred to as α_H or α_Z , similarly depending on whether the material was hafnia or zirconia. Although the postannealing was done at 500 °C in the present research, a slight PL α_H peak is observable in the HA spectrum shown in Fig. 4(a).

The PL component around 2.8–3.0 eV induced in

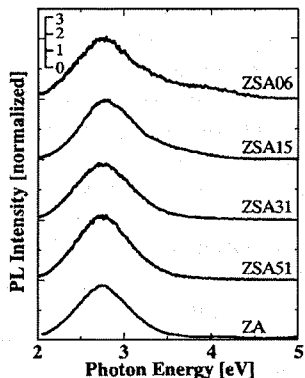


FIG. 7. PL spectra induced by 6.4 eV photons from SR in zirconium silicates.

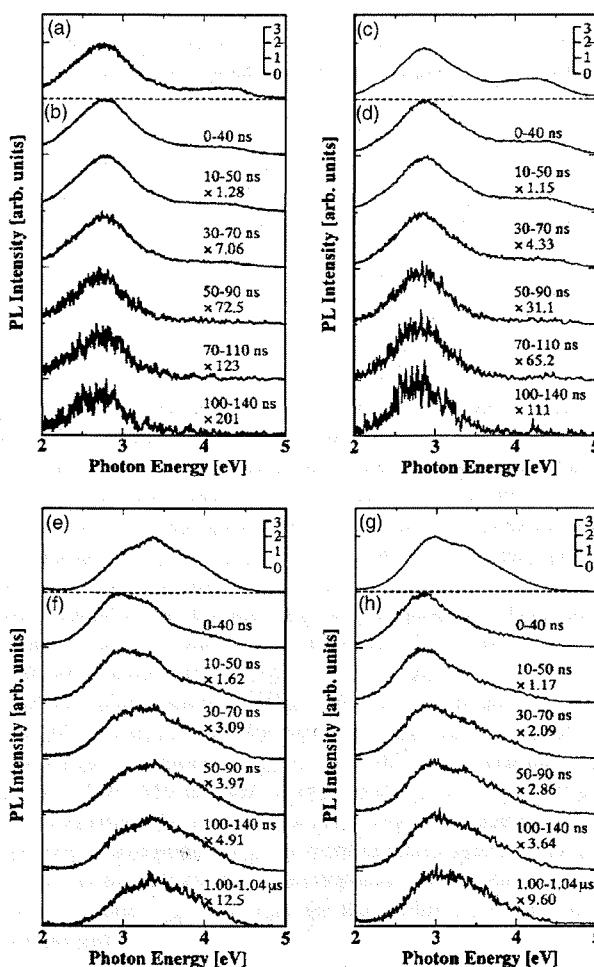


FIG. 8. PL spectrum and its time-resolved spectra observed during given observation periods for HA [(a) and (b)], ZA [(c) and (d)], HSA12 [(e) and (f)], and ZSA06 [(g) and (h)]. All the spectra were excited by 6.4 eV photons from the ArF excimer laser.

hafnium silicate shown in Figs. 4 and 6 is very similar to PL β_H . Moreover, the 2.7–3.0 eV component induced in zirconium silicate shown in Figs. 5 and 7 is also similar to PL β_Z . Therefore, these PL components are hereafter referred to as PL β_{HS} or β_{ZS} , depending on whether the sample is hafnium or zirconium silicate. On the other hand, the PL around 3.8 eV is hereafter referred to as PL γ_{HS} or γ_{ZS} .

In order to examine the similarity between PLs β_H and β_{HS} or that between PLs β_Z and β_{ZS} time-resolved PL spectra were examined. Figure 8(a) shows the whole spectrum of PL β_H induced in HA by the irradiation of 6.4 eV photons from the ArF excimer laser, while Fig. 8(b) shows its time-resolved spectra, measured during given periods right after the PL intensity had shown its maximum intensity. The PL α_H , which is slightly seen in Fig. 8(a), will not be discussed here. As shown in Fig. 8(b), the intensity of PL β_H decreases as the delay time becomes longer, while its wave form and its peak energy do not change.

A similar whole spectrum and its time-resolved spectra are shown in Figs. 8(c) and 8(d) for ZA, in Figs. 8(e) and 8(f) for HSA12, and in Figs. 8(g) and 8(h) for ZSA06. As shown

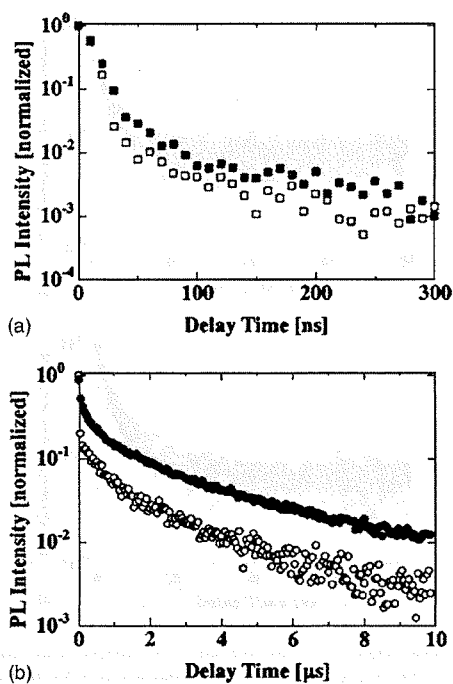


FIG. 9. (a) Decay profiles of PL β_H observed in HA (open squares) and PL β_Z observed in ZA (solid squares). (b) Those of PL β_{HS} observed in HSA12 (open circles) and PL β_{ZS} observed in ZSA06 (solid circles).

in Fig. 8(d), the intensity of PL β_Z in ZA also decreases with an increase in the delay time. Furthermore, the intensities of PLs β_{HS} and β_{ZS} in both silicates also decrease with an increase in the delay time. As shown in Figs. 6 and 7, PLs γ_{HS} and γ_{ZS} are scarcely induced by the irradiation of SR photons at 6.4 eV. Nevertheless, they are clearly observable in Figs. 8(e) and 8(g) with their wave shapes very similar to those induced by the 8.0 eV photons from SR shown in Figs. 4 and 5. It is probable that PLs γ_{HS} and γ_{ZS} in Figs. 8(e) and 8(g) were excited by two-photon absorption since the power of the excimer laser is as high as ~ 150 mJ/pulse.

As mentioned above, the intensity of PL β_{HS} in Fig. 8(f) decreases with an increase in the delay time. Moreover, its peak energy slightly shifts toward a higher energy with an increase in the delay time. Namely, the peak is at 2.9 eV for the delay time of 0–40 ns, while it is at 3.2 eV for the delay time of 50 ns–1.04 μ s. The peak energy did not change after the delay time of 1.04 μ s, although the spectra are not shown here. Therefore, PL β_{HS} is considered to have two subcomponents: one peak around 2.9 eV and the other located at a slightly higher energy. Quite similar behavior is seen in Fig. 8(h) for the intensity and peak energy of PL β_{ZS} observed in ZSA06.

Figure 9(a) shows the decay profiles of PLs β_H and β_Z obtained by replotting their intensities shown in Figs. 8(b) and 8(d), while Fig. 9(b) shows those of PLs β_{HS} and β_{ZS} similarly obtained from Figs. 8(f) and 8(h). It can be seen that PLs β_H and β_Z have very similar decay profiles that consist of a fast component $\tau_{\beta 1}$ and a slow component $\tau_{\beta 2}$.

Assuming that a PL has several components and that each component shows an exponential decay, the measured

PL intensity I is expressed by the following equation when the finite laser pulse width and exposure period to ICCD are taken into consideration:

$$\begin{aligned}
 I(t_d) &= \int_{t_d}^{t_e} \int_0^{t_p} \sum_i I_{0i} \exp\left(-\frac{T-u}{\tau_i}\right) dudT \\
 &= \sum_i I_{0i} \tau_i^2 \left\{ \exp\left(-\frac{t_e}{\tau_i}\right) + \exp\left(-\frac{t_d-t_p}{\tau_i}\right) - \exp\left(-\frac{t_d}{\tau_i}\right) \right. \\
 &\quad \left. - \exp\left(-\frac{t_e-t_p}{\tau_i}\right) \right\}. \quad (1)
 \end{aligned}$$

Here, I_{0i} is the PL intensity of the i th PL right after its excitation by the laser for $u < t < u + du$, and τ_i is its lifetime. We assumed that the laser pulse had a rectangular shape, beginning at $t=0$ and ending at $t=t_p$, and that the ICCD gate opened at $t=t_d$ and closed at $t=t_e$. Under the experimental conditions of $t_p=25$ ns and $t_e-t_d=40$ ns, the data points shown in Fig. 9(a) were fitted to Eq. (1). Both PLs β_H and β_Z were found to be divided into two components. Their lifetimes $\tau_{\beta 1}$ and $\tau_{\beta 2}$ were found to be the same in the two PLs, and were estimated as $\tau_{\beta 1} < \sim 10$ ns and $\tau_{\beta 2} \sim 100$ ns. The data points shown in Fig. 9(b) can be similarly divided into three components for both PLs β_{HS} and β_{ZS} with a fast decay component $\tau_{\beta S1} \sim 15$ –40 ns, a medium one $\tau_{\beta S2} \sim 500$ –550 ns, and a slow one $\tau_{\beta S3} \sim 3.0$ –3.5 μ s. By comparing the spectra shown in Figs. 8(f) and 8(h), the fast decay component $\tau_{\beta S1}$ in both silicates seems to be ascribed to the 2.9 eV PL subcomponent, while the medium and slow ones $\tau_{\beta S2}$ and $\tau_{\beta S3}$ are due to the 3.2 eV PL subcomponent.

There is a possibility that the fast decay components $\tau_{\beta 1}$ and $\tau_{\beta S1}$ could not be estimated correctly, since they are shorter than the laser width or the gate-on period of the ICCD array. Therefore, the decay profiles were measured using a single-photon counting method. The results are shown in Fig. 10. All the PLs β_H , β_Z , β_{HS} , and β_{ZS} have almost the same decay profile consisting of a fast and a slow decay component. From this, $\tau_{\beta 1}$ and $\tau_{\beta S1}$ have the same value of almost 3 ns. In the single-photon counting method, the PL was excited repeatedly by the SR pulses once every 176 ns. Since the observation period was as long as several minutes, a very slow PL component should have been accumulated so many times. Therefore, the slow decay component shown in Figs. 10(a) and 10(b) is assumed to be affected by such accumulation of slow components such as $\tau_{\beta S2}$ and $\tau_{\beta S3}$ observed in the time-resolved measurements using the gate array. From these results, it can be assumed that PLs β_{HS} and β_{ZS} have the same fast decay component as PLs β_H and β_Z do. It is true that the slow decay components of the former two PLs are different from those of the latter two PLs. However, the decay speed of a relatively slower component of a PL is generally easily changeable as will be discussed later. Therefore, it is reasonable to assume that the origins of PLs β_{HS} and β_{ZS} are very similar to those of PLs β_H and β_Z .

It is known that silica has a well-defined PL around 2.7 eV.²⁶ This PL has a very long lifetime of ~ 10 ms and two clear PLE peaks around 5.0 and 7.6 eV. It is clear that

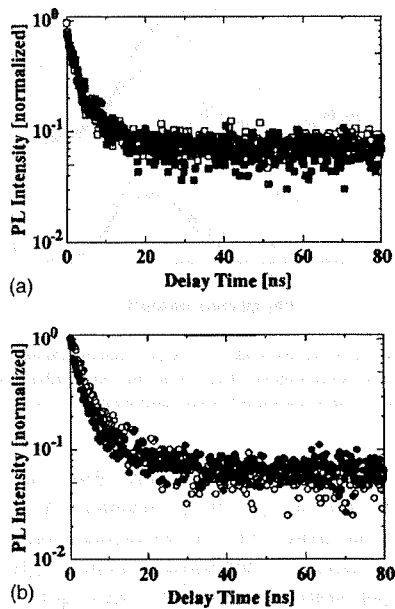


FIG. 10. (a) Decay profiles of PL β_H observed in HA (open squares) and PL β_Z observed in ZA (solid squares). (b) Those of PL β_{HS} observed in HSA12 (open circles) and PL β_{ZS} observed in ZSA06 (solid circles).

the present PLs β_{HS} and β_{ZS} do not have such a slow decay component. Furthermore, their PLE spectra are completely different from those of silica as shown later. Therefore, PLs β_{HS} and β_{ZS} are not due to silica, but due to a structure related to hafnium or zirconium such as their oxides or silicates.

The decay profiles of PLs γ_{HS} and γ_{ZS} are replotted in Fig. 11 from Figs. 8(f) and 8(h), similarly to those of PLs β_H , β_Z , β_{HS} , and β_{ZS} . They are very similar to those of PLs β_{HS} and β_{ZS} . Therefore, the medium and slow decay components of PL β_{HS} are almost the same as those of PL γ_{HS} , and those of PL β_{ZS} are also the same as those of PL γ_{ZS} . In order to confirm more the similarity between the decay profiles of PLs β_{HS} and β_{ZS} and that between the profiles of PLs γ_{HS} and γ_{ZS} , we tried to estimate the fast decay components of PLs γ_{HS} and γ_{ZS} using the single-photon counting method. Figure 12 shows the obtained decay profiles. As mentioned above, the slow decay components overlap the fast ones. Therefore, the fast decay components of PLs γ_{HS} and γ_{ZS} could not be compared with those of PLs β_{HS} and β_{ZS} . Nev-

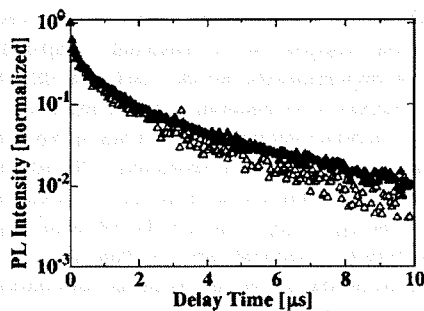


FIG. 11. Decay profiles of PL γ_{HS} observed in HSA12 (open triangles) and PL γ_{ZS} observed in ZSA06 (solid triangles).

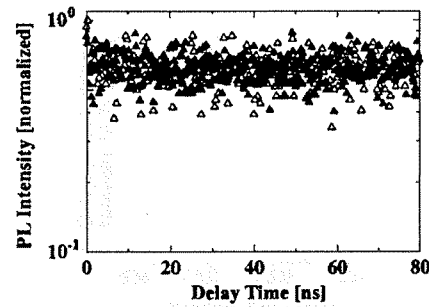


FIG. 12. Decay profiles of PL γ_{HS} observed in HSA12 (open triangles) and that of PL γ_{ZS} observed in ZSA06 (solid triangles).

ertheless, this does not imply that the similarity of the decay profiles is denied. The following discussion will be continued on the assumption that the overall similarity between the decay profiles has been confirmed. Namely, the decay profiles are similar between PLs γ_{HS} and β_{HS} and between PLs γ_{ZS} and β_{ZS} , although their peak energies are different. This can be explained as follows. After being excited to the upper state by photons, part of electrons relaxes to a middle state, which is the upper state of the luminescent centers responsible for PL β_{HS} or β_{ZS} . Another part of the excited electrons relax to another middle state, which is the upper state of the luminescence centers responsible for PL γ_{HS} or γ_{ZS} . During this relaxation, there could be nonluminescent medium and slow transition processes, which reflects the decay profiles.

Figure 13(a) shows changes in peak energies of PLs β_{HS} , β_{ZS} , γ_{HS} , and γ_{ZS} as a function of hafnium or zirconium content x . The peak energy shifts lower by about 0.2 eV for PLs β_{HS} and β_{ZS} . As shown in Fig. 8, for both β_{HS} and β_{ZS} , the PL is composed of two subcomponents around 2.9 and 3.2 eV. Therefore, it is natural to assume that the peak energy shift was induced by the change in ratio of the two

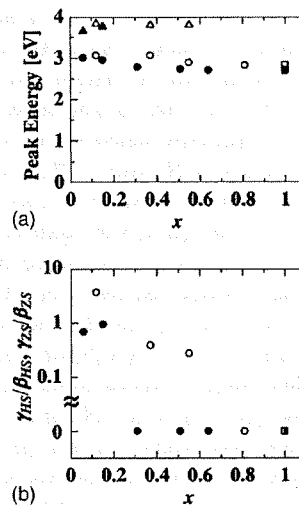


FIG. 13. (a) Changes in peak energy for PLs β_{HS} (open circles), γ_{HS} (open triangles), β_H (open square), β_{ZS} (solid circles), γ_{ZS} (solid triangles), and β_Z (solid square), as a function of hafnium or zirconium content x . (b) Those in PL intensity ratio for (γ_{HS}/β_{HS}) (open circles), (γ_{HS}/β_H) (open square), (γ_{ZS}/β_{ZS}) (solid circles), and (γ_{ZS}/β_Z) (solid square). For $x=1$, β_H and β_Z were used instead of β_{HS} and β_{ZS} .

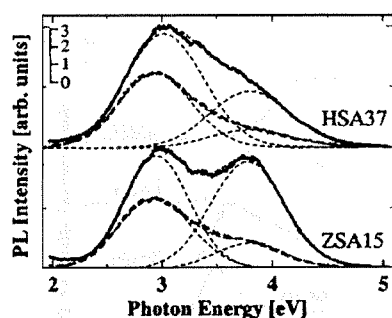


FIG. 14. PL spectra induced by 8.0 eV photons from SR in HSA37 and ZSA15 before (solid lines) and after (bold dashed lines) the thermal treatment at 900 °C. Fine dashed lines show Gaussian-fitted components.

subcomponents with an increase in x . Next, the ratio ($\gamma_{\text{HS}}/\beta_{\text{HS}}$) of the intensity of PL γ_{HS} to that of PL β_{HS} in hafnium silicates calculated by their peak heights and the ratio ($\gamma_{\text{ZS}}/\beta_{\text{ZS}}$) similarly calculated for zirconium silicates are shown in Fig. 13(b). The $\gamma_{\text{HS}}/\beta_{\text{HS}}$ value decreases with an increase in x value, while the $\gamma_{\text{ZS}}/\beta_{\text{ZS}}$ value becomes negligibly small at x not less than 0.31 after showing an almost constant value at $x=0.06$ and 0.15. Namely, both the two ratios are larger for smaller values of x . This might suggest that PLs γ_{HS} and γ_{ZS} are ascribed to silica. However, similar luminescence has not been observed, as reported in our previous paper.²⁶ Moreover, as mentioned above, it is more reasonable to assume that PLs γ_{HS} and γ_{ZS} are intrinsic to their respective silicates, that the dependence of the ratio ($\gamma_{\text{HS}}/\beta_{\text{HS}}$) on x is fairly similar to that of the ratio ($\gamma_{\text{ZS}}/\beta_{\text{ZS}}$) is supportive to this assumption.

The presence of a PL around 2.6 eV has been reported in literature as an example of PLs observable only in hafnium silicate and not in hafnia or silica.²⁷ In that paper,²⁷ the PL at 2.6 eV was attributed to defects peculiar to hafnium silicate such as lattice mismatch or oxygen dangling bonds induced in silica by incorporated hafnium atoms. As mentioned above, PLs γ_{HS} and γ_{ZS} are observed only in hafnium silicate and zirconium silicate, and neither hafnia, zirconia, nor silica has these PLs. Therefore, the possibility that the defects peculiar to silicates are responsible for the two PLs cannot be neglected. The same literature²⁷ suggested impurities as another possible cause of the PLs. However, this should not be the case, since the present results clearly indicate that the PLs γ_{HS} and γ_{ZS} are not due to impurities, similarly as in the cases of PLs β_{HS} and β_{ZS} .

Figure 14 shows PL spectra observed in HSA37 and ZSA15 thermally annealed in an oxygen atmosphere at 900 °C for 20 min. Here, all the measurements were done in sequence using the samples mounted on a vertically movable nonrotating rod in the PL measurement chamber so that comparison of the PL intensities among different samples becomes possible. A clear decrease in intensity by the thermal annealing is seen for all PLs β_{HS} , β_{ZS} , γ_{HS} , and γ_{ZS} . Especially in PLs γ_{HS} and γ_{ZS} , the decrease is significant. It has been reported that hafnia or zirconia is phase separated from silicates by thermal annealing at temperatures above 800 °C for hafnium silicate and above 900 °C for zirconium silicate.^{28–30} This should reduce the intensity of the PL pecu-

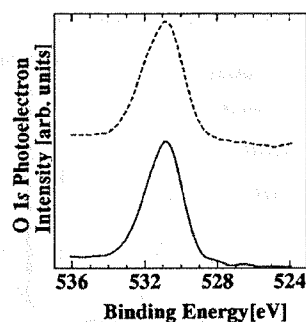


FIG. 15. O 1s photoelectron spectra obtained for $\text{Hf}_{0.54}\text{Si}_{0.46}\text{O}_{1.6}$ before (solid line) and after (dashed line) the thermal annealing at 900 °C.

liar to silicates. Therefore, by assuming that the phase separation also occurred in HSA37 and ZSA15, the decrease in intensity for PLs γ_{HS} and γ_{ZS} by the thermal annealing can be explained. On the other hand, such separation into the two substances should not affect the intensities of PLs β_{HS} and β_{ZS} , if it is reasonable to assume that the two PLs are identical to PLs β_{H} and β_{Z} induced in hafnia or zirconia, as we already discussed. This is supportive to the result that the intensities of PLs β_{H} and β_{Z} do not decrease so much by the thermal annealing.

In order to confirm the possibility of occurrence of phase separation by the thermal annealing, an XPS measurement was performed with a sample having a structure $\text{Hf}_{0.54}\text{Si}_{0.46}\text{O}_{1.6}$. By the phase separation, the XPS peak due to O 1s electrons is known to show two distinct spectral features at core level binding energies close to those of silica at ~ 532.4 eV and hafnia or zirconia at ~ 530 eV.²⁸ Since the XPS O 1s spectra shown in Fig. 1 do not have such features, all the samples were not phase separated before postannealing at 900 °C. Its shape does not change even after the postannealing at 900 °C as shown in Fig. 15, indicating that the annealed silicate is not phase separated. Still, there is a possibility that the separated hafnia or zirconia is not large enough, or is not present in the surface layer as thin as ~ 5 nm that is detectable by XPS.

In order to further obtain information about the excitation of respective PLs, their PLE spectra were measured. Figure 16(a) shows PLE spectra of PLs β_{HS} and γ_{HS} , while Fig. 16(b) shows those of PLs β_{ZS} and γ_{ZS} . The PLE spectra of PLs β_{HS} and β_{ZS} are very similar to those of PLs γ_{HS} and γ_{ZS} , respectively. This indicates that the excitation process is almost the same between PLs β_{HS} and γ_{HS} , and that so is the excitation process for PLs β_{ZS} and γ_{ZS} . Moreover, the onset of PLE spectrum shifts toward a lower energy with an increase in x for all the PLs β_{HS} , β_{ZS} , γ_{HS} , and γ_{ZS} . The PLE spectra of PLs α_{H} and α_{Z} , which were observed in the HA and ZA samples that had been thermally annealed in an oxygen atmosphere at 900 °C for 20 min, are also shown in Fig. 16. Their onsets are located at higher energies than those of PLs β_{H} and β_{Z} as reported in our previous paper.²⁵

Figure 17 shows VUV absorption spectra measured in the two silicates. For amorphous materials, photon absorption can be expressed by the following equation:³¹

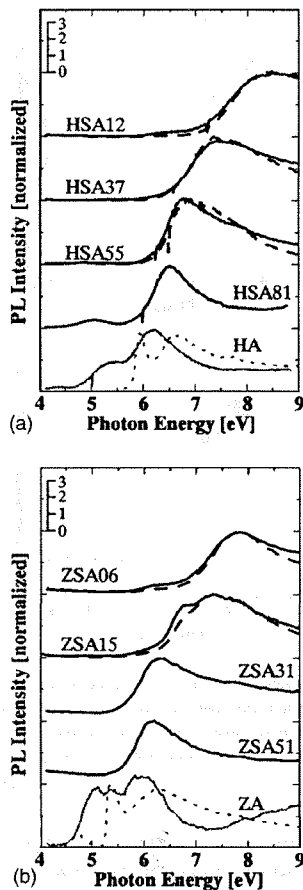


FIG. 16. (a) PLE spectra for β_{HS} (solid lines) and γ_{HS} (dashed lines) for hafnium silicates and α_{H} (light dotted line) and β_{H} (light solid line) for hafnia. (b) Those for β_{ZS} (solid lines) and γ_{ZS} (dashed lines) for zirconium silicates and α_{Z} (light dotted line) and β_{Z} (light solid line) for zirconia.

$$ah\nu \propto (h\nu - E_{\text{opt}})^2, \quad (2)$$

where α and $h\nu$ are the absorption coefficient and photon energy, respectively. The optical band gap energy E_{opt} or the interband photon absorption energy between the valence and conduction bands, estimated by fitting each spectrum to Eq. (2), shifts to a lower energy with an increase in x . In common with all the samples, the onset of the absorption is not steep. This is due to tail states around the band edges resulting from typical nature of amorphous materials. Hereafter, the onset energy of absorption is referred to as E_{tail} . In our previous paper,²⁵ we reported that the threshold energies of PLE spectra for PLs α_{H} and α_{Z} in hafnia and zirconia are quite similar to their E_{opt} values, while those of PLE spectra for PLs β_{H} and β_{Z} are similar to E_{tail} . Therefore, it is highly probable that PLs α_{H} and α_{Z} are excited due to the interband absorption, while PLs β_{H} and β_{Z} seem to be excited by photon absorption to tail states located at the band edges.²⁵ Since PLs β_{HS} and β_{ZS} are, respectively, very similar to PLs β_{H} and β_{Z} , they should be also excited by photon absorption to tail states. In order to confirm this, E_{tail} values in both silicates were estimated and were compared with PLE threshold energies for PLs β_{HS} and β_{ZS} . It is assumed that E_{tail} can be also estimated using Eq. (2) by substituting E_{tail} for E_{opt} .

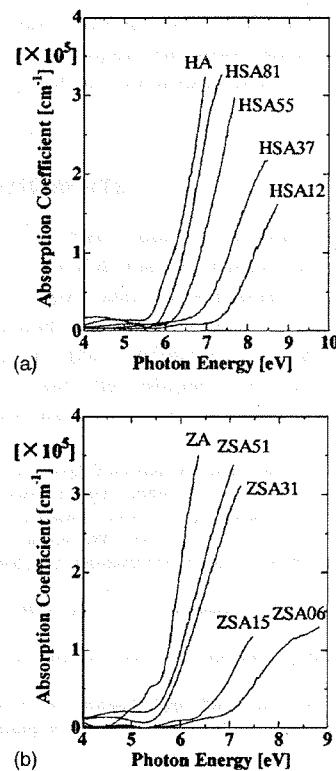


FIG. 17. VUV absorption spectra measured for hafnium silicates (a) and zirconium silicates (b).

Here, in replotting the absorption curves shown in Fig. 17 in accordance with Eq. (2), the initial onset portions were used to estimate E_{tail} . Furthermore, by assuming that a similar relationship holds between the threshold energy of PLE and the PLE spectrum and by substituting PLE threshold energy for E_{opt} and PL intensity for α , the threshold energies for PLs β_{HS} and β_{ZS} were estimated. These two estimated energies are shown in Fig. 18, where the broken lines are drawn as guides to eyes to show the slope of 1. The PLE threshold energies for PLs β_{HS} and β_{ZS} are quite similar to the E_{tail} values in respective silicates. This indicates that PLs β_{HS} and β_{ZS} are induced similarly to the cases of PLs β_{H} and β_{Z} by excitation to tail states near the band edge. Furthermore, PLs γ_{HS} and γ_{ZS} are also excited by the same process since the PLE threshold energies of PLs γ_{HS} and γ_{ZS} are almost the same as those of PLs β_{HS} and β_{ZS} as shown in Fig. 16.

As shown in Figs. 13(a) and 17, E_{opt} decreases with an increase in x , while the peak energies of PLs β_{HS} and β_{ZS} change by only 0.2 eV, and those of PLs γ_{HS} and γ_{ZS} do not change. Moreover, as mentioned in relation to Fig. 8, the small shift in peak energy for PLs β_{HS} and β_{ZS} is attributable to the change in constituent ratio of the 2.9 and 3.2 eV sub-components with an increase in x . This fact indicates that these PLs are most likely due to radiative recombination in the band gap between two localized states that have the same energy difference irrespective of x . To sum up, we can conclude that all the PLs β_{HS} , β_{ZS} , γ_{HS} , and γ_{ZS} arise from the same luminescence process; electrons (or holes) are excited to tail states at the band edges and then relax to the upper

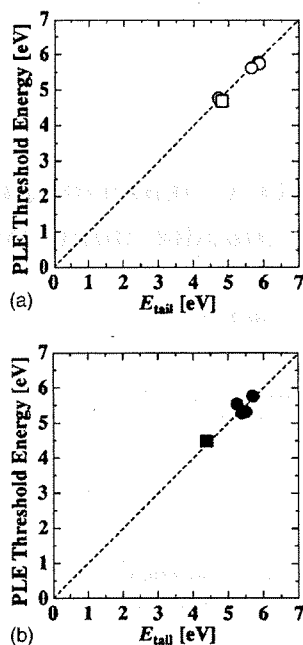


FIG. 18. (a) Relations between the PLE threshold energy of PL β_{HS} or β_{H} and the energy at absorption edge due to band tail states E_{tail} , observed for hafnium silicates (open circles) and hafnia (open square). (b) Similar relations observed for PL β_{ZS} in zirconium silicates (solid circles) and for PL β_{Z} in zirconia (solid square).

state of the luminescent centers fixed in the band gap. The electrons (or holes) are then deexcited to the lower state and induce the luminescence. However, the fact that the change in intensity as a function of x , namely, the hafnium or zirconium content, is different between PLs β_{HS} and γ_{HS} and also the fact that PL γ_{HS} is thermally annealed more completely than PL β_{HS} indicate that the origin of PL β_{HS} is different from that of PL γ_{HS} . Similarly, the origin of PL β_{ZS} is different from that of PL γ_{ZS} .

IV. CONCLUSION

Hafnium and zirconium silicate samples with various compositions were deposited by PECVD and their PL characteristics induced by ultraviolet photons were studied. When the samples are irradiated by SR photons at 8.0 eV, a broad PL band is observed around 2.0–5.0 eV in both the silicates. The PL band is Gaussian fitted by two components with peaks around 2.8–3.0 eV (PL β_{HS}) and 3.8 eV (PL γ_{HS}) for hafnium silicates and those around 2.7–3.0 eV (PL β_{ZS}) and 3.8 eV (PL γ_{ZS}) for zirconium silicates. Similar PL spectra are observed irrespective of the difference in source alkoxide for hafnium silicates, which indicates that PLs β_{HS} and γ_{HS} are not due to impurities but intrinsic to hafnium silicates. The decay characteristics of PLs β_{HS} and β_{ZS} are very similar to each other, and they are also very similar to those of the PL components around 2.7–2.9 eV observed in hafnia (PL β_{H}) and zirconia (PL β_{Z}). Therefore, it is assumed that the origins of PLs β_{HS} , β_{ZS} , β_{H} , and β_{Z} are similar. By comparing their PLE spectra with VUV absorption spectra, it is assumed that hafnium silicate, zirconium silicate, hafnia,

and zirconia have luminescent centers in their band gaps with their respective upper and lower states that have a certain fixed energy difference irrespective of hafnium or zirconium content.

ACKNOWLEDGMENTS

This work was partly done in the Joint Studies Program (2000–2005) of UVSOR Facility, Institute for Molecular Science, Okazaki, Japan, and was supported by a Grant-in-Aid from Japan Society for the Promotion of Science for Scientific Research (B) (No. 16360160). A High-Tech Research Center Grant from the Ministry of Education, Culture, Sports, Science and Technology of Japan is also appreciated.

- ¹International Technology Roadmap for Semiconductors, International Sematech, <http://public.itrs.net/> (2004).
- ²D. A. Muller, T. Sorsch, S. Morrio, F. H. Baunann, K. E. Lutterodt, and G. Timp, *Nature (London)* **399**, 758 (1999).
- ³J. H. Stathis and D. J. DiMaria, *Tech. Dig. - Int. Electron Devices Meet.* **1998**, 167.
- ⁴B. Brar, G. D. Wilk, and A. C. Seabaugh, *Appl. Phys. Lett.* **69**, 2728 (1996).
- ⁵G. D. Wilk, R. M. Wallace, and J. M. Anthony, *J. Appl. Phys.* **89**, 5243 (2001).
- ⁶G. D. Wilk and R. M. Wallace, *Appl. Phys. Lett.* **76**, 112 (2000).
- ⁷B. H. Lee, L. Kang, R. Nieh, W. J. Qi, and J. C. Lee, *Appl. Phys. Lett.* **76**, 1926 (2000).
- ⁸W. J. Qi *et al.*, *Tech. Dig. - Int. Electron Devices Meet.* **1999**, 145.
- ⁹Y. H. Wu, M. Y. Yang, A. Chin, W. J. Chen, and C. M. Kwei, *IEEE Electron Device Lett.* **21**, 341 (2000).
- ¹⁰H. H. Tseng *et al.*, *Tech. Dig. - Int. Electron Devices Meet.* **2003**, 83.
- ¹¹D. A. Neumayer and E. Cartier, *J. Appl. Phys.* **90**, 1801 (2001).
- ¹²W. J. Zhu, T. P. Ma, T. Tamagawa, J. Kim, and Y. Di, *IEEE Electron Device Lett.* **23**, 97 (2002).
- ¹³J. P. Chang and Y. S. Lin, *J. Appl. Phys.* **90**, 2964 (2001).
- ¹⁴M. Matsuoka, S. Isotani, J. F. D. Chubaci, S. Miyake, Y. Setsuhara, K. Ogata, and N. Kuratani, *J. Appl. Phys.* **88**, 3773 (2000).
- ¹⁵H. Kato, T. Nango, T. Miyagawa, T. Katagiri, K. S. Seol, and Y. Ohki, *J. Appl. Phys.* **92**, 1106 (2002).
- ¹⁶G. D. Wilk, R. M. Wallace, and J. M. Anthony, *J. Appl. Phys.* **87**, 484 (2000).
- ¹⁷N. Ikarashi and K. Manabe, *J. Appl. Phys.* **94**, 480 (2003).
- ¹⁸J. Morais, E. B. O. da Rosa, L. Miotti, R. P. Pezzi, I. J. R. Baumvol, A. L. P. Rotondaro, M. J. Bevan, and L. Colombo, *Appl. Phys. Lett.* **78**, 2446 (2001).
- ¹⁹M. Koike *et al.*, *Tech. Dig. - Int. Electron Devices Meet.* **2003**, 107.
- ²⁰H. Y. Yu *et al.*, *Appl. Phys. Lett.* **81**, 376 (2002).
- ²¹R. S. Johnson, J. G. Hong, C. Hinkle, and G. Lucovsky, *J. Vac. Sci. Technol. B* **20**, 1126 (2002).
- ²²W. J. Zhu, T. P. Ma, S. Zafar, and T. Tamagawa, *IEEE Electron Device Lett.* **23**, 597 (2002).
- ²³J. F. Conley, Y. Ono, R. Solanki, G. Stecker, and W. Zhuang, *Appl. Phys. Lett.* **82**, 3508 (2003).
- ²⁴A. Y. Kang, P. M. Lenahan, and J. F. Conley, *Appl. Phys. Lett.* **83**, 3407 (2003).
- ²⁵T. Ito, M. Maeda, K. Nakamura, H. Kato, and Y. Ohki, *J. Appl. Phys.* **97**, 054104-1 (2005).
- ²⁶K. S. Seol, A. Ieki, Y. Ohki, H. Nishikawa, and M. Tachimori, *J. Appl. Phys.* **79**, 412 (1996).
- ²⁷E. Vainonen-Ahlgren, E. Tois, T. Ahlgren, L. Khriachtchev, J. Marles, S. Haukka, and M. Tuominen, *Comput. Mater. Sci.* **27**, 65 (2003).
- ²⁸G. B. Rayner, D. Kang, and G. Lucovsky, *J. Non-Cryst. Solids* **338–340**, 151 (2004).
- ²⁹S. Saito, Y. Matsui, K. Torii, Y. Shimamoto, M. Hiratani, and S. Kimura, *Jpn. J. Appl. Phys., Part 2* **42**, L1425 (2003).
- ³⁰J. Kim and K. Yong, *J. Cryst. Growth* **263**, 442 (2004).
- ³¹N. F. Mott and E. A. Davis, in *Electronic Processes in Non-Crystalline Materials*, 2nd ed. (Clarendon, Oxford, 1979), p. 289.

Improvement in electrical properties of hafnium and zirconium silicates by postnitriding

T Ito¹, H Kato², T Nango¹ and Y Ohki¹

¹ Department of Electrical Engineering and Bioscience, Waseda University, Shinjuku-ku, Tokyo 169-8555, Japan

² Diamond Research Center, National Institute of Advanced Industrial Science and Technology (AIST), Umezono, Tsukuba-shi, Ibaraki 305-8565, Japan

E-mail: prince@suou.waseda.jp

Received 15 February 2006, in final form 6 May 2006

Published 19 June 2006

Online at stacks.iop.org/JPhysCM/18/6009

Abstract

Hafnium and zirconium silicate films were deposited on a silicon substrate and the effects of postannealing on their electrical properties were investigated. When the films are postannealed in nitrogen monoxide (NO), the leakage current becomes lower by more than one order of magnitude as compared with that of the as-deposited films. The capacitance–voltage (C – V) hysteresis width is also decreased drastically by the NO postannealing. From electron spin resonance spectroscopy, it is indicated that paramagnetic defects at the interface between the film and the substrate are responsible for the leakage current and the C – V hysteresis. It is also indicated by x-ray photoelectron spectroscopy that the postnitridation effectively terminates these interface defects and contributes to the improvement in electrical properties.

1. Introduction

According to guidelines for manufacturing processes for the future complementary metal–oxide–semiconductor (CMOS) technology such as the International Technology Roadmap for Semiconductors (ITRS), the thickness of the gate silicon dioxide is expected to be scaled down to a value below its thinnest limit in the near future [1]. In this thickness region, silicon dioxide would not maintain its insulating property, since direct tunnelling dominates the leakage current [2, 3]. In order to overcome this difficulty, several attempts to increase the physical thickness have been carried out using materials with a higher permittivity, while keeping the equivalent silicon dioxide thickness unchanged [4–6]. However, these materials contain various densities of defects, many of which will get charged and cause an increase in their leakage currents. Therefore, finding an adequate method to improve their electrical properties is necessary.

We have successfully deposited hafnium silicate and zirconium silicate by plasma-enhanced chemical-vapour deposition (PECVD) and examined their energy band profiles and

photoluminescence characteristics [7, 8]. In the present paper, we investigate the effects of postannealing on their electrical properties, in order to find a clue to the improvement.

2. Samples and experimental procedures

Hafnium silicate and zirconium silicate films were deposited using a PECVD technique. The source gases were tetraethoxysilane [TEOS: $\text{Si}(\text{OC}_2\text{H}_5)_4$] and a hafnium alkoxide [$\text{Hf}(\text{O}-i\text{-C}_3\text{H}_7)_4$] or a zirconium alkoxide [$\text{Zr}(\text{O}-i\text{-C}_3\text{H}_7)(\text{C}_{11}\text{H}_{19}\text{O}_2)_3$]. Oxygen, used as an oxidation gas, was excited with an rf power of 13.56 MHz through capacitive coupling. The TEOS was vaporized and transported at 70 °C into the 'tail flame' of the oxygen plasma. The hafnium or zirconium alkoxide was vaporized and transported at 220 °C into the oxygen plasma using argon gas as a carrier and diluent gas. The gas flow rate was controlled with a mass-flow controller. The films were deposited onto a p-type silicon monocrystal wafer (100) set on a stage whose temperature was kept at 400 °C.

The elemental composition and chemical structure of the deposited films were estimated through x-ray photoelectron spectroscopy (XPS, JEOL JPS-9010TR) and x-ray diffraction (XRD) spectroscopy (Rigaku RAD-1C). The XPS peaks ascribable to Hf–O–Si or Zr–O–Si bonds appeared, while no peaks to be ascribed to Hf–Si or Zr–Si silicide bonds were seen. No crystalline peaks appeared in the XRD spectra of both silicates. Therefore, the deposited films were confirmed to be amorphous silicates with the chemical formula $\text{Hf}_{0.43}\text{Si}_{0.57}\text{O}_{1.8}$ or $\text{Zr}_{0.32}\text{Si}_{0.68}\text{O}_{2.0}$. Here, the estimation error in the chemical composition is about 10%. The film thickness was measured to be about 80 nm for both silicates by ellipsometry (Ulvac ESM-1) with a He–Ne laser at a wavelength of 632.8 nm.

For postannealing, the deposited films were kept at 900 °C for 60 s in a rapid thermal annealing apparatus filled either with nitrogen monoxide (NO), oxygen (O_2) or nitrogen (N_2) at a pressure of $\sim 1.0 \times 10^5$ Pa. The postannealing in NO is known to cause nitridation and oxidation, while that in O_2 causes oxidation [9, 10]. No such chemical changes are expected in the N_2 postannealing.

Fourier transform infrared (FT-IR) absorption spectroscopy was carried out before and after the postannealing in a JEOL JIR-WINSPEC50 spectrometer. On the other hand, electron spin resonance (ESR) spectra were examined for the samples put in a pure silica glass cell with a JEOL JES-FA 300 spectrometer at the X-band frequency at room temperature in air. In order to obtain the g -values, a standard Mn^{2+} signal marker was used. The number of paramagnetic spins was evaluated by double numerical integration of a first-derivative ESR spectrum and by comparison with the signal from diphenylpicrylhydrazyl ($g = 2.0036$) of a known weight. The accuracy of estimation is believed to be $\pm 20\%$.

Electrical properties were examined at room temperature for the sample having a metal–insulator–semiconductor structure consisting of the lower silicon substrate, the film and an evaporated gold upper electrode with an effective area of 2.8×10^{-3} cm². The leakage current was measured using a high resistance meter (Advantest R8340) by applying a positive dc voltage to the upper electrode while changing its average field value from 0 to 14 MV cm⁻¹ in a stepwise manner with a step of 0.03 MV cm⁻¹. The capacitance–voltage (C – V) characteristics were obtained at 1 MHz using a high-frequency C – V meter (Sanwa Mega Bytek MI-494) by sweeping the voltage first from negative to positive at a constant rate of 0.4 V s⁻¹ and then by sweeping it inversely.

3. Results and discussion

Figure 1 shows the current density J as a function of the electric field intensity E obtained for the hafnium and zirconium silicates. The J – E curves clearly vary for the different

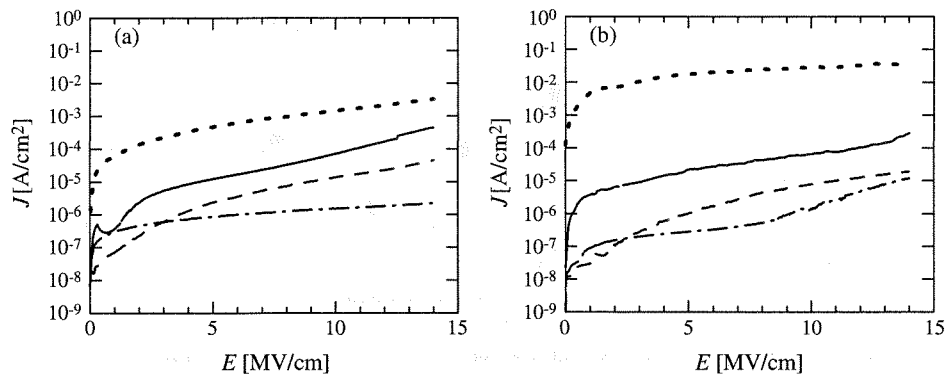


Figure 1. (a) Relations between the electric field intensity E and the current density J observed for hafnium silicate before (solid curve) and after postannealing in NO (dashed-dotted curve), O_2 (dashed curve) or N_2 (dotted curve). (b) Similar relations observed for zirconium silicate before (solid curve) and after postannealing in NO (dashed-dotted curve), O_2 (dashed curve) or N_2 (dotted curve).

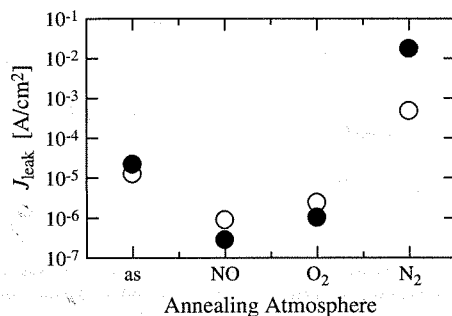


Figure 2. Changes in the leakage current density J_{leak} with the difference in the postannealing atmosphere. Open and closed symbols are the data obtained for hafnium silicate and zirconium silicate, respectively.

postannealing atmospheres. For both silicates, J becomes smallest in the case of O_2 annealing at $E < 3 \text{ MV cm}^{-1}$. However, at $E > 3 \text{ MV cm}^{-1}$, J is most effectively reduced by the NO annealing. According to ITRS, CMOS devices with a SiO_2 gate dielectric film are to be operated at 10 MV cm^{-1} [1]. The permittivity values of the present silicate samples were measured to be about 7, nearly twice as high as that of SiO_2 . Therefore, the equivalent thickness of the present film turns out to be twice the SiO_2 thickness. Therefore, it would be better to compare the leakage current density J_{leak} at $E = 5 \text{ MV cm}^{-1}$. The changes in J_{leak} due to the difference in the postannealing atmosphere are compared in figure 2 for the two silicates. Regardless of whether the sample is hafnium or zirconium silicate, the value of J_{leak} is lower in the NO and O_2 postannealed samples than in the as-deposited samples, whereas it is higher in the N_2 postannealed samples. In particular, in the NO postannealed samples, J_{leak} decreases by more than one order of magnitude as compared to the value in as-deposited samples. Therefore, it is clear from figure 2 that the NO postannealing is quite effective in reducing J_{leak} in both the silicates.

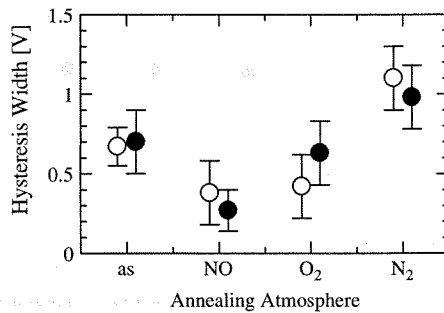


Figure 3. Changes in the hysteresis width with the postannealing atmosphere. Open and closed symbols are the data obtained for hafnium silicate and zirconium silicate, respectively.

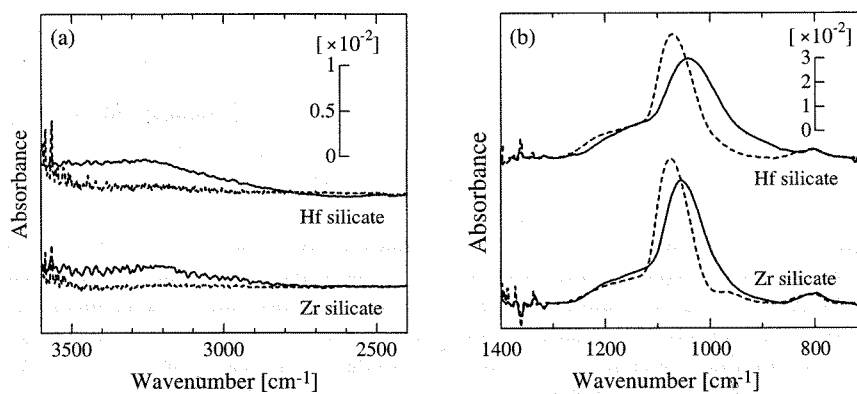


Figure 4. FT-IR spectra obtained for hafnium and zirconium silicates from 2400 to 3600 cm^{-1} (a) and around 1000 cm^{-1} (b). The solid and broken curves are the spectra before and after the postannealing in NO, respectively.

Figure 3 shows the C - V hysteresis widths measured before and after the postannealing. For both silicates, the width decreases with NO or O_2 postannealing, whereas it increases with N_2 postannealing. This changing pattern is very similar to that of J_{leak} shown in figure 2. The hysteresis width is known to reflect the number of charge traps in the bulk or at the interface [11, 12]. Therefore, the decrease in the number of charge traps, which can act as leakage paths for carriers, is considered to bring about a lower leakage current.

In order to investigate the reasons for the changes in J_{leak} and in the hysteresis width with the postannealing atmosphere, FT-IR and ESR measurements were carried out. Figure 4 shows FT-IR spectra obtained before and after the postannealing in NO. The absorption peaks around 1000 and 3400 cm^{-1} seen in the as-deposited samples are attributable to Si-O and OH bonds, respectively. Here, the OH bonds seem to be contained as impurities in the samples. In figure 4, the OH bonds clearly disappear with NO postannealing. Similar disappearance was confirmed in the O_2 and N_2 postannealed samples, although the spectra are not shown here. This means that hydrogen-related impurities are desorbed by the postannealing, regardless of its atmosphere.

The wavenumber K of the FT-IR absorption peak around 1000 cm^{-1} due to Si-O bonds can be an indicator of the structural distortion. The bond angle $\angle\text{SiOSi}$, denoted by θ , is known

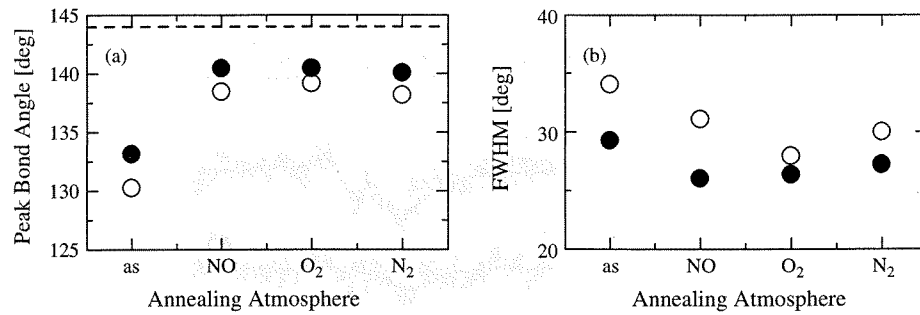


Figure 5. Changes in the peak value (a) and FWHM (b) of the bond angle $\angle\text{SiOSi } \theta$ with the postannealing atmosphere. Open and closed symbols represent the data obtained for hafnium silicate and zirconium silicate, respectively. The broken line in (a) is drawn as a guide to the eyes to show the value of 144° .

to follow the equation [13]

$$K = a \left[\frac{2}{m} \left(\alpha \sin^2 \frac{\theta}{2} + \gamma \cos^2 \frac{\theta}{2} \right) \right]^{1/2} \quad (1)$$

Here, K is in cm^{-1} , a and γ are constants ($5.3 \times 10^{-12} \text{ s cm}^{-1}$ and 100 N m^{-1} , respectively) and m is the mass of an oxygen atom. The α -value might in principle be able to vary with the modification of the bond length of Si–O, $d_{\text{Si-O}}$. However, it has been reported that the major cause of K variation is due to θ and not to changes in α through $d_{\text{Si-O}}$ for the range $120^\circ < \theta < 150^\circ$ in the case of silicate materials [13]. Therefore, variations in $d_{\text{Si-O}}$ and α are neglected and α is regarded as a constant value of 600 N m^{-1} [13]. By substituting K into equation (1), the FT-IR spectra were converted to those expressed as a function of θ . Figure 5 shows the peak value and the full width at half maximum (FWHM) of θ of such converted spectra. The peak bond angle approaches 144° , the most stable value of θ [13], for all the postannealing atmospheres. The value of FWHM also decreases with postannealing. Therefore, it is clear that the postannealing reduces the randomness in microscopic structure regardless of its atmosphere. The desorption of hydrogen-related impurities by the postannealing seems to play a role in the structural stabilization. However, since the dependences of J_{leak} and the hysteresis width on the annealing atmosphere shown in figures 2 and 3 are not similar to those of the peak value and FWHM of θ shown in figure 5, the structural randomness seems to have no direct relation to the electrical properties.

Figure 6 shows ESR spectra obtained in zirconium silicate before and after postannealing. Although not so clear, the spectra are presumed from their shapes and g -values to be due to the P_b centre, which is an inherent point defect induced by a lattice mismatch at an interface between Si and SiO_2 [14]. Figure 7 shows the change in the number of paramagnetic spins with postannealing estimated from figure 6. The NO annealing effectively eliminates the defects, while the N_2 annealing increases their number. This dependence of the spin number on the annealing atmosphere is similar to those of J_{leak} and the hysteresis width shown in figures 2 and 3. Therefore, it is highly probable that the defects causing the ESR spectra at the interface between the silicon substrate and the film are responsible for the increase in the leakage current and the hysteresis width.

To verify this assumption further, we now discuss how the NO postannealing reduces the number of interface defects. Since these interface defects are observable by ESR as shown in

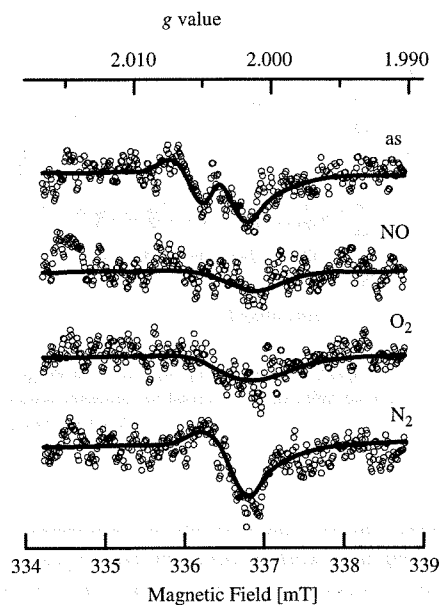


Figure 6. ESR spectra obtained for zirconium silicate before and after postannealing. The solid curves are drawn as a guide for the eyes.

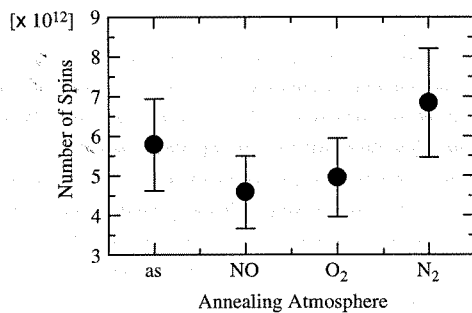


Figure 7. Change in the number of spins with the postannealing atmosphere obtained for zirconium silicate.

figure 6, they should have unpaired electrons. For SiO_2 deposited on a Si substrate, it has been reported that unpaired P_b centres at SiO_2/Si interfaces are terminated by the NO annealing, forming $\text{Si}_3\equiv\text{N}$ bonds and $\text{Si}_2=\text{N}-\text{O}$ -bonds [15]. As an analogy to this, unpaired centres in the present hafnium and zirconium silicates are also assumed to be terminated by the NO annealing. If this is the case, nitrogen will be observed at the interface. Figure 8 shows depth profiles of the XPS signals due to Hf, Si, O and N atoms obtained for hafnium silicate after the NO postannealing. At the depths from about 60 to 70 nm, the signal due to Si drastically increases, while those due to Hf and O decrease. This region corresponds to the interface between the silicon substrate and the hafnium silicate. Therefore, figure 8 clearly shows that the NO postannealing causes nitridation and effectively diminishes the interface defects.

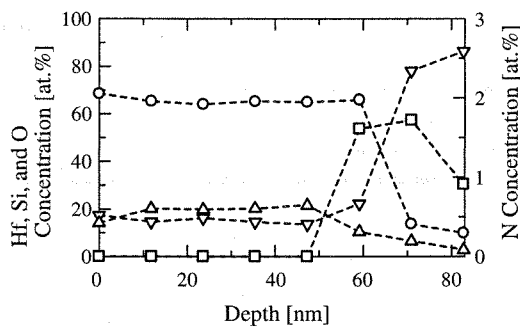


Figure 8. XPS depth profiles of Hf (triangles), Si (inverted triangles), O (circles) and N (squares) atoms obtained for hafnium silicate after the NO postannealing. The broken curves are drawn as a guide for the eyes.

Finally, the possibility of the relevance of any other causes to the decrease in J_{leak} is discussed. It is well known that silicon dioxide is grown at the interface between the high-permittivity dielectric film and the silicon substrate by thermal treatment in O_2 ambient [16]. Furthermore, it has been reported that interfacial oxide layers are also grown in the case of the N_2 annealing [17, 18], probably due to dissolved oxygen and/or reaction with detached oxygen from silicate. The interfacial layer can act as a barrier for carriers, which leads to the decrease in the leakage current. On the other hand, when the film is annealed in NO ambient, NO diffuses into the film and forms strong Si–N bonds at the interface [19–21], which suppresses the formation of interfacial oxide layers [21]. Therefore, the oxide layer thickness grown by the NO annealing must be thinner than that grown by the O_2 or N_2 annealing. This assumption is also supported by the fact that the zirconium silicate deposited in a NO atmosphere has a much thinner interfacial layer than the one deposited in an O_2 atmosphere [16, 22]. Therefore, if the decrease in J_{leak} is due to the growth of the interfacial layer during the postannealing, J_{leak} should be decreased for all the postannealing atmospheres and its reduction ratio should be the smallest in the NO postannealed samples among the three postannealed samples. However, this is not the case in the present result shown in figure 2. Therefore, the decrease in J_{leak} is not due to the growth in the interfacial oxide layer.

To summarize, structural randomness does not affect the electrical properties, while paramagnetic defects such as the P_b centres at the interface act as leakage paths and charge traps. Such defects can be eliminated effectively by nitridation through postannealing in NO ambient.

4. Conclusion

The effects of postannealing on the electrical properties of hafnium and zirconium silicate films deposited on a silicon substrate by PECVD were investigated. For both silicates, the leakage current and the C – V hysteresis width become smaller in the NO and O_2 postannealed samples than in the as-deposited samples, whereas they become larger in the N_2 postannealed samples. In particular, the NO postannealing significantly lowers these values. From FT-IR, ESR and XPS spectroscopy, it has become clear that paramagnetic defects such as the P_b centres at the interface between the film and the substrate are responsible for the leakage current, and that the NO postannealing effectively terminates these defects.

Acknowledgments

This work was partly supported by Grants-in-Aid from the Japan Society for the Promotion of Science (JSPS) for JSPS Fellows (No. 1205733) and for Scientific Research (B) (Nos 12450132 and 16360160). A High-Tech Research Center Grant from the Ministry of Education, Culture, Sports, Science and Technology of Japan is also appreciated.

References

- [1] <http://public.itrs.net>
- [2] Muller D A, Sorsch T, Morrio S, Baumann F H, Lutterodt K E and Timp G 1999 *Nature* **399** 758–61
- [3] Brar B, Wilk G D and Seabaugh A C 1996 *Appl. Phys. Lett.* **69** 2728–30
- [4] Wilk G D, Wallace R M and Anthony J M 2000 *J. Appl. Phys.* **87** 484–92
- [5] Wilk G D and Wallace R M 2000 *Appl. Phys. Lett.* **76** 112–4
- [6] Lee B H, Kang L, Nieh R, Qi W J and Lee J C 2000 *Appl. Phys. Lett.* **76** 1926–8
- [7] Ito T, Kato H, Nango T and Ohki Y 2004 *Japan. J. Appl. Phys.* **43** 8199–202
- [8] Ito T, Kato H and Ohki Y 2006 *J. Appl. Phys.* **99** 094106
- [9] Bhat M, Wristers D J, Han L-K, Yan J, Fulford H J and Kwong D-L 1995 *IEEE Trans. Electron Devices* **42** 907–14
- [10] Ota H, Yasuda N, Yasuda T, Morita Y, Miyata N, Tominaga K, Kadoshima M, Migita S, Nabatame T and Toriumi A 2005 *Japan. J. Appl. Phys.* **44** 1698–703
- [11] Kato H, Seol K S, Fujimaki M, Toyoda T, Ohki Y and Takiyama M 1999 *Japan. J. Appl. Phys.* **38** 6791–6
- [12] Sze S M 1981 *Physics of Semiconductor Devices* (New York: Wiley) p 379
- [13] Devine R A B 1993 *J. Non-Cryst. Solids* **152** 50–8
- [14] Jorgensen C, Svensson C and Ryden K H 1984 *J. Appl. Phys.* **56** 1093–6
- [15] Hegde R I, Tobin P J, Reid K G and Ajuria S A 1995 *Appl. Phys. Lett.* **66** 2882–4
- [16] Ahn H, Chen H-W, Landheer D, Wu X, Chou L J and Chao T-S 2004 *Thin Solid Films* **455/456** 318–22
- [17] Ho M-T, Wang Y, Brewer R T, Wielunski L S and Chabal Y J 2005 *Appl. Phys. Lett.* **87** 133103
- [18] Quevedo-Lopez M A, Chambers J J, Visokay M R, Shanware A and Colombo L 2005 *Appl. Phys. Lett.* **87** 012902
- [19] Lu H C, Gusev E, Yasuda N, Green M, Alers G, Garfunkel E and Gustafsson T 2000 *Appl. Surf. Sci.* **166** 465–8
- [20] Lu H C, Gusev E P, Garfunkel E, Busch B W, Gustafsson T, Sorsch T W and Green M L 2000 *J. Appl. Phys.* **87** 1550–5
- [21] Scheer K C, Rao R A, Muralidhar R, Bagchi S, Conner J, Lozano L, Perez C, Sadd M and White B E Jr 2003 *J. Appl. Phys.* **93** 5637–42
- [22] Chen H-W, Huang T-Y, Landheer D, Wu X, Moisa S, Sproule G I, Kim J K, Lennard W N and Chao T-S 2003 *J. Electrochem. Soc.* **150** C465–71

関連研究成果の詳細

Details of Related Research Results

プラズマ化学気相堆積により成膜した high-*k* 膜の X 線光電子分光

非会員 及川 圭太* (早稲田大学) 学生員 伊藤 俊秀 (早稲田大学)
 非会員 高瀬 雅之 (早稲田大学) 正員 大木 義路 (早稲田大学)
 非会員 加藤 宙光 (産総研)

X-ray photoelectron spectroscopy of high-*k* dielectric films synthesized by plasma-enhanced chemical-vapor deposition

Keita Oikawa, Non-member, Toshihide Ito, Student member, Masayuki Takase, Non-member,
 Yoshimichi Ohki, Member (Waseda University), Hiromitsu Kato, Non-member (AIST)

Abstract: Thin films were deposited by plasma-enhanced chemical-vapor deposition using hafnium-, zirconium-, and silicon-alkoxides. Their chemical compositions, bonding states, and band gap energies were estimated by X-ray photoelectron spectroscopy. As a result, they were confirmed to be hafnia, hafnium silicate, zirconia, and zirconium silicate with no silicides. From the O 1s photoelectron spectra, the binding energy of electrons in oxygen atoms decreases monotonically with an increase in hafnium or zirconium content, which indicates that the oxygen atom becomes more ionic. Furthermore, the band gap energy estimated by the photoelectron loss peak agrees with the optical band gap energy estimated by the vacuum ultraviolet absorption and it decreases with an increase in hafnium or zirconium content. When the hafnia or hafnium silicate films are compared with the zirconia or zirconium silicate films having the same content of hafnium or zirconium, the band gap energy is higher in hafnia or hafnium silicate than in zirconia or zirconium silicate.

Keywords: Plasma-enhanced chemical-vapor deposition, high-*k*, hafnia, hafnium silicate, zirconia, zirconium silicate

1. はじめに

現代の高度情報化社会において、電子デバイスの更なる高速化ならびに低消費電力化への要求は高まるばかりである。一方、これまでのような微細化による CMOS (Complementary Metal Oxide Semiconductor) デバイスの性能向上には限界が迫っている⁽¹⁾。その顕著な例がゲート絶縁膜の極薄化である。従来より用いられてきた SiO₂ ゲート絶縁膜の膜厚は 1nm 以下となり、電子の直接トンネリングによるリーク電流の増大が問題となっている⁽²⁾。そこで SiO₂ よりも誘電率の高い high-*k* 材料を用いたゲート絶縁膜が注目されている^(2,3)。high-*k* 絶縁膜を導入することで適切な物理的膜厚を確保しつつ、ゲート容量を増加させることができる。これによりトンネルリーク電流を抑制しながら、高い駆動電流を実現しデバイスの高速化が達成できる。

高誘電率ゲート絶縁膜が満足すべき要件としては、ワイドバンドギャップ、少ない界面準位密度、良好な熱的安定性などが挙げられる。これまでに high-*k* 材料の候補としてハフニア(HfO₂)^(4,7)、ハフニウムシリケート(Hf_xSi_(1-x)O_y)^(7,8)、ジルコニア(ZrO₂)^(5,7,9,10)、ジルコニウムシリケート(Zr_xSi_(1-x)O_y)^(7,8,11)などが研究されてきた。特にハフニウム系の絶縁膜は高い誘電率を有し、Si 基板との接合面における熱力学的安定性から high-*k* ゲート絶縁膜の有力候補と考え

られている。しかし、これら high-*k* 絶縁膜における欠陥や界面準位の起因についての理解はまだ不十分であり、更なる研究が必要である。

High-*k* 膜を成膜する手法には DC スパッタ、rf スパッタ、ゾル-ゲル法、化学気相堆積(CVD: Chemical-Vapor Deposition) 法などがある。CVD 法の中で、熱 CVD 法は高温に加熱された表面での化学反応により薄膜を作成するのに対して、プラズマ CVD 法はプラズマを利用することで低温でも化学的に活性化種を生成することができる。絶縁膜が高温におかれると結晶化するが、結晶粒界はリークパスとなることから、低温での堆積が望ましい。そこで、我々はプラズマ CVD 装置を用いた high-*k* 膜の堆積を行い、これまで多くの特性について報告してきた⁽¹²⁾。ここでは HfO₂、Hf_xSi_(1-x)O_y、ZrO₂、Zr_xSi_(1-x)O_y に関し、X 線光電子分光(XPS)の結果をもとに原子間の結合状態などを中心に報告する。

2. 実験方法

我々の使用したプラズマ CVD 装置は容量結合のプラズマ励起方式であり、ガラス管上部より導入された酸素は 13.56MHz、50-400W の高周波電源によりプラズマ化される。このプラズマに、気化させたハフニウムアルコキシド [Hf(O-*i*-C₄H₉)₄ または Hf(O-*i*-C₃H₇)₄]、ジルコニウムアルコキシド [Zr(O-*i*-C₄H₉)₄ または Zr(O-*i*-C₃H₇)(C₁₁H₁₉O₂)₃]、シリコン

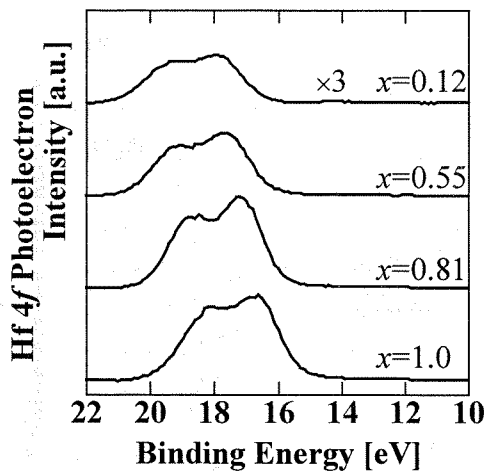


Fig. 1 Hf 4f photoelectron spectra.

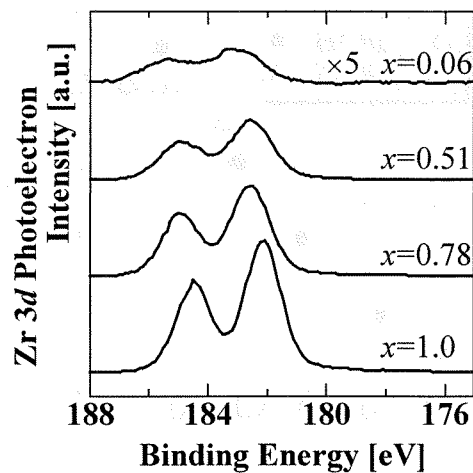


Fig. 2 Zr 3d photoelectron spectra.

アルコキシド[Si(OC₂H₅)₄]をマスフローコントローラーで流量を制御しつつ流し込み酸化させ、フッ化カルシウム基板とp形単結晶シリコン基板(面方位: 100 抵抗率: 0.9-1.5Ωcm)の2種類の基板上に薄膜を堆積した。基板温度は400-500°Cとし、シリコン基板については堆積前に0.5%フッ酸で自然酸化膜を除去し、純水で洗浄して使用した。

Mg Kα線(1253.6eV)を用いたXPS(JEOL JPS-9010TR)により、堆積膜の組成分析および結合状態分析を行った。このとき試料の帯電によるピークシフトは、束縛エネルギー284eVのC 1sスペクトルで補正した。さらに、単色化したAl Kα線(1486.6eV)を用いたXPSにより、O 1s光電子損失スペクトルを測定し、コアピークとの差から堆積膜のバンドギャップエネルギーを見積った。この値を、分子科学研究所UVSORのシンクロトロン放射光(750MeV)を使用した真空紫外光(VUV)吸収から見積った値と比較した。このとき、VUVに対し透明なフッ化カルシウムを基板として用いた。

3. 実験結果および考察

堆積膜のHf 4f、Zr 3d、Si 2pおよびO 1sの光電子スペクトルをFigs. 1-4に示す。これらのスペクトルから相対感度係数法を用いて組成を求めたところ、堆積膜はHf_xSi_(1-x)O_y、Zr_xSi_(1-x)O_yなる組成式で表わされ、各図中に記したHf、あるいはZrの組成比(x)を有していることがわかった。さらに各膜について、Oの組成比をxの関数として示すとFig. 5に示すように変化した。すなわち、xの増加につれて、膜は酸素過多から酸素欠乏へと変化する。

さらに、各スペクトルについて詳細に検討を加え各膜の化学結合状態を解析した。Fig. 1から16.7-17.9eVと18.1-19.3eV付近にHf-O結合に起因するHf 4f_{5/2}、Hf 4f_{7/2}ピークが確認できる。また、14eV付近にHf-Si結合起因のピーク⁽⁷⁾は観測されないことから、リーク電流を増加させる原因となるシリサイド⁽¹³⁾は形成されていないと言える。同様にFig. 2のZr 3d光電子スペクトルにおいても、182.1-183.1eVと184.5-185.4eV付近にZr-O結合に起因する

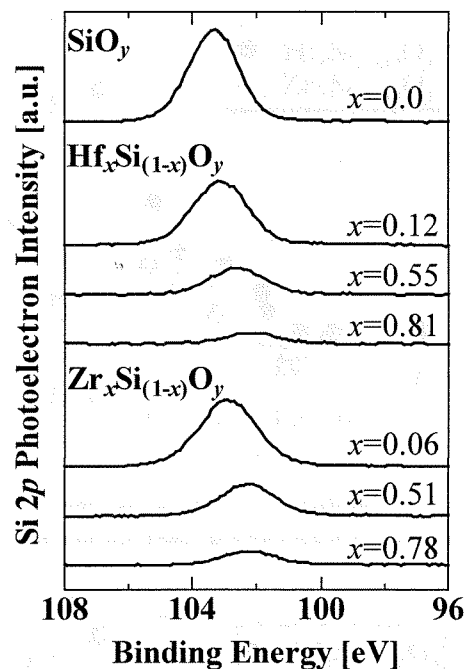


Fig. 3 Si 2p photoelectron spectra.

Zr 3d_{3/2}、Zr 3d_{5/2}ピークが見られる一方、180eV付近にZr-Si結合のピーク⁽⁷⁾は観測されない。また、Fig. 3のSi 2pの光電子スペクトルにおいて、Si-O結合起因のピークが観察できる。つぎにO 1sの光電子スペクトルについては、HfO_yのO-Hf結合およびZrO_yのO-Zr結合のピークは530eV付近⁽⁷⁾、SiO₂のO-Si結合のピークは533eV付近⁽¹⁴⁾、シリケートでは530-533eV付近^(7,15)に現れると報告されており、Fig. 4の結果と一致している。Figs. 1-4の結果を総合して判断すると所望の通りのハフニア、ハフニウムシリケート、ジルコニア、ジルコニウムシリケート、すなわちHfO_y、Hf_xSi_(1-x)O_y、ZrO_y、Zr_xSi_(1-x)O_yが堆積されていることがわかる。

ところで、同一の結合ピークに対するXPSピークであっ

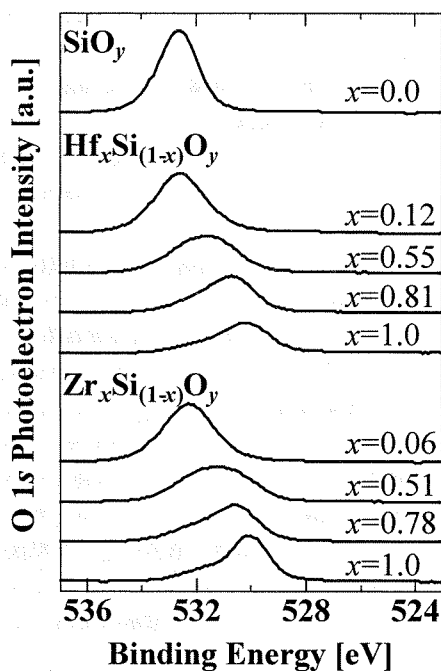


Fig. 4 O 1s photoelectron spectra.

でも、電子をとりまく周辺環境の変化によって化学シフトが生じる。この化学シフトに注目して、結合状態をさらに解析した。一般に HfO_y や ZrO_y はイオン結合性が強く、 SiO_2 は共有結合性が強いことが知られている。このためシリケート膜はイオン結合と共有結合の中間状態にあると予想される。陽イオンよりの電子の XPS ピークは、クーロン引力により電子の束縛エネルギーが大きくなるため、中性原子に比べて高エネルギー側へシフトする。一方、陰イオンの場合低エネルギー側へシフトする。共有結合された原子よりの電子においては、化学シフトは小さくなる。Fig. 4 によれば O 原子は組成 x の増加とともに束縛エネルギーが減少する。これは組成がイオン結晶である HfO_y や ZrO_y に近づくほど、O 原子のイオン結合性が強くなることと符合している。ところが Figs. 1, 2 によれば、シリケートにおける Hf, Zr 原子は HfO_y 、 ZrO_y に比べて束縛エネルギーが大きい。同様に、Fig. 3 によればシリケートにおける Si 原子は SiO_2 よりも束縛エネルギーが小さい。この結果は、 ZrO_2 、 ZrSiO_4 、 SiO_2 の化学シフトに関する量子化学計算⁽¹⁶⁾と一致している。同報告⁽¹⁶⁾によれば ZrSiO_4 における Zr 原子は ZrO_2 に比べて価数が大きく強いイオン結合性を有し、Si 原子は SiO_2 に比べて価数が小さく強い共有結合性を有している。

ゲート絶縁膜においてリーク電流を抑制するためには電子・正孔に対して 1eV 以上の障壁高さが必要となる。ゆえに、high- k 材料は大きなバンドギャップを有することが望まれる。そこで、O 1s 光電子損失スペクトルから堆積膜のバンドギャップエネルギー E_{loss} を見積った。Fig. 6 に E_{loss} の組成 x 依存性を示す。両シリケートにおいて組成 x の増加とともに E_{loss} の減少が見られること、および各試料における E_{loss}

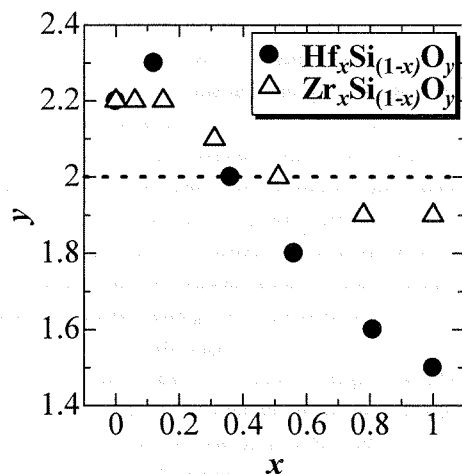


Fig. 5 Relation between composition ratios x and y . The broken line represents the stoichiometric ratio.

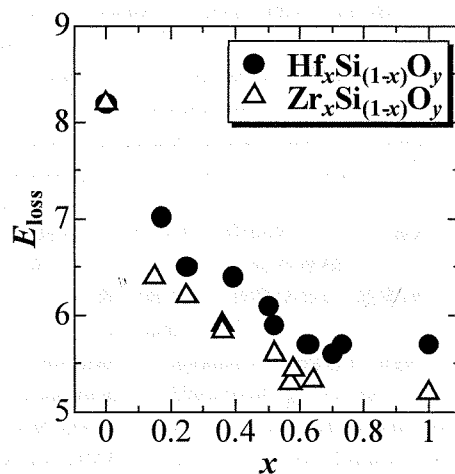


Fig. 6 Band gap energy (E_{loss}) estimated from the O 1s photoelectron loss peaks as a function of the composition x .

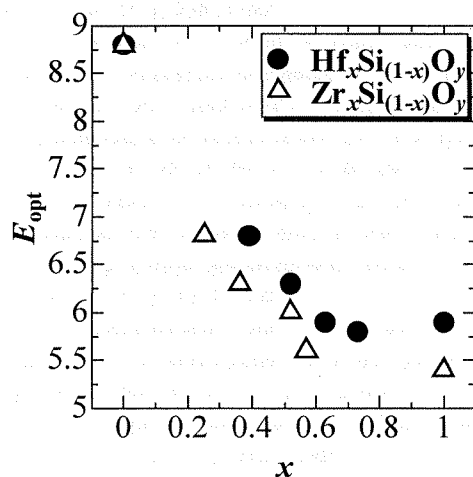


Fig. 7 Band gap energy (E_{opt}) estimated from the VUV absorption spectra as a function of the composition x .

の値は、 HfO_2 、 ZrO_2 、 SiO_2 のバンドギャップが順に $5.70\text{eV}^{(17)}$ 、 $5.65\text{eV}^{(17)}$ 、 $8.9\text{eV}^{(18)}$ であることを考えたとき、妥当な結果である。また、組成 $x < 0.6$ の範囲で x の増大により E_{loss} が急激に減少している。Hf や Zr の d 軌道は HfO_2 や ZrO_2 の伝導帯の底を形成すると報告されている⁽⁸⁾ので、 $x \geq 0.6$ で伝導帯底にバンドが形成されたのちは、 E_g がほぼ一定になると思われる。

Fig. 6 の結果をさらに検証するため、VUV 吸収から堆積膜の光学的バンドギャップエネルギー E_{opt} を見積った。一般にバンド間遷移吸収は次式で表わせる⁽¹⁹⁾。

$$\alpha h\nu \propto (h\nu - E_{\text{opt}})^2 \quad (1)$$

ここで α 、 $h\nu$ 、 E_{opt} はそれぞれ吸収係数、光子エネルギー、光学的バンドギャップである。

式(1)を用いて吸収スペクトルから E_{opt} を見積った結果を Fig. 7 に示す。両シリケートにおいて組成 x の増加とともに $x < 0.6$ の範囲で E_{opt} が急激に減少すること、ならびに E_{opt} は $\text{Zr}_x\text{Si}_{(1-x)}\text{O}_y$ より $\text{Hf}_x\text{Si}_{(1-x)}\text{O}_y$ の方が大きいことなどが確認でき、Fig. 6 の結果が検証できた。

4. まとめ

プラズマ CVD 装置を用いてハフニウム、ジルコニウム、シリコンのアルコキシドを酸化させて薄膜を堆積させ、XPS により、組成分析、結合状態分析およびバンドギャップ E_{loss} の見積りを行った。堆積膜は、シリサイド成分を含まぬ所望のハフニア、ハフニウムシリケート、ジルコニア、ジルコニウムシリケートであること、および Hf、Zr の組成比(x)が増加しハフニア、ジルコニアに近づくほど O 原子のイオン結合性が強くなるのがわかった。 E_{loss} は組成 x の増加とともに減少し、VUV 吸収から求めたバンドギャップ E_{opt} とほぼ一致した。

文 献

(1) International Technology Roadmap for Semiconductors, International Sematech <http://public.itrs.net/> (2004).
 (2) D. A. Muller, T. Sorsch, S. Morrio, F. H. Baunann, K. E. Lutterodt, and G. Timp: "The electronic structure at the atomic scale of ultrathin gate oxides", *Nature*, Vol. 399, No. 6738, p. 758 (1999).
 (3) G. D. Wilk, R. M. Wallace, and J. M. Anthony: "High-k gate dielectrics: Current status and materials properties considerations", *J. Appl. Phys.*, Vol. 89, No. 10, p. 5243 (2001).
 (4) H. H. Tseng, M. E. Ramon, L. Hebert, P. J. Tobin, D. Triyoso, J. M. Grant, Z. X. Jiang, D. Roan, S. B. Samavedam, D. C. Gilmer, S. Kalpat, C. Hobbs, W. J. Taylor, O. Adetutu, and B. E. White: "ALD HfO_2 using heavy water (D_2O) for improved MOSFET stability", *Tech. Dig. - Int. Electron Devices Meet.* 2003, p. 83.
 (5) D. A. Neumayer and E. Cartier: "Materials characterization of ZrO_2 - SiO_2 and HfO_2 - SiO_2 binary oxides deposited by chemical solution deposition", *J. Appl. Phys.*,

Vol. 90, No. 4, p. 1801 (2001).
 (6) W. J. Zhu, T. P. Ma, T. Tamagawa, J. Kim, and Y. Di: "Current transport in metal/hafnium oxide/silicon structure", *IEEE Electron Device Lett.*, Vol. 23, No. 2, p. 97 (2002).
 (7) G. D. Wilk, R. M. Wallace, and J. M. Anthony: "Hafnium and zirconium silicates for advanced gate dielectrics", *J. Appl. Phys.*, Vol. 87, No. 1, p. 484 (2000).
 (8) N. Ikarashi and K. Manabe: "Electronic structure analysis of Zr silicate and Hf silicate films by using spatially resolved valence electron energy-loss spectroscopy", *J. Appl. Phys.*, Vol. 94, No. 1, p. 480 (2003).
 (9) J. P. Chang and Y. S. Lin: "Highly conformal ZrO_2 deposition for dynamic random access memory application", *J. Appl. Phys.*, Vol. 90, No. 6, p. 2964 (2001).
 (10) M. Matsuoka, S. Isotani, J. F. D. Chubaci, S. Miyake, Y. Setsuhara, K. Ogata, and N. Kuratani: "Influence of ion energy and arrival rate on x-ray crystallographic properties of thin ZrO_x films prepared on Si(111) substrate by ion-beam assisted deposition", *J. Appl. Phys.*, Vol. 88, No. 6, p. 3773 (2000).
 (11) J. Morais, E. B. O. da Rosa, L. Miotti, R. P. Pezzi, I. J. R. Baumvol, A. L. P. Rotondaro, M. J. Bevan, and L. Colombo: "Stability of zirconium silicate films on Si under vacuum and O_2 annealing", *Appl. Phys. Lett.*, Vol. 78, No. 17, p. 2446 (2001).
 (12) 加藤宙光・宮川武・南向智広・大木義路・薛光洙・滝山真功: 「プラズマ化学気相堆積法によるハフニウムシリケート膜の堆積」, *放電学会誌 放電研究*, Vol. 44, No. 1/2, p. 69 (2001).
 (13) Y. Morisaki, T. Aoyama, Y. Sugita, K. Irino, T. Sugii, and T. Nakamura: "Ultra-thin($T_{\text{eff}}^{\text{mv}}=1.7\text{nm}$) Poly-Si-gated $\text{SiN}/\text{HfO}_2/\text{SiON}$ High-k Stack Dielectrics with High Thermal Stability (1050°C)", *Tech. Dig. - Int. Electron Devices Meet.* 2002, p. 861.
 (14) J. J. Chambers and G. N. Parsons: "Yttrium silicate formation on silicon: Effect of silicon preoxidation and nitridation on interface reaction kinetics", *Appl. Phys. Lett.*, Vol. 77, No. 15, p. 2385 (2000).
 (15) G. B. Rayner, Jr., D. Kang, Y. Zhang, and G. Lucovsky: "Nonlinear composition dependence of x-ray photoelectron spectroscopy and Auger electron spectroscopy features in plasma-deposited zirconium silicate alloy thin films", *J. Vac. Sci. Technol. B*, Vol. 20, No. 4, p. 1748 (2002).
 (16) M. J. Guittet, J. P. Crocombette and M. Gautier-Soyer: "Bonding and XPS chemical shifts in ZrSiO_4 versus SiO_2 and ZrO_2 : Charge transfer and electrostatic effects", *Phys. Rev. B*, Vol. 63, No. 12, p. 125117 (2001).
 (17) R. Puthenkottilakam and J. P. Chang: "An accurate determination of barrier heights at the HfO_2/Si interfaces", *J. Appl. Phys.*, Vol. 96, No. 5, p. 2701, (2004).
 (18) R. B. Laughlin: "Optical absorption edge of SiO_2 ", *Phys. Rev. B*, Vol. 22, No. 6, p. 3021 (1980).
 (19) N. F. Mott and E. A. Davis, in *Electronic Processes in Non-Crystalline Materials*, 2nd ed., Clarendon, Oxford, p. 289 (1979).

TWO INHERENT PHOTOLUMINESCENCE BANDS IN HAFNIA AND ZIRCONIA

Toshihide Ito¹, Motohiro Maeda¹, Kazuhiko Nakamura¹,
Masayuki Takase¹, Hiromitsu Kato^{1,2}, and Yoshimichi Ohki¹

¹Waseda University, Shinjuku-ku, Tokyo 169-8555, Japan

²AIST, Tsukuba-shi, Ibaraki 305-8565, Japan

Photoluminescence (PL) spectra induced by ultraviolet photons were measured for many kinds of hafnia, zirconia, hafnium silicate, and zirconium silicate samples. A PL peak was observed around 2.8 eV similarly in all the samples, irrespective of the difference in content of hafnium or zirconium, crystallinity, oxygen deficiency, source alkoxide, deposition method, or the substrate material. The decay profile of this PL is also similar in all the samples. These facts clearly show that neither impurities, oxygen vacancy, nor defects at the interface between the sample and the substrate are responsible for the PL. It is a luminescence inherent in each material, and is most likely due to radiative recombination between localized states at the band tails. When hafnia or zirconia was annealed in oxygen, a new PL peak appeared around 4.2 eV in all the amorphous samples. Vacuum ultraviolet absorption measurements and PL excitation measurements indicate that the 4.2-eV PL is excited due to the inter-band absorption.

1. INTRODUCTION

It is commonly recognized that the thickness of the silicon dioxide or silica as a gate dielectric for complementary metal oxide semiconductor devices will be scaled down in near future to a value below its thinnest limit, where the direct tunneling dominates the leakage current [1]. Therefore, materials with higher permittivities are required in order to maintain a proper thickness of the gate dielectric [2]. The candidates are oxides, silicates, and aluminates such as hafnia [3,4], zirconia [4,5], alumina [6], hafnium silicate [7,8], zirconium silicate [7,8], hafnium silicon oxynitride [9], and hafnium aluminate [10]. However, there is a high possibility that a lot of localized states due to defects are present in the band gap of these materials [11]. These localized states are assumed to cause leakage current [12].

We have shown that photoluminescence (PL) is a very effective method to examine the localized states present in insulating materials [13,14]. In the present research, we apply the PL method to a series of hafnia and hafnium silicate samples with different hafnium contents that were synthesized with various methods, and to a similar series of zirconia and zirconium silicate samples.

2. EXPERIMENTAL PROCEDURES

The samples examined are hafnia (HCA, HCB, and HP), hafnium silicate (H81, H55, H37, and H12), zirconia (ZCA, ZCB, and ZY), and zirconium silicate (Z64, Z51, Z31, and Z06) as listed in Table I. The samples HCA and HCB were deposited by plasma-enhanced chemical vapor deposition (PECVD) using $\text{Hf}(\text{O}-t\text{-C}_4\text{H}_9)_4$ and $\text{Hf}(\text{O}-i\text{-C}_3\text{H}_7)_4$ respectively as source hafnium alkoxides, while ZCA and ZCB were deposited similarly by PECVD using $\text{Zr}(\text{O}-t\text{-C}_4\text{H}_9)_4$ and $\text{Zr}(\text{O}-i\text{-C}_3\text{H}_7)(\text{C}_{11}\text{H}_{19}\text{O}_2)_3$ respectively. All the hafnium or zirconium silicates were deposited by PECVD using tetraethoxysilane [TEOS: $\text{Si}(\text{OC}_2\text{H}_5)_4$] and $\text{Hf}(\text{O}-t\text{-C}_4\text{H}_9)_4$ or $\text{Zr}(\text{O}-t\text{-C}_4\text{H}_9)_4$. Oxygen, used as an oxidation gas, was excited with a RF power of 13.56 MHz through capacitive coupling. For HCA, ZCA, and hafnium or zirconium silicates, the alkoxide was vaporized and transported into the oxygen plasma by controlling its flow rate with a mass-flow controller. In about 20 min, an amorphous film about 100 nm thick was deposited on a substrate when the substrate temperature was kept constant at 500 °C. The substrate used was a *p*-type Si monocrystal wafer, unless otherwise stated. For HCB and ZCB, the alkoxide was vaporized and transported into the oxygen plasma using argon as a carrier and diluent gas. In about 40 min, an amorphous 100-nm thick

Table I. Samples examined with their elemental compositions and thicknesses.

Sample	Elemental ratio (atomic %)			$\text{Hf}_x\text{Si}_{(1-x)}\text{O}_y$		Thickness (nm)
	Hf	Si	O	x	y	
HCA	42	---	58	1.0	1.4	88
HCB	41	---	59	1.0	1.4	130
HP	48	---	52	1.0	1.1	1.1×10^3
H81	31	7.2	62	0.81	1.6	123
H55	20	16	64	0.55	1.8	115
H37	12	21	67	0.37	2.0	96
H12	3.6	27	69	0.12	2.3	72

Sample	Elemental ratio (atomic %)			$\text{Zr}_x\text{Si}_{(1-x)}\text{O}_y$		Thickness (nm)
	Zr	Si	O	x	y	
ZCA	35	---	65	1.0	1.8	130
ZCB	32	---	68	1.0	2.1	98
Z64	22	12	66	0.64	1.9	104
Z51	17	16	67	0.51	2.0	106
Z31	9.9	22	68	0.31	2.1	105
Z06	1.9	29	69	0.06	2.2	144

Sample	Elemental ratio (atomic %)			$\text{Zr}_x\text{Y}_{(1-x)}\text{O}_y$		Thickness (nm)
	Zr	Y	O	x	y	
ZY	30	7.5	63	0.8	1.7	4.5×10^5

film was deposited on the substrate at 400 °C.

The sample HP was deposited on a SiO₂ substrate at 200 °C with a pulse laser deposition (PLD) method by irradiating KrF excimer laser photons onto a hafnia target. The deposited film is amorphous with a thickness of about 1.1 μm. The sample ZY is an yttria-stabilized zirconia (100) crystal plate, about 0.45 mm thick with both sides polished, and was synthesized by Nakazumi Crystal Laboratory.

Using synchrotron radiation (SR) or an ArF excimer laser (photon energy: 6.4 eV) as a photon source, PL, PL excitation (PLE), vacuum ultraviolet (VUV) absorption spectra, and PL decay profiles were measured. These PL characteristics were also obtained for the samples post-annealed at various temperatures for 10 - 20 min in a rapid thermal annealing apparatus filled with oxygen gas at a pressure of $\sim 1.0 \times 10^5$ Pa.

In order to study the elemental composition, the samples were examined by x-ray photoelectron spectroscopy (XPS; JEOL JPS-9010TR or JEOL JPS-90MX) using Mg K α ($h\nu = 1253.6$ eV) x-rays.

3. RESULTS AND DISCUSSION

Figure 1 shows the PL spectra induced in hafnia by the irradiation of SR photons at 6.0 eV and those induced in hafnium silicate by 8.0-eV SR photons. The measured intensity of a PL peak

generally depends on various hardly controllable factors such as a subtle difference in the mutual angles among the photon source, the sample, and the detector. This sometimes makes it difficult to compare the PL intensities among different samples. Therefore, in Fig. 1 and subsequent figures, the PL intensity is shown after being normalized by the highest peak height.

Figure 1 shows that three kinds of hafnia

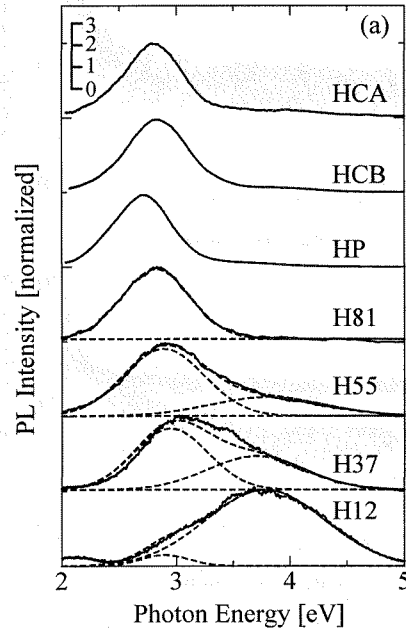


Fig. 1. PL spectra induced by 6.0-eV photons in hafnia and those induced by 8.0-eV photons in hafnium silicate.

samples and four kinds of hafnium silicate samples have an apparently single PL peak. Quite a similar PL profile was obtained for the zirconia and zirconium silicate samples as shown in Fig. 2. In common with Figs. 2 and 3, the top three curves, namely the PL spectra of hafnia or zirconia samples, have a single peak around 2.8 eV. Furthermore, it becomes clear by fitting Gaussian curves to the PL spectrum that the spectrum of each silicate is composed of two component peaks.

The band gap energy of the hafnium or zirconium silicate becomes smaller as the hafnium or zirconium content (x) becomes higher [15]. However, the peak energies of the two component PLs are nearly independent of x as shown in Fig. 3. Although the data are not shown here, the decay profile of the low-energy component PL is almost the same as that of the PL around 2.8 eV in hafnia and zirconia. These results indicate that it is highly probable that the low-energy component PL in the silicates is essentially the same as the 2.8-eV PL in hafnia or zirconia. Therefore, the 2.8-eV PL together with the low-energy component PL is called PL β_H for the hafnia and hafnium silicates and is called PL β_Z for the zirconia and zirconium silicates. The PL component at the higher energy seen in the hafnium silicates is called PL γ_{HS} , and a similar one seen in the zirconium silicates is called PL γ_{ZS} . Since the characteristics of PLs γ_{HS} and γ_{ZS} have been discussed elsewhere [16], the present paper deals mainly with PLs β_H and β_Z that appear in hafnia

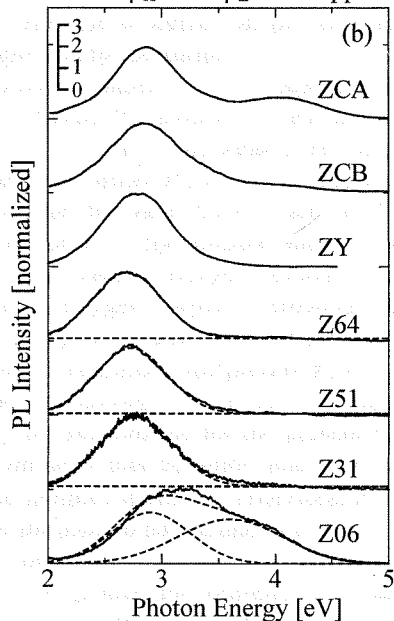


Fig. 2. PL spectra induced by 6.4-eV photons in zirconia and those induced by 8.0-eV photons in zirconium silicate.

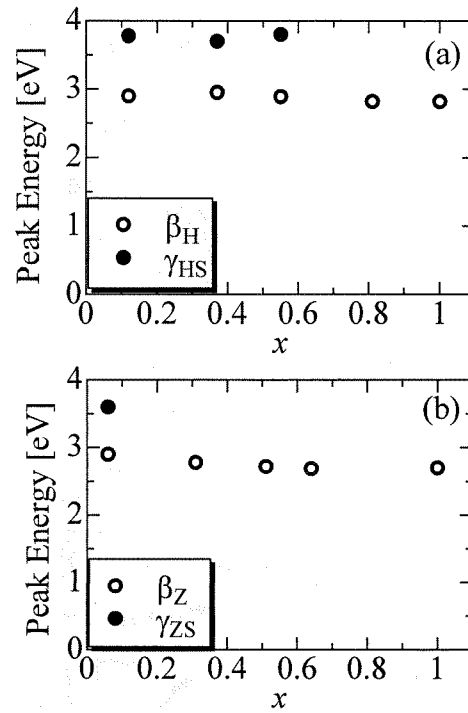


Fig. 3. Changes in PL peak energy as a function of hafnium or zirconium content, observed in $\text{Hf}_x\text{Si}_{(1-x)}\text{O}_y$ (a) and $\text{Zr}_x\text{Si}_{(1-x)}\text{O}_y$ (b).

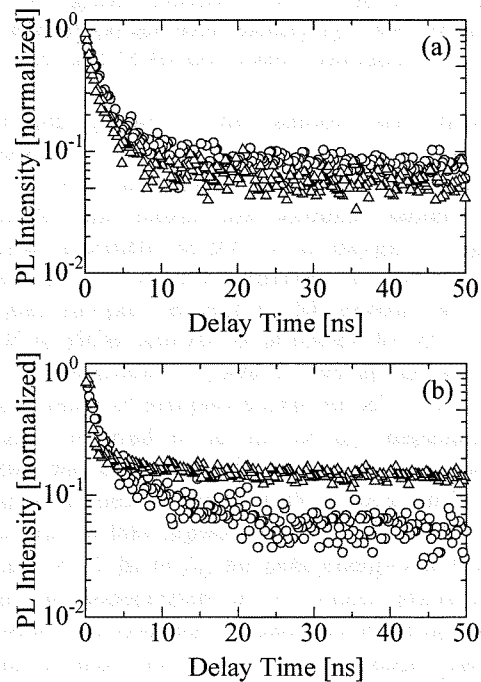


Fig. 4. Decay profiles of PL β_H observed in HCA (circles) and HP (triangles) (a) and those of PL β_Z observed in ZCA (circles) and ZY (triangles) (b).

and zirconia. For this purpose, we have prepared the hafnia and zirconia samples with a wide variation in many respects; amorphous and crystalline, thin and thick, oxygen surplus and deficient, and different synthesizing methods as shown in Table 1.

Figure 4 shows the decay profiles of PLs β_H and β_Z observed in all the hafnia or zirconia samples except for HCB and ZCB. Note that HCB and ZCB were deposited using our old CVD apparatus that was replaced by our new one for HCA and ZCA before the measurements of the PL decay characteristics. The PL decay curve consists of a fast component with a lifetime less than 2 ns and a slow one with a lifetime longer than 50 ns for all the samples. Although the ratio between the fast and slow components differs slightly among the samples, this small difference is considered to be negligible, since there could be many nonessential extraneous factors that affect the ratio. Therefore, it is indicated that the PL decay profile is independent of the difference in source alkoxide or deposition method in both cases of PLs β_H and β_Z . This indicates that the PLs β_H and β_Z are inherent PL bands in hafnia and zirconia. Furthermore, the good similarity between the two PLs β_H and β_Z indicates that their luminescence mechanisms are similar or basically identical. Moreover, similar experiments were repeated for the samples HCA, HCB, ZCA, and ZCB using CaF_2 crystal plates as substrates, and exactly the same PL β_H or β_Z appeared as in the cases of the Si substrates. This strongly indicates that PLs β_H and β_Z are certainly not due to defects at the interface between the sample and the substrate.

Previous papers [17-20] reported the appearance of a broad PL around 2.7 eV and a small PL around 2.0 eV in yttria-stabilized zirconia, and attributed the former PL to yttria-associated oxygen vacancies and the latter to Pr^{3+} and Tb^{3+} [20]. As shown in Table I, the present hafnia and zirconia samples have various oxygen contents, from oxygen deficient to oxygen surplus. However, this difference in oxygen content is not reflected in the PL properties. Therefore, the present PLs β_H and β_Z are not due to oxygen vacancies. Impurities are certainly not responsible for the present PLs, since it is very unlikely that common impurities are present in all the samples studied. Therefore, PLs β_H and β_Z are truly intrinsic to hafnia and zirconia.

If we observe the PL spectra shown in Fig. 2 carefully, we notice the presence of a small hump around 4.2 eV on the PL spectrum of the sample ZCA. The presence of this hump is not limited to ZCA, and

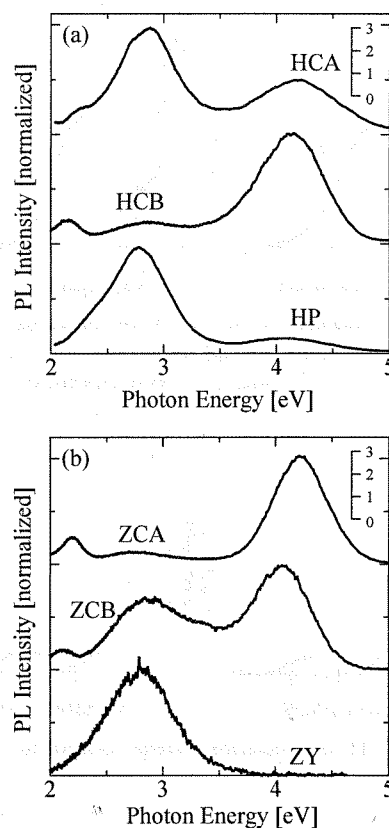


Fig. 5. PL spectra induced by 6.0-eV photons in HCA, HCB, and HP (a) and those induced by 6.4-eV photons in ZCA, ZCB, and ZY (b) after thermal annealing.

its height grows if the sample was thermally annealed.

In order to examine this new PL band more in detail, all the hafnia and zirconia samples were annealed thermally at 900 °C in oxygen. Figure 5 shows the PL spectra observed in the thermally annealed samples, excited by SR photons at 6.0 eV for HCA, HCB, and HP, or at 6.4 eV for ZCA, ZCB, and ZY. A similar PL peak is seen around 4.2 eV in the five kinds of samples except for ZY. This PL is hereafter referred to as α_H or α_Z , depending on whether the sample is hafnia or zirconia. Note that the apparent peak around 2.1 eV is not a real PL peak but a stray or fake replica of the 4.2-eV peak. As in the case of PL β_H or β_Z , the peak energy and shape of PL α_H are independent of the source alkoxide, the deposition method, and the substrate material, and are similar to those of PL α_Z . These results certainly give clues to a study on the PL mechanism. Note that similar results such as the appearance of PL around 4.2 eV in hafnia by a heat treatment were

observed by cathodoluminescence [21].

In order to further obtain information about the excitation of respective PLs, their PLE spectra were measured. Here, the samples used for PLs α_H and α_Z had been thermally treated. Figure 6 (a) shows a typical PLE spectrum for PL β_H monitored at 2.8 eV and the one for PL α_H monitored at 4.4 eV, observed in HCA. The PLE spectrum for PL β_H has two components; the one showing the maximum around 5.1 eV and the other showing a steep rise around 5.7 eV. The location of the latter component is similar to the location of the onset of the PLE spectrum for PL α_H . This indicates that PL β_H has two PL origins; one is in common with PL α_H and the other is different. Similar PLE spectra were observed in the samples HCB and HP. Furthermore, the PLE spectra for PLs β_Z and α_Z observed in ZCA are shown in Fig. 6 (b). Similar PLE spectra were obtained in ZCB. Note that PL α_Z does not appear in ZY even after the heat treatment.

The VUV absorption spectra were also measured. Here, Si substrates of the samples HCA, HCB, ZCA, and ZCB were replaced by CaF_2 substrates, since Si is opaque to VUV photons. As typical examples, the VUV absorption spectra obtained in HCA and ZCA are shown in Fig. 7. In common with the five samples other than ZY, the onset portion of the inter-band photon absorption between the valence band and the conduction band is not a steep curve. It spreads out over a wide energy range, which indicates that these five deposited film samples have much structural randomness. For ZY, only the initial portion of the absorption onset was measurable due to its too thick thickness. However, the onset is located at an energy far lower than the band gap energy of 4.9 eV [20]. This indicates that ZY also has a structural disorder. In such a material, presence of two kinds of threshold energies is generally assumed. One is the band gap energy due to inter-band photon absorption, which is hereafter referred to as E_{opt} . The other is due to photon absorption between tail states below the conduction band and those above the valence band, which is referred to as E_{tail} . For the five amorphous samples other than ZY, the photon absorption can be expressed by the following equation [22] :

$$\alpha h\nu \propto (h\nu - E_g)^2, \quad \text{----- (1)}$$

where α , $h\nu$, and E_g are the absorption coefficient, photon energy, and band gap energy, respectively. Assuming that both E_{opt} and E_{tail} can be estimated by Eq. (1) by substituting E_{opt} or E_{tail} for E_g , the two values are estimated as shown in Fig. 8 (a). Here, in

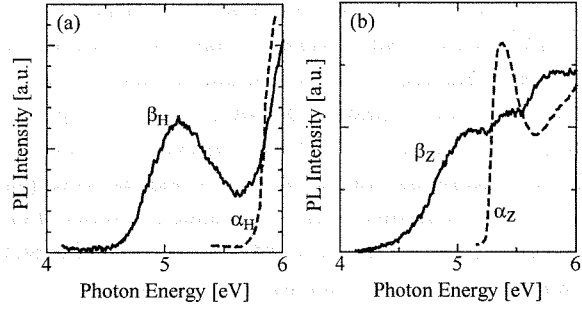


Fig. 6. PLE spectrum for PL α_H or α_Z detected at 4.4 eV (broken curve) and that for PL β_H or β_Z detected at 2.8 eV (solid curve), observed in HCA (a) and ZCA (b).

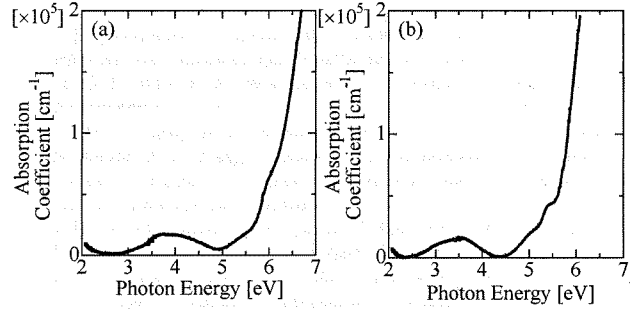


Fig. 7. VUV absorption spectra measured for HCA (a) and ZCA (b).

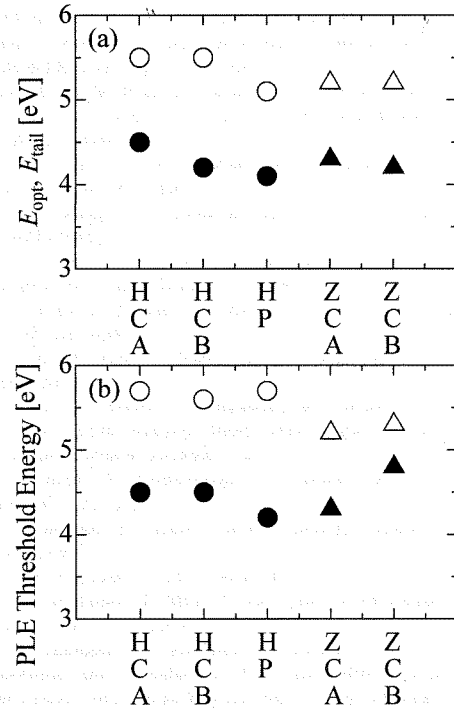


Fig. 8. (a) E_{opt} (open circles and triangles) and E_{tail} (solid circles and triangles). (b) PLE threshold energies E_α (open circles and triangles) and E_β (solid circles and triangles) of PL α_H , α_Z , β_H , or β_Z .

replotting the absorption curves in accordance with Eq. (1), the initial onset portion and the next rising portion were used to estimate E_{tail} and E_{opt} , respectively. Furthermore, by assuming that a similar relationship holds between the threshold energy of PLE and the PLE spectrum, the threshold energies E_{α} for PLs α_{H} and α_{Z} and E_{β} for PLs β_{H} and β_{Z} are estimated as shown in Fig. 8 (b).

From Fig. 8, the threshold energy E_{α} is quite similar to E_{opt} for all the samples, while E_{β} is similar to E_{tail} . This indicates that PLs α_{H} and α_{Z} are excited due to the inter-band absorption and that PLs β_{H} and β_{Z} are excited by photon absorption due to excitation of electrons to localized states located at the tail of the conduction band. As for the PL β_{Z} observed in ZY, the same process can be assumed since the sample also has localized states as mentioned above, although E_{tail} and E_{opt} were not measurable. Furthermore, the thermal treatment increases the intensities of PLs α_{H} and α_{Z} as above-mentioned. It seems that some structural change induced by the thermal treatment opens a path to the upper states of PLs α_{H} and α_{Z} . Another possibility is that the thermal treatment extinguishes localized states that quench PLs α_{H} and α_{Z} , although the details are unknown. Crystal zirconia is reported to have an indirect band gap according to a quantum chemical calculation [23]. This explains the reason that PL α_{Z} does not appear in ZY which is an only crystal among the samples tested.

Although the details have to be omitted because of limitations of space, the above-mentioned characteristics of PLs β_{H} and β_{Z} were similarly observed in all the samples listed in Table I.

4. CONCLUSION

We investigated PL characteristics induced by ultraviolet photons for hafnia, zirconia, hafnium silicate, and zirconium silicate samples having a wide variation in many aspects such as the synthesizing condition. A PL peak was observed around 2.8 eV in common with all the samples. Namely, very similar phenomena are observed irrespective of the difference in hafnium (or zirconium) content, oxygen content, and crystallinity of the sample, source alkoxide, deposition method, or the substrate material. This indicates that the PL is not due to impurities or defects at the interface between the sample and the substrate. The oxygen vacancy is also unlikely to

be responsible. Therefore, this PL is considered to be intrinsic to each material, most likely due to radiative recombination between localized states at the band tails. After the sample was thermally annealed in oxygen at 900 °C, a new PL peak appeared around 4.2 eV in all the amorphous hafnia and zirconia samples. By comparing the PLE spectra of the 4.2-eV PL with the VUV spectra, this PL is considered to be excited due to the inter-band absorption.

5. REFERENCES

- [1] International Technology Roadmap for Semiconductors, International Sematech <http://public.itrs.net/> (2002).
- [2] G. D. Wilk, R. M. Wallace, and J. M. Anthony, *J. Appl. Phys.* **89**, 5243 (2001).
- [3] H. H. Tseng, M. E. Ramon, L. Hebert, P. J. Tobin, D. Triyoso, J. M. Grant, Z. X. Jiang, D. Roan, S. B. Samavedam, D. C. Gilmer, S. Kalpat, C. Hobbs, W. J. Taylor, O. Adetutu, and B. E. White, *Tech. Dig. Int. Electron Devices Meet.*, 83 (2003).
- [4] D. A. Neumayer and E. Cartier, *J. Appl. Phys.* **90**, 1801 (2001).
- [5] J. P. Chang and Y. S. Lin, *J. Appl. Phys.* **90**, 2964 (2001).
- [6] Y. I. Ogita, S. Iehara, T. Tomita, *Thin Solid Films*, 161 (2003).
- [7] H. Kato, T. Nango, T. Miyagawa, T. Katagiri, K. S. Seol, and Y. Ohki, *J. Appl. Phys.* **92**, 1106 (2002).
- [8] G. D. Wilk, R. M. Wallace, and J. M. Anthony, *J. Appl. Phys.* **87**, 484 (2000).
- [9] M. Koike, T. Iño, Y. Kamimuta, M. Koyama, Y. Kamata, M. Suzuki, Y. Mitani, A. Nishiyama, and Y. Tsunashima, *Tech. Dig. Int. Electron Devices Meet.*, 107 (2003).
- [10] H. Y. Yu, M. F. Li, B. J. Cho, C. C. Yeo, M. S. Joo, D. L. Kwong, J. S. Pan, C. H. Ang, J. Z. Zheng, and S. Ramanathan, *Appl. Phys. Lett.* **81**, 376 (2002).
- [11] W. J. Zhu, T. P. Ma, S. Zafar, and T. Tamagawa, *IEEE Electron Device Lett.* **23**, 597 (2002).
- [12] A. Y. Kang, P. M. Lenahan, and J. F. Conley, *Appl. Phys. Lett.* **83**, 3407 (2003).
- [13] K. S. Seol, T. Watanabe, M. Fujimaki, H. Kato, Y. Ohki, and M. Takiyama, *Phys. Rev. B* **62**, 1532 (2000).
- [14] H. Kato, N. Kashio, Y. Ohki, K. S. Seol, and T. Noma, *J. Appl. Phys.* **93**, 239 (2003).
- [15] T. Ito, H. Kato, T. Nango, and Y. Ohki, *Jpn. J. Appl. Phys.*, to appear (2004).
- [16] T. Ito, M. Maeda, K. Nakamura, M. Takase, Y. Ohki, H. Kato, *Ext. Abstr. 65th Autumn Meet. 2004, Japan Society of Applied Physics and Related Societies*, 1a-C-10.
- [17] M. Kunz, H. Kretschmann, W. Assmus, and C. Klingshirn, *J. Lumin.* **37**, 123 (1987).
- [18] P. Camagni, P. Galinetto, and G. Samoggia, *Solid State Commun.* **83**, 943 (1992).
- [19] S. E. Paje and J. Llopis, *Appl. Phys. A* **57**, 225 (1993).
- [20] H. Nakajima, T. Mori, S. Itoh, and M. Watanabe, *Solid State Commun.* **129**, 421 (2004).
- [21] S. Yamasaki, N. Mizuochi, T. Yasuda, J. Isoya, S. Sakai, M. Kadoshima, and T. Nabatame, *Ext. Abstr. 49th Spring Meet. 2002, Japan Society of Applied Physics and Related Societies*, 28p-A-13.
- [22] N. F. Mott and E. A. Davis, in *Electronic Processes in Non-Crystalline Materials*, 2nd ed. (Clarendon, Oxford, 1979), p. 289.
- [23] B. Kralik, E. K. Chang, and S. G. Louie, *Phys. Rev. B* **57**, 7027 (1998).

Temperature effects on luminescence properties of Cr³⁺ ions in alkali gallium silicate nanostructured media

Kristina E. Lipinska-Kalita^{a)}

Department of Physics, High Pressure Science and Engineering Center, University of Nevada Las Vegas, Las Vegas, Nevada 89154-4002

Denise M. Krol

Department of Applied Science, University of California Davis, Davis, California 95615

Russell J. Hemley

Geophysical Laboratory, Carnegie Institution of Washington, Washington D.C. 20015

Patricia E. Kalita and Cedric L. Gobin

Department of Physics, University of Nevada Las Vegas, Las Vegas, Nevada 89154-4002

Yoshimichi Ohki

Department of Electrical Engineering and Bioscience, Waseda University, Tokyo 169-8555, Japan

(Received 10 January 2005; accepted 13 July 2005)

We have investigated the optical properties of Cr³⁺ ions in an alkali gallium silicate glass system and in two glass-based nanocomposites with nucleated β -Ga₂O₃ nanocrystals. The nucleation and growth of the nanocrystalline phase in the host glass matrix were monitored by Raman-scattering spectroscopy and angle-dispersive x-ray-diffraction. A broadband luminescence, associated with the ⁴T₂-⁴A₂ transition from the weak crystal field of octahedral Cr³⁺ sites, dominated the emission of the precursor as-quenched glass. The luminescence spectra of the synthesized glass-ceramic nanocomposites revealed a crystal-like ²E-⁴A₂ strong emission and indicated that the major fraction of Cr³⁺ ions was located within the nanocrystalline environment. The variable-temperature studies of the nanocomposites demonstrated that the fluorescence of Cr³⁺ ions can be transformed from sharp R lines of the ²E-⁴A₂ transition to a combination of R lines and of the broad band of the ⁴T₂-²A transition. We propose a simple distribution model where the major part of Cr³⁺ ions is located in the nanocrystalline phase of the glass-ceramic composites in the octahedral environment, substituting the gallium atoms in the β -Ga₂O₃ crystal structure. The developed nanocrystalline glass-ceramics are a promising class of Cr³⁺-doped oxide glass-based optically active composite materials. © 2005 American Institute of Physics. [DOI: 10.1063/1.2012509]

I. INTRODUCTION

A key trend in solid-state physics is the research of heterophased composite materials with nanometer-size structures of metal, semiconductor, or dielectric clusters dispersed in diverse solid matrices. Nanocomposites currently attract much research attention because of their multiple technological applications.¹⁻⁹ From the viewpoint of optical properties, transparent glass-ceramics with nanosized crystals or quantum dots embedded in glass matrices have been extensively investigated because of their potential function as promising media for optical devices.^{1-3,7} Especially, silica glass-based composites doped with a selected range of optically active ions are of particular research interest. Chromium-based luminescent solids continue to be of technological interest, since the octahedrally coordinated Cr³⁺ ions can function as laser-active centers and can also act as energy sensitizers in rare-earth-based laser materials.¹⁰⁻¹⁴ For application in the field of solid-state lasers or optical amplifiers it is essential to know correctly the environment where the optically active

ions are located. In fact the spectral characteristics of the luminescent ions, specifically in the case of transition metals, are strongly dependent on the nature of their local environment.¹⁵⁻²⁴

In our former studies, we investigated the nucleation and crystallization processes in a range of multicomponent glass systems. The endeavor was to design and synthesize optically transparent glass-ceramic nanocomposites displaying optical properties, in particular, an increased optical gain.⁷⁻⁹ In this paper we present the results of spectroscopic investigations of Cr³⁺ ions dispersed in an alkali gallium silicate glass system and in two glass-ceramic nanocomposites with different diameters of nanocrystalline β -Ga₂O₃ phase dispersed in the glass matrix. Considered from the standpoint of optical properties, these composites are very attractive for studying how a change of local environment, caused by the nucleation of nanocrystals, modifies the material's luminescence properties. In particular, we focus on luminescence as a function of temperature and we compare the emission from Cr³⁺ ions in the as-quenched precursor glass with that in two synthesized glass-ceramic nanocomposites. We also attempt to elucidate the question of whether the Cr³⁺ ions infiltrate

^{a)} Author to whom correspondence should be addressed; FAX: 702 895 0804; electronic mail: kristina@physics.unlv.edu

the nanocrystalline phase and if so, how are they localized in the structure, and finally, we propose a model explaining the local environment of the Cr^{3+} ions.

II. EXPERIMENT

A mixture for the alkali gallium silicate precursor glass, of nominal composition represented by 2 Na:2 K:8 Ga:24 Si:64 O ratio in at. %, doped with 0.03-wt % Cr_2O_3 was prepared using analytical grade reagents of 99.999% purity. The batch components were sintered at low temperature and afterwards melted in a platinum crucible at a temperature of 1550 °C in a resistance furnace in an air atmosphere. The liquid melt was cast into a brass mold and air cooled. To induce nucleation of $\beta\text{-Ga}_2\text{O}_3$ phase in the as-quenched host glass matrix, rectangular pieces of material underwent isothermal heat treatments at temperatures close to the glass crystallization, which was about 880 °C as estimated from differential thermal studies. Following this procedure a series of glass-ceramic nanocomposites were obtained and two of them were selected for spectroscopic investigations. The rate of the temperature increase varied from 1.0 up to 200 °C/min, 0.5 up to 500 °C/min, and 0.2 °C/min up to the setup temperature which was 850 °C (10 h) for composite 1 and 900 °C (6 h) for composite 2. To confirm the amorphous nature of the as-quenched precursor glass, as well as to identify the structure and estimate the average diameter of the nanocrystalline phase in the synthesized glass-ceramic composites we used a conventional x-ray-diffraction technique and Raman-scattering spectroscopy. The temperature-dependent luminescence spectra were excited with the 442-nm line of a krypton laser, analyzed with a single-grating monochromator, and detected with a photomultiplier operating in photon-counting mode. For low-temperature experiments, the samples were mounted in a closed-cycle helium continuous-flow cryostat (Oxford Instruments), whose temperature was controlled to within 1 K. The luminescence spectra were collected in the temperature range from 10 up to 170 K and 220 K for composite 1 and composite 2, respectively.

III. RESULTS AND DISCUSSION

A. Microstructural studies

Both the x-ray-diffraction technique and the Raman-scattering spectroscopy confirmed the amorphous nature of the as-quenched glass. The angle-dispersive x-ray-diffraction patterns of the as-quenched glass and of the two synthesized glass-ceramic nanocomposites are presented in Fig. 1. A distinct change in the glass microstructure occurred after thermal annealing and nucleation of the monoclinic $\beta\text{-Ga}_2\text{O}_3$ phase was detected. The diffraction spectrum of the as-quenched glass shown in Fig. 1(a), exhibits broad bands in the low- 2θ range, typical of glass systems. However, diffraction patterns of both glass-ceramic nanocomposites (Fig. 1, plots b and c) show sharp $\beta\text{-Ga}_2\text{O}_3$ peaks overlapped with a broad glass continuum. The estimated diameter of the nanocrystalline phase (using the Scherrer equation) was 14.5 ± 1.6 and 18.2 ± 2.1 nm for composites 1 and 2, respectively. The details of the crystal size and size distribution calculations

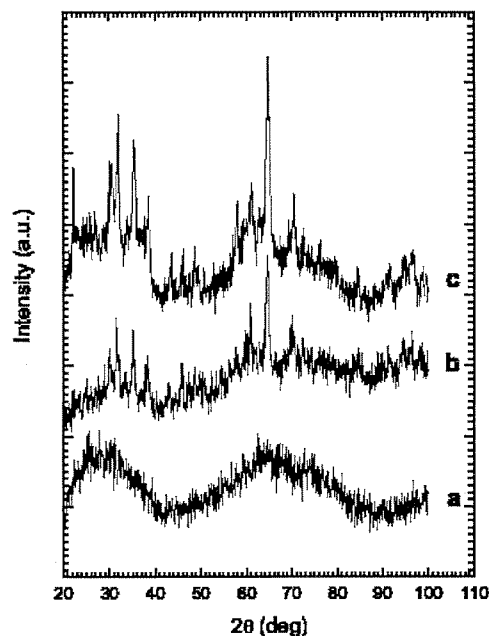


FIG. 1. Angle-dispersive x-ray-diffraction patterns of as-quenched glass (plot a) and of the two synthesized glass-ceramics: composite 1 (plot b) and composite 2 (plot c). The sharp peaks in composite 1 and in composite 2 correspond to gallium oxide nanocrystals. The estimated mean crystallite diameter (the Scherrer equation) is 14.5 ± 1.6 nm for composite 1 and 18.2 ± 2.1 nm for composite 2.

were presented previously.⁸ The presence of the monoclinic $\beta\text{-Ga}_2\text{O}_3$ phase in the nanocomposites was also confirmed by Raman-scattering spectroscopy. Figure 2 illustrates VV- (plot A) and HV- (plot B) polarized Raman-scattering spectra of the as-quenched glass, the two glass-ceramic nanocomposites, and a $\beta\text{-Ga}_2\text{O}_3$ reference crystal. The sharp, small-intensity peaks, which overlap with the broad Raman-scattering bands characteristic of silica glass, indicate the nucleation of gallium oxide nanocrystals in the matrix of the host glass.

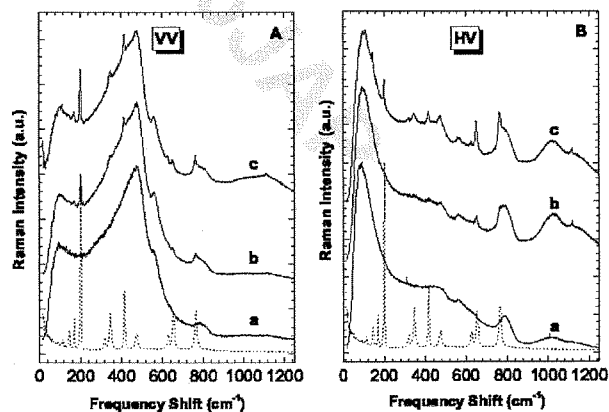


FIG. 2. VV (part A) and HV (part B) polarized Raman-scattering spectra of as-quenched glass (plots a) and two glass-ceramic nanocomposites: composite 1 (plots b) and composite 2 (plots c). The sharp, small-intensity peaks overlapped with the Raman glass bands indicate the nucleation of gallium oxide nanocrystals. The Raman spectrum of a $\beta\text{-Ga}_2\text{O}_3$ reference powder is shown as a dotted line.

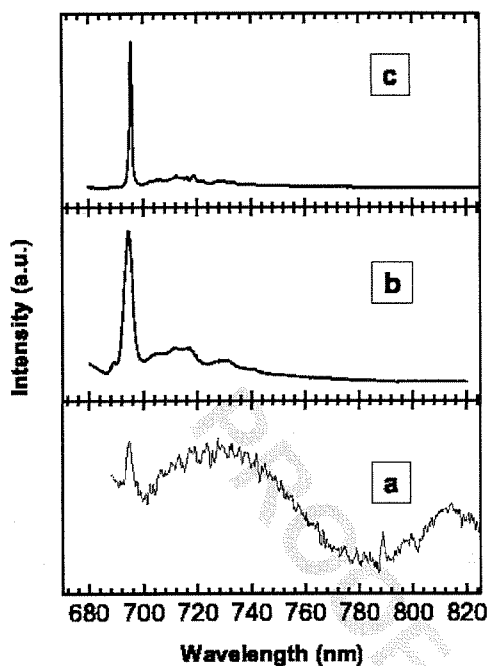


FIG. 3. Luminescence spectra measured at 10 K of the as-quenched precursor glass (plot *a*) and of the synthesized glass-ceramic nanocomposites: annealed at 850 °C composite 1 (plot *b*) and annealed at 900 °C composite 2 (plot *c*). The very strong intensity of the *R* lines of Cr^{3+} emission characterizes the emission spectra of the two composites.

B. Luminescence properties of the as-quenched glass and the glass-ceramic nanocomposites: A comparison

Chromium ions dispersed in inorganic solid host matrices occupy preferentially octahedral symmetry sites due to the strong ligand-field stabilization energy in sixfold coordination.¹⁵⁻¹⁸ The octahedral energy-level structure is determined by the relative strength of the crystal field and the two lowest-excited levels in the energy-level diagram of the Cr^{3+} ion are 2E and 4T_2 . In a weak crystal field, the 4T_2 state is at a lower energy than the 2E state and Cr^{3+} exhibits a broad luminescence band related to the strongly coupled lattice transition from the 4T_2 to the ground 4A_2 level. Since optical transitions from the 4T_2 state to the ground 4A_2 state are spin-allowed, the radiative decay time is very short (on the order of tens of microseconds). In an intermediate crystal field, the broad 4T_2 - 4A_2 band and the sharper 2E - 4A_2 transition, weakly coupled to the lattice, are both superimposed. In a strong crystal field the first excited state of the Cr^{3+} ions is the 2E level, weakly coupled to the lattice. The optical transitions from the 2E level to the ground 4A_2 state are characterized by the presence of one or two sharp zero-phonon lines (called *R* lines), with a one-phonon sideband. Since this transition is spin-forbidden the long radiative decay time is usually measured in milliseconds.

The luminescence spectra of the as-quenched glass, precursor material of the synthesized nanocomposites, measured at 10 K are presented in Fig. 3. In a glass, the Cr^{3+} ions experience a wide range of crystal fields and the luminescence from such a system may include mixed emission from

the 2E level of Cr^{3+} ions in the strong crystal field sites as well as from the 4T_2 level of Cr^{3+} ions in a weak crystal field. The dominant feature of the as-quenched glass emission (Fig. 3, plot *a*) is a broad band centered at about 730 nm with a small peak at 695 nm. This electronic-vibrational band exhibits a typical signature of the 4T_2 - 4A_2 emission of Cr^{3+} ions residing in a weak octahedral field, strongly coupled to the lattice vibrations. The weak-intensity peak at 695 nm, overlapped with the 4T_2 - 4A_2 band, is due to the 2E - 4A_2 emission. The strong intensity of the 4T_2 - 4A_2 transition and the weak intensity of the 2E - 4A_2 peak in the 10-K spectrum of the glass (Fig. 3, plot *a*) indicate that only a small fraction of Cr^{3+} ions is located in the strong crystal-field sites, while a majority of Cr^{3+} ions occupy the weak crystal-field sites. After the extended thermal annealing of the precursor glass, which produced nucleation of gallium oxide nanocrystals in the glass matrix, the broad band of the 4T_2 - 4A_2 transition of Cr^{3+} ions in the weak crystal-field sites disappears gradually from the emission spectra (Fig. 3 plots *b* and *c*). This can be explained by the increased amount of nanocrystalline β - Ga_2O_3 phase in the host glass matrix. The glass-ceramic nanocomposites (Fig. 3 plot *b* and *c*) exhibit very intense emission peaks attributed to 2E - 4A_2 transitions of Cr^{3+} ions in a strong octahedral crystal field (*R* lines). The main difference in the luminescence spectra of the two nanocomposites is that the dominant feature, the 2E - 4A_2 emission, exhibits much stronger intensity with particularly narrow bandwidth in composite 2 compared to composite 1. The microstructural characterization (Figs. 1 and 2) and the luminescence spectra (Fig. 3) give ground to conclude that as a result of thermal annealing, which induced the nucleation of nanocrystals in the glass matrix, a significant redistribution of the luminescence intensity occurred. The spectra of both nanocomposites are dominated by very strong emission lines accompanied by much weaker intensity, structured phonon sidebands. Considering the high intensities, the narrow bandwidths, and the energy position of these emissions (Fig. 3 plots *b* and *c*) we assign these lines to the Cr^{3+} ions located in the nanocrystalline environment in intermediate-to-strong octahedral field sites.

C. Low-temperature luminescence studies

Temperature-dependent luminescence studies were performed in order to isolate the spectral contribution from Cr^{3+} ions located in weak crystal-field sites of the glass matrix from those of Cr^{3+} ions located in strong crystal-field sites, that is, embedded in ordered structures like the nanocrystalline phase. Figures 4(a) and 4(b) show the luminescence spectra measured from 10 up to 170 and 220 K for composite 1 and composite 2, respectively. At 10 K, the narrow and very intense peaks at about 695 nm are the dominant features of the emission spectra of the composites. In composite 1 [Fig. 4(a)], with β - Ga_2O_3 nanocrystals of 14.5 ± 1.6 -nm diameter, the 2E - 4A_2 emission region differs noticeably from that of composite 2 [Fig. 4(b)] with nanocrystals of 18.2 ± 2.1 -nm diameter. In particular, the intensity ratio of the *R*-line emissions (2E - 4A_2) to the total luminescence intensity is about 25% higher for composite 2. Moreover, the *R* lines

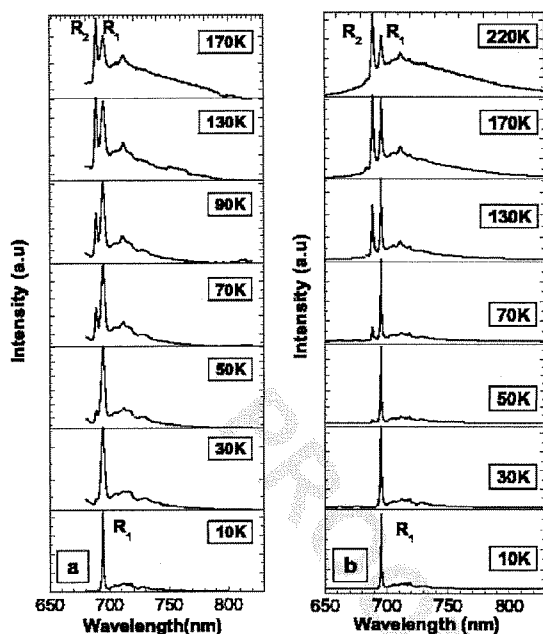


FIG. 4. Temperature dependence of the luminescence for composite 1 (part a) and for composite 2 (part b). The spectra of both composites illustrate the strong ${}^2E-{}^4A_2$ emissions attributed to the zero-phonon R_1 and R_2 lines of Cr^{3+} .

of composite 2 have much narrower bandwidths for the same temperatures with respect to that of composite 1. The emission spectra of the composites [Figs. 4(a) and 4(b)] up to about 70 K are dominated by the R -lines' emission, indicating that the prevailing luminescence contribution comes from the strong crystal-field Cr^{3+} sites with the energy of the 4T_2 levels higher than that of the 2E levels. With further increase in temperature, the spectral changes are reflected by the evolution of the structured R -lines' emissions. Beginning at about 30 K for composite 1 and 50 K for composite 2, a second ${}^2E-{}^4A_2$ emission line (the R_2 line) appears in the spectra. With temperature rise, the intensity of the R_2 lines increases with respect to the R_1 lines and starting from 130 K for composite 1 and 170 K for composite 2, the R_2 lines become dominant [Figs. 4(a) and 4(b)]. Beside a continuing decrease in their intensity with temperature rise, the R lines of both nanocomposites gradually increase their bandwidths. These changes are accompanied by a notable enhancement of luminescence intensity on the low-energy side of the R lines. The 4T_2 emission is almost nonexistent at low temperatures and the luminescence below about 30 K for composite 1 and below about 70 K for composite 2 consists of a dominant R_1 -line emission with the associated phonon sidebands. However, with temperature increase the redistribution of the luminescence intensity from the narrow ${}^2E-{}^4A_2$ lines to the broad Stokes emissions suggests a progressive increase of the thermal populations of the 4T_2 states. When approaching room temperature the energy difference of the 4T_2 and 2E states is sufficiently small to permit a partial thermal population of the 4T_2 states. As a result, above about 50 K, the emission spectra of both composites consist of the two zero-phonon lines (R_1 and R_2 lines) overlapped with the accom-

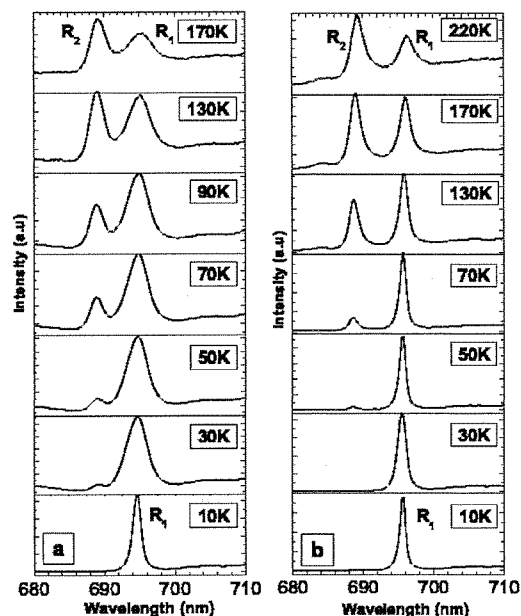


FIG. 5. Expanded-scale temperature dependence of the luminescence intensity in the region of R lines of Cr^{3+} for composite 1 (part a) and for composite 2 (part b).

panying Stokes and small anti-Stokes phonon sidebands, superimposed with increasing emissions from the ${}^4T_2-{}^4A_2$ transition. In conclusion, the variable-temperature studies indicate for both composites two main regimes of behavior: a low-temperature regime where the emission of the zero-phonon lines and their sidebands from the 2E state of Cr^{3+} dominate, and a high-temperature regime with the important contribution of the thermally populated 4T_2 states.

We now consider in greater detail the temperature dependence of the luminescence intensity in the region of R lines for composite 1 and composite 2, respectively, as shown in Figs. 5(a) and 5(b). In the spectral range of the ${}^2E-{}^4A_2$ emission (R lines) both nanocomposites differ not only by the intensity ratios but also by the spectral profiles of the R lines. Homogeneous broadening dominates the line-width of the R -line emissions above 50 K. The shift of the positions of the R lines and their bandwidth modifications as functions of temperature are examined in Figs. 6 and 7, respectively. For both nanocomposites, the R_1 and R_2 lines increase their bandwidths with temperature and move gradually to longer wavelengths (redshift). These shifts are linear

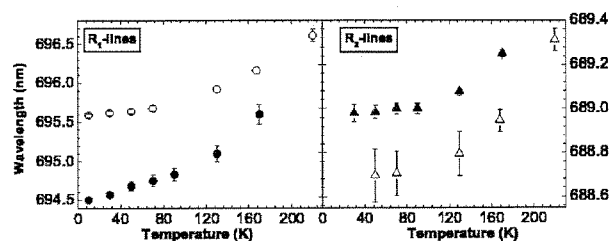


FIG. 6. Low-energy shift of the R_1 and R_2 lines position of the Cr^{3+} emission as a function of temperature for composite 1 (solid circles) and composite 2 (open circles).

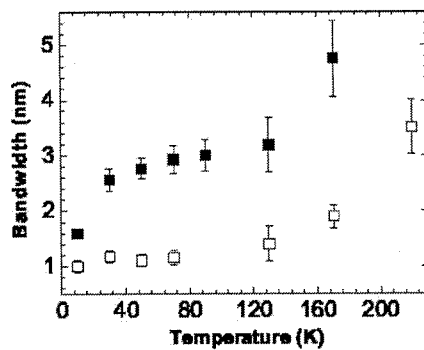


FIG. 7. Temperature dependence of the bandwidth of the R_1 line of the Cr^{3+} emission for composite 1 (solid squares) and composite 2 (open squares).

at low temperature, but as the temperature rises up to about 90 K a crossover from linear to nonlinear (T^2) behavior occurs. Similar results have been previously reported by Rossi *et al.*²⁴ for the cordierite glass-ceramic.

For potential practical applications of the nanostructured glass-ceramic composites, it is essential to know the location of the optically active ions in the material's structure. In fact, especially for the transition-metal ions, the spectral characteristics of their emission are strongly dependent on the local environment.¹⁵⁻²⁴ It is known that Cr^{3+} ions reside preferentially in octahedral rather than in tetrahedral sites because the $3d^3$ electron configuration has its maximum stabilization energy in the octahedral symmetry. In oxide glass matrices Cr^{3+} ions may form CrO_6 octahedral arrangements that satisfy local energy requirements. The situation is more complex in the case of a nanocrystalline glass-ceramic composite. In such a material different structural sites are accessible to the luminescent ions: (i) the sites inside the glass phase, (ii) the sites inside the nanocrystalline phase, and (iii) the sites at the nanocrystal-glass interface. The luminescence spectra of the studied glass-ceramic nanocomposites revealed the noteworthy presence of strong crystal-field Cr^{3+} centers. The crystal-like ${}^2E-{}^4A_2$ (R lines) emission in low temperatures indicated that the major fraction of Cr^{3+} ions is located within the nanocrystalline environment. With the rise of temperature, the increasing contribution of the ${}^4T_2-{}^4T_2$ broad emission is combined with the still present sharp ${}^2E-{}^4A_2$ emission. This may illustrate the presence of an intermediate-to-strong crystal field, where the energy difference between the 2E and the 4T_2 states is small enough to permit a thermal population of the higher of the two states. Based on the presented results we propose a simple distribution model where the major part of the Cr^{3+} ions are located in the nanocrystalline environment, most likely in octahedral symmetry arrangements. Actually, the $\beta\text{-Ga}_2\text{O}_3$ crystal has 50% of Ga atoms in octahedral and 50% in tetrahedral coordination with oxygen atoms.²⁵ Since the octahedral sites are available in the structure of the nanocrystalline phase ($\beta\text{-Ga}_2\text{O}_3$), we can envision a scenario where Cr^{3+} ions substitute gallium ions in those sites. The quadratic temperature behavior of the R -line bandwidth above 100 K compared to the linear dependence observed for different glasses^{21,24} in the same range of temperatures also indicates that at least the major part of the Cr^{3+} ions is located in the nanocrystalline phase.

IV. CONCLUSION

We have studied the optical properties of Cr^{3+} ions in the alkali gallium silicate glass system and in the glass-ceramic nanocomposites with embedded $\beta\text{-Ga}_2\text{O}_3$ nanocrystals. A broadband luminescence associated with the ${}^4T_2-{}^4A_2$ transition from the weak crystal-field, octahedral Cr^{3+} sites dominated the spectrum of the precursor as-quenched glass. The glass-ceramic nanocomposites revealed the crystal-like ${}^2E-{}^4A_2$ emission and demonstrated that the major fraction of Cr^{3+} ions was located within the crystalline environment. The variable-temperature studies of the nanocomposites illustrated that the Cr^{3+} luminescence can be transformed from the sharp R lines of the ${}^2E-{}^4A_2$ emission to a combination of R lines and the broadband of the ${}^4T_2-{}^2A_1$ transition. We postulated that the overall modification of the luminescence profiles from the broad ${}^4T_2-{}^4A_2$ emission for the as-quenched precursor glass to the narrow R lines for glass-ceramic composites reflects the kinetics of the $\text{Ga}_2\text{O}_3:\text{Cr}^{3+}$ nanocrystallite formation and the migration process of Cr^{3+} ions from the glass matrix to the nanocrystalline phase. Based on the presented results we proposed a simple distribution model that provided a reasonable quantitative agreement with the experimental data. In this model we advanced that the major part of Cr^{3+} ions were located in the nanocrystalline phase, most likely in the octahedral environment.

ACKNOWLEDGMENTS

Part of this work was done under financial support of the Advanced Research Institute for Science and Engineering, Waseda University, Tokyo (Japan). The authors acknowledge the Nippon Electric Glass Company, Kyoto (Japan) for technical advice and the use of their facilities for samples preparation. The authors gratefully acknowledge the support from the U.S. Department of Energy Cooperative Agreement No. FC08-01NV14049 with the University of Nevada Las Vegas.

- ¹A. Stepanov, D. E. Hole, and P. D. Townsend, *J. Non-Cryst. Solids* **260**, 65 (1999).
- ²E. Borsella *et al.*, *J. Non-Cryst. Solids* **245**, 122 (1999).
- ³G. DeMarchi, F. Gonella, and P. Mazzoldi, *J. Non-Cryst. Solids* **196**, 79 (1996).
- ⁴Y. Wang and J. Ohwaki, *Appl. Phys. Lett.* **63**, 3268 (1993).
- ⁵P. A. Tick, N. F. Borrelli, L. K. Cornelius, and M. A. Newhouse, *J. Appl. Phys.* **78**, 116367 (1995).
- ⁶M. J. Dejneka, *J. Non-Cryst. Solids* **239**, 149 (1998).
- ⁷F. Auzel, K. E. Lipinska-Kalita, and P. Santa-Cruz, *Opt. Mater.* **5**, 75 (1996).
- ⁸R. Ceccato, R. Dal Maschio, G. Mariotto, M. Montagna, F. Rossi, M. Ferrari, K. E. Lipinska-Kalita, and Y. Ohki, *J. Appl. Phys.* **90**, 2522 (2001).
- ⁹K. E. Lipinska-Kalita, B. Chen, M. Kruger, Y. Ohki, J. Murowchik, and E. P. Gogol, *Phys. Rev. B* **68**, 035209 (2003).
- ¹⁰U. Hommerich and K. L. Bray, *Phys. Rev. B* **51**, 12133 (1995).
- ¹¹M. Yamaga, B. Henderson, K. P. O'Donnell, and Y. Gao, *Phys. Rev. B* **44**, 4853 (1991).
- ¹²B. Henderson, M. Yamaga, Y. Gao, and K. P. O'Donnell, *Phys. Rev. B* **46**, 652 (1992).
- ¹³E. Luria, S. R. Rotman, J. A. Mares, G. Boulon, A. Brenier, and L. Lou, *J. Lumin.* **72-74**, 951 (1997).
- ¹⁴P. Hong, X. X. Zhang, C. W. Struck, and B. Di Bartolo, *J. Appl. Phys.* **78**, 4659 (1995).
- ¹⁵D. L. Russell, K. Holiday, M. Grinberg, and D. B. Hollis, *Phys. Rev. B* **59**, 13712 (1999).
- ¹⁶A. Kaminska, P. Kaczor, A. Durygin, A. Suchocki, and M. Grinberg, *Phys.*

- Rev. B **65**, 104106 (2002).
- ¹⁷A. Kaminska, A. Suchocki, L. Arizmendi, D. Callejo, F. Jaque, and M. Grinberg, Phys. Rev. B **62**, 10802 (2000).
- ¹⁸A. Kaminska, A. Suchocki, M. Grinberg, J. Garcia-Sole, F. Jaque, and L. Arizmendi, J. Lumin. **87-89**, 571 (2000).
- ¹⁹C. Koepke, K. Wisniewski, M. Grinberg, D. L. Russel, K. Z. Holliday, and G. Beall, J. Lumin. **78**, 135 (1998).
- ²⁰■. Hommerich, K. L. Bray, Y. Shen, and K. Bray, Phys. Rev. B **51**, 12133 (1995).
- ²¹S. P. Feofilov, A. A. Kaplyanski, A. B. Kulinkin, R. S. Meltzer, and T. N. Vasilevskaya, J. Lumin. **100**, 155 (2002).
- ²²F. Rossi, M. Montagna, M. Ferrari, J. A. Capobianco, and M. Betinelli, J. Non-Cryst. Solids **240**, 232 (1998).
- ²³M. Grinberg, J. Barzowska, Y. Shen, and K. Bray, Phys. Rev. B **63**, 214104 (2001).
- ²⁴F. Rossi, G. Pucker, M. Montagna, M. Ferrari, and A. Buckenter, Opt. Mater. **13**, 373 (2000); S. Geller, J. Chem. Phys. **33**, 676 (1966).
- ²⁵■.

PROOF COPY 067516JAP

Synthesis and characterization of metal-dielectric composites with copper nanoparticles embedded in a glass matrix: A multitechnique approach

Kristina E. Lipinska-Kalita^{a)}

High Pressure Science and Engineering Center, Department of Physics, University of Nevada Las Vegas, Las Vegas, Nevada 89154-4002

Denise M. Krol

Department of Applied Science, University of California Davis, Livermore, California 94550

Russell J. Hemley

Geophysical Laboratory, Carnegie Institution of Washington, Washington, D.C. 20015

Gino Mariotto

Dipartimento di Fisica, Università di Trento, 38050 Povo (Trento), Italy

Patricia E. Kalita

Department of Physics, University of Nevada Las Vegas, Las Vegas, Nevada 89154-4002

Yoshimichi Ohki

Department of Electrical, Electronics and Computer Engineering, Waseda University, Shinjuku, Tokyo 169-8555, Japan

(Received 15 October 2004; accepted 7 July 2005)

The precipitation and growth of copper nanoparticles in an optically transparent aluminosilicate glass matrix was investigated. The size of particles in this heterophase glass-based composite was modified in a controlled manner by isothermal heat treatments. A multitechnique approach, consisting of Raman-scattering spectroscopy, high-resolution transmission electron microscopy, x-ray-diffraction technique, and optical-absorption spectroscopy, has been used to study the nucleation and crystallization processes. Optical-absorption spectroscopy revealed the presence of intense absorption bands attributed to oscillations of free electrons, known as the surface-plasmon resonance band of copper particles, and confirmed a gradual increase of the particles' mean size and density with annealing time. The Raman scattering on acoustical phonons from Cu quantum dots in the glass matrix measured for off-resonance conditions demonstrated the presence of intense, inhomogeneously broadened peaks that have been assigned to the confined acoustic eigenmodes of copper nanoparticles. The particle-size dependence of the acoustic peak energies and the relation between the size distribution and bandwidths of these peaks were derived. High-resolution transmission electron microscopy was used to monitor the nucleation of the nanoparticles and to estimate their mean size. © 2005 American Institute of Physics. [DOI: 10.1063/1.2011776]

I. INTRODUCTION

Composite materials consisting of nanosized crystals or quantum dots embedded in solid matrices stimulate currently intense research interest. Small metal and semiconductor clusters, dispersed in optically transparent matrices, belong to three-dimensional quantum-confined electronic systems and their properties are affected by the confinement processes in the nanosized particles (electrons, holes, excitons, phonons). It was demonstrated that due to dielectric and quantum confinement effects such composites exhibit largely enhanced nonlinear susceptibilities, fast response time, and are promising candidates for all optical switching devices.¹⁻⁷ In particular, the electron-phonon coupling increases in strength with decreasing nanocrystal diameter and is of key importance in these composites.¹⁻⁷ One crucial requirement with regard to the potential technical applications of these

composite materials in the field of nonlinear optical devices is to have an accurate knowledge of the particle size as well as their size distribution.

Raman-scattering spectroscopy in the very-low-frequency region has proven to be one of the most outstanding nondestructive techniques to study the microstructure together with the vibrational and electronic states in low-dimensional systems composed of very small aggregates (nanocrystals, nanoparticles) dispersed in solid matrices. In particular, this technique is sensitive to the mean nanoparticle diameter, to the width of the particle size distribution, and to the particle-matrix interface conditions. The appearance of distinct peaks in the low-frequency region of Raman scattering has been established as due to acoustic-phonon modes confined in the homogenous nanoparticle volume.⁸⁻¹² Our previous studies¹³⁻¹⁷ confirmed that low-frequency Raman scattering, below 100 cm⁻¹, is very sensitive to microstructural features with characteristic lengths from one to tens of nanometers, i.e., intermediate scale between the molecular regime and the bulk one. We successfully applied this

^{a)} Author to whom correspondence should be addressed; electronic mail: kristina@physics.unlv.edu

technique to the microstructural studies of various glass compositions doped by semiconductor or dielectric particles, focusing specifically on the early stages of crystallization (such as nucleation) to determine the size, size distribution, and influence of the excitation radiation energy on the shape, frequency, and intensity of the nanoparticles' acoustic bands.⁸⁻¹⁷

In this paper we present the synthesis and the comprehensive microstructural investigations of glass-based optically transparent composites with a homogeneous distribution of metallic particles grown within the host glass matrix. We focus on the very early stages of crystallization in a soda-lime aluminosilicate glass system and study the confined acoustic-phonon modes of copper quantum dots by Raman-scattering spectroscopy. In particular, for nonresonant excitation, we examine the relationship between the energy and spectral shape of the low-frequency Raman peaks assigned to the eigenvibration modes of copper particles and their mean diameters. Furthermore, we employ high-resolution transmission electron microscopy (HRTEM), x-ray-diffraction (XRD) technique, and optical-absorption (OA) spectroscopy on a series of composites and compare the size of nanoparticles estimated from low-frequency Raman spectroscopy (LoFRS) with that derived from HRTEM.

II. EXPERIMENT

The starting material was as-quenched glass with basic composition of $76 \text{ SiO}_2-4\text{Al}_2\text{O}_3-6\text{CaO}-14\text{Na}_2\text{O}$ (in mol %) doped with 0.15 mol % of Cu_2O . After low-temperature sintering the powdered mixture of high-purity reagents was melted in a platinum crucible at a temperature of about 1500°C in reducing conditions. The liquid melt was cast into a brass mold, quenched by air cooling, and thermally annealed to relieve internal material stresses. As a result a good-optical-quality precursor glass was obtained. To induce nucleation, samples of as-quenched precursor glass were isothermally annealed at 650°C in air with a heating rate ranging from 1 up to 200°C , from 0.5 up to 400°C , and from 0.2 to $400^\circ\text{C}/\text{min}$ to the set temperature of 650°C , which is close to the glass transformation temperature. By varying the annealing time at 650°C between 5 and 60 min, a number of glass-ceramic composites with different mean diameters of copper particles representing the various nucleation and growth stages of quantum-sized nanocrystals were synthesized. For optical studies, the samples were cut to rectangular plates of 2–3-mm thickness. After thermal treatments, the glass plates were carefully polished to minimize the intensity of elastic light scattering.

Room-temperature optical-absorption spectra were measured in the range from 400 to 800 nm using a Shimadzu UV-3100 PC dual-beam spectrophotometer. The Raman-scattering spectra were excited by means of a krypton-ion laser line at 647 nm to provide off-resonance excitation conditions. The Raman spectra were recorded at room temperature both in Stokes and in anti-Stokes sides, with a laser power of about 300 mW in a 90° scattering geometry using a Jobin-Yvon double-pass monochromator with holographic

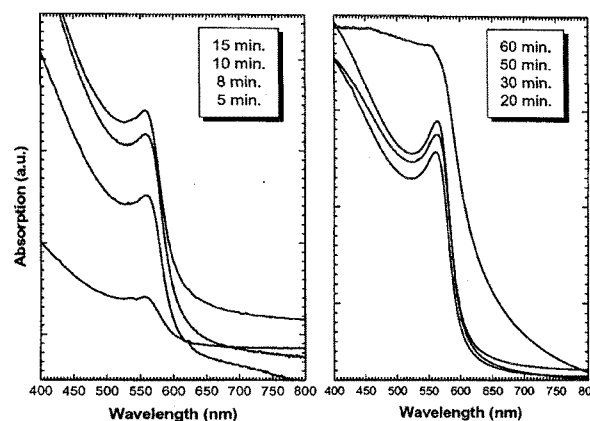


FIG. 1. Optical absorption spectra of a number of composites annealed isothermally (650°C) for periods of time between 5 and 60 min. The band at 560 nm attributed to the surface-plasmon resonance of copper nanoparticles increases gradually its intensity, indicating an increase of the particles' mean size and density with the annealing time.

gratings and a photomultiplier, operated in photon counting mode, as a detection system. Both Stokes and anti-Stokes spectra were recorded at data intervals of $0.1-0.5 \text{ cm}^{-1}$. To avoid local laser heating a cylindrical lens was applied to focus the laser beam on the sample surface. Under the adopted experimental conditions no changes in the optical properties of all studied samples were observed. XRD patterns were collected in angle-dispersive mode using a Rigaku diffractometer in $\theta-2\theta$ Bragg-Brentano geometry, $\text{Cu } K\alpha$ radiation, and a graphite monochromator for the diffracted beam. HRTEM studies were carried out on the powdered samples dispersed over carbon-coated copper grids using a Philips 400T microscope operating at 120 kV.

III. RESULTS AND DISCUSSION

The experimental techniques adopted in this study, LoFRS, HRTEM, and XRD, confirmed the amorphous nature of the as-quenched precursor glass. As a result of isothermal treatments distinct changes in the glass microstructure were detected. A copper particle nucleation process was observed, with the particles' mean diameter gradually increasing with the time of thermal annealing.

A. Optical spectra

The optical-absorption spectra of the metal-dielectric composites, isothermally annealed at 650°C are shown in Fig. 1. The absorption bands with maxima at about 560 nm present in the spectra of all composites have been assigned to the surface-plasmon resonance (SPR) of copper nanoparticles. Similar bands, observed for copper-implanted SiO_2 glasses or Al_2O_3 thin films, were explained by the plasmon oscillations of the free electrons also known as plasma resonance bands.²¹⁻²⁵ As shown in Fig. 1, the optical absorption of the composites is considerably affected by the nucleation and consecutive growth of particles in the host glass. As the annealing time is raised from 5 to 15 min, the absorption band shifts slightly towards shorter wavelengths and its intensity increases markedly. These changes indicate that the

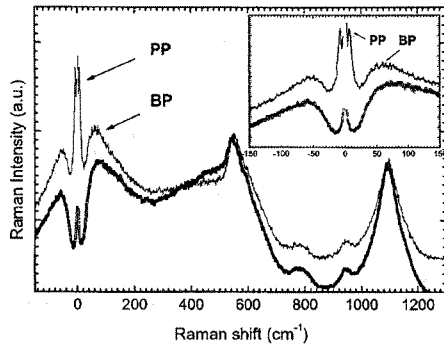


FIG. 2. Room-temperature, VV polarized Stokes, and anti-Stokes Raman-scattering spectra of the as-quenched precursor glass (dotted line) and of the glass-ceramic composite annealed for 30 min at 650 °C (solid line). The inset shows a zoom on the low-frequency region of scattering. “PP” indicates the particle peak assigned to spheroidal, symmetric ($l=0$) acoustic-phonon modes confined in copper nanoparticles nucleated in the host glass matrix; “BP” points toward the boson band.

mean size of particles increases along with the time of thermal annealing. For composites annealed over 15 min the intensity of the SPR band increases slightly, without any apparent shift in the position of its maximum. We explain this behavior as due to an increase of the copper particles’ density accompanied by only a little increase in the particles’ mean size. In particular, for composites annealed for more than 20 min, the mean particle size does not grow much, therefore the enhancement of the SPR band intensity is mostly due to the increased particles’ density (confirmed by LoFRS spectroscopy, see Sec. III B).

B. Low-frequency Raman-scattering studies

The resonance Raman spectra were collected with the excitation energy located outside the absorption region common for all composites. Figure 2 presents room-temperature Stokes and anti-Stokes Raman-scattering spectra of as-quenched precursor glass and one of the synthesized glass-ceramic composites. The spectra presented in Fig. 2 are very similar in the high-frequency region of scattering. In the low-frequency region the dominant feature is an asymmetric band with a long tail toward the high-energy, called the boson peak (BP). The BP behavior follows in temperature the Bose-Einstein factor, indicating its origin in nearly harmonic excitations, and originates from disorder-induced light scattering due to acoustic phonons. The major difference between the as-quenched glass and the annealed glass spectra is observed in the very-low-frequency spectral region (see Fig. 2, inset). The glass-ceramic composite exhibits strong scattering peaks, both in Stokes and anti-Stokes sides. These distinct peaks appearing in the Raman spectra between the BP and the Rayleigh line have been assigned to acoustic-phonon modes confined in copper nanoparticles nucleated in the host glass matrix. Similar low-frequency peaks have been observed in several nanocomposite systems, where dielectric,^{5,13,14} semiconductor,^{6,9,12} or metallic^{1,2,4,7} particles were embedded into transparent vitreous matrices. These peaks were attributed to acoustic-phonon modes confined in homogeneous particles (nanocrystals, clusters, aggregates,

etc.) and they can provide direct information on their diameters. The energies of these vibration eigenmodes depend on the elastic properties of the material (longitudinal to transverse sound velocity ratio) and are also a function of the particle diameter. In a simplified model^{8,11} that considers vibrations of a free homogeneous elastic particle only two types of acoustic modes are expected to be Raman active, namely, the spheroidal modes labeled $l=0$ (symmetric) and $l=2$ (quadrupolar). The classification of these modes is performed following the symmetry group of a sphere, with the indices l and m equivalent to the spherical harmonics Y_l^m . The spheroidal, symmetric modes $l=0$ are purely radial with spherical symmetry and active only in VV polarization^{8,11} but quadrupolar modes are depolarized (active both in VV and HV polarizations), so the depolarization ratio I_{HV}/I_{VV} allows one to assign the Raman spectra to symmetrical or quadrupolar vibrations. The frequencies of these surface vibration symmetric or quadrupolar spheroidal modes, i.e., the lowest-energy modes, are given by

$$\omega_0 = A_0 v_l / 2rc, \quad (1)$$

$$\omega_2 = A_2 v_l / 2rc, \quad (2)$$

for $l=0$ or $l=2$, where ω_0 and ω_2 are the frequencies of the observed vibrational modes, v_l is the longitudinal sound velocity, v_t is the transverse sound velocity, A_0 (A_2) is a proportionality coefficient depending on the angular momentum l , the harmonic number n , and the ratio between the transverse and longitudinal sound velocities v_t/v_l , c is the velocity of light in vacuum, and $2r$ is the diameter of the vibrating sphere. From the frequency position and the line shape of the low-frequency Raman peaks, we can derive the mean particle size and the size distribution of the vibrating particles, nanocrystals, or clusters. Montagna and Dusi¹¹ calculated the values of A_0 and A_2 coefficients as a function of v_t/v_l in the form of dimensionless wave numbers. Using the calculation results of Montagna and Dusi¹¹ and the sound velocities for bulk copper $v_l=4828$ m/s and $v_t=2648$ m/s, we obtained the value $A_0=0.83$.

Low-frequency, VV polarized Stokes, and anti-Stokes Raman spectra of a series of isothermally treated glasses with nucleated copper particles are presented in Figs. 3(a)–3(c) (plots B). The as-quenched precursor glass annealed at 650 °C for 10 min does not exhibit well-defined peaks, but showed small intensity bands in the low-frequency region of scattering. However, the spectra of samples annealed at the same temperature for extended periods of time such as 30 and 60 min exhibit distinct peaks in the scattering region between the Rayleigh line and the BP. These very-low-frequency peaks, observed only in VV polarization, have been assigned to the symmetric spheroidal ($l=0$) surface vibrational modes of the copper particles.

In order to isolate the amount of light scattering due to the acoustic modes of the nanoparticles from the total amount of low-frequency scattering, spectral subtractions were performed. This procedure was indispensable, since the scattering contribution from the host glass presents a broad band—the BP—in the frequency range of our interest. This operation of subtraction cannot be performed in a straight-

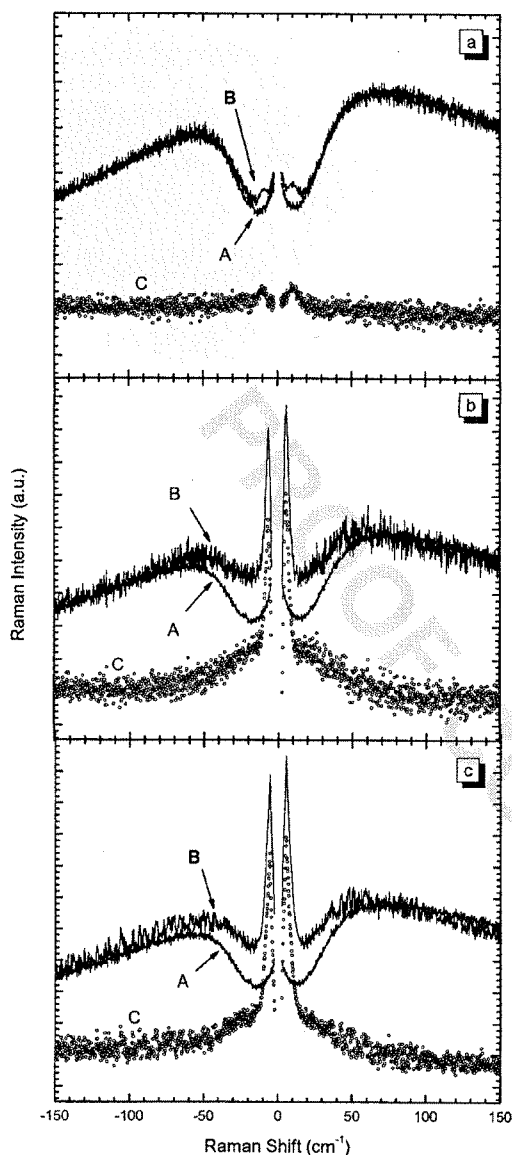


FIG. 3. Comparison of the low-frequency VV polarized Stokes and anti-Stokes Raman-scattering spectra of a series of composites with nucleated copper particles and different isothermal (650 °C) annealing times: (a) 10, (b) 30, and (c) 60 min. "A" marks as-quenched glasses, "B" marks annealed composites, and "C" displays difference spectra showing the scattering contribution due only to the acoustic phonons of the copper particles. For the shortest annealing time (10 min) only an enhancement of scattering in the region between the Rayleigh line and the Boson band can be noticed. For longer annealings, however, distinct low-frequency peaks appear and are assigned to the surface vibrational ($l=0$) modes of the copper nanoparticles.

forward way because the Raman spectra of the annealed and of the as-quenched precursor glass are not the same. In particular, the normalized spectral intensity of the broad band centered at about 100 cm^{-1} , assigned to the boson peak, is stronger in the annealed glass than in the as-quenched one. The spectra, after corrections including a subtraction of the luminescence background and normalization, were completely overlapped in the spectral region of interest. After this procedure, the spectrum of the as-quenched glass and of the annealed samples could be reasonably superimposed and subtracted.

Besides the scattering spectra of thermally treated samples, Figs. 3(a)–3(c) also illustrate the spectra of the as-quenched precursor glass (plots A) together with the difference spectra (plots C) that show the scattering contribution due only to the acoustic phonons of the copper particles. With the increased time of isothermal treatments, the position of the acoustic peaks shifts slightly towards lower frequencies, indicating a gradual increase of the diameter of copper nanocrystals. The systematic increase of the acoustic peak areas indicates an increasing number of scattering centers, that is, the particles' density. The observed low-frequency acoustic-phonon peaks are centered at 9 cm^{-1} [Fig. 3(a)], 6.1 cm^{-1} [Fig. 3(b)], and 5.5 cm^{-1} [Fig. 3(c)] with a full-width half-maximum (FWHM) estimated from a Gaussian distribution to be 14.0 ± 0.7 , 3.2 ± 0.1 , and $4.7\pm 0.2\text{ cm}^{-1}$, respectively. The mean nanoparticle diameters calculated from the frequency position of the maximum of the acoustic peaks [Eq. (1)] were found to be 14.8, 21.9, and 24.3 nm, respectively. We used a Gaussian distribution to fit the spectral line shape of the Raman peaks and obtained similar results: $\langle d \rangle = 13.6$, 21.1, and 22.6 nm, respectively, with $\sigma_d = 0.9$, 1.4, and 1.8 nm, respectively, where σ_d is the standard deviation of the Gaussian distribution around the mean diameter. The model provides a smaller mean diameter than that directly obtained from Eq. (1) by using the peak positions. This is due to the fact that the Raman intensities of the particle modes are proportional to the volume of the particles themselves; different Raman weights produce an inhomogeneous Raman line shape with a maximum of the amplitude which does not correspond to the maximum of the size distribution.

We would like to mention that in the spectra of all composites investigated, we did not observe the quadrupolar acoustic particle modes ($l=2$) that are expected to be present at lower frequencies than the symmetric $l=0$ modes. One probable reason for the absence of these modes is that their VV contribution is hidden by the low-frequency tail of the far more intense spectral contribution of the symmetric spheroidal modes due to the vibrations of larger particles. The other reason is that it is impossible to separate the contribution of quadrupolar modes from the elastic part of light scattering that produces a strong intensity at very low frequencies ($\omega < 5\text{ cm}^{-1}$). In this frequency range our experimental apparatus is not able to resolve a peak from the elastic line. Figure 3 (plots C) illustrates a low-energy shift of the particle peaks, as well as an enhancement of the scattering contribution of the nanoparticles' acoustic modes, as the time of isothermal annealing increases. Furthermore, in the advanced stages of nucleation the observed energy shift is accompanied by the inhomogeneous broadening of the acoustic peaks that increases notably with the time of thermal treatment (30 min and above). Such spectral broadening indicates a wide distribution of particle diameters nucleated in the glass matrix.

C. Transmission electron microscopy and x-ray-diffraction studies

HRTEM investigations were performed on several grains of the as-quenched glass powder as well as on grains of the

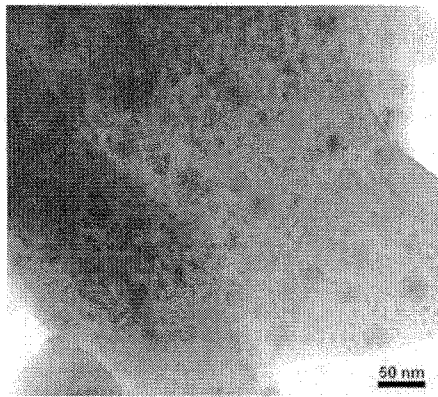


FIG. 4. HRTEM micrograph of one of the synthesized metal-dielectric composites (30 min at 650 °C) showing the microstructure of the host glass and the embedded copper nanoparticles. The estimated crystallite size ranges from ~21 to ~24 nm.

thermally treated materials. For the precursor glass selective area diffraction (SAD) patterns did not reveal any crystalline reflection except for the typical halo of amorphous systems. However, for the thermally treated glasses the SAD patterns revealed the presence of diffraction rings. The HRTEM images of composites showed coherently scattering domains, uniformly distributed in the glass matrix, confirming the nucleation of nanoparticles. The micrograph in Fig. 4 shows the image of one of the studied nanocomposites (30 min at 650 °C). The estimated crystallite size ranges from ~21 to ~24 nm. The mean diameter of copper particles obtained from HRTEM images is slightly larger compared with that calculated from LoFRS spectroscopy. An amorphous structure of the host glass is still evident in the image of the nanocomposite, as was confirmed by LoFRS spectroscopy, angle-dispersive XRD patterns, and by the diffuse halo visible in the SAD patterns.

The angle-dispersive x-ray-diffraction patterns of the as-quenched precursor glass and of the thermally annealed metal-dielectric composites are presented in Fig. 5. The spectral profile of all the diffraction patterns is very similar and the precursor glass as well as all thermally annealed composites exhibit haloes typical of amorphous systems. The x-ray-diffraction patterns indicated the absence of crystalline phases in the studied composites. However, with annealing time, a noticeable decrease of the intensity of the haloes characteristic of the amorphous phase was observed in the low- 2θ range (see inset in Fig. 5). These changes have been attributed to the structural rearrangements within the host matrix, more specifically to the modification of short-range order in the glass network associated with the nucleation and growth of nanometer-sized copper particles. The low concentration of particles in the glass matrix as well as the very small volume of the nucleated nanocrystals could explain the lack of x-ray-diffraction peaks of metallic copper on the collected patterns.

IV. CONCLUSIONS

We have successfully synthesized a series of metal-dielectric composites with nanometer-sized copper clusters

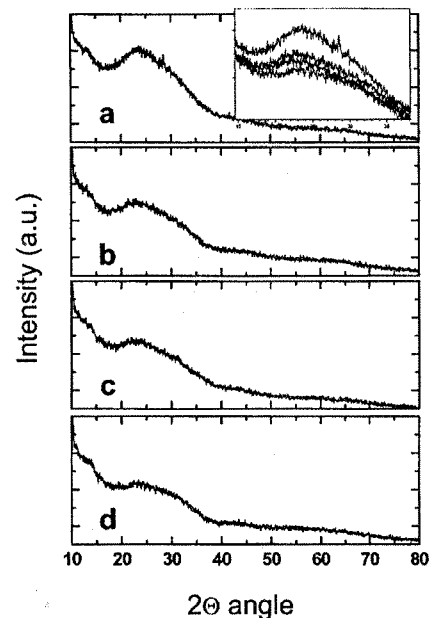


FIG. 5. X-ray-diffraction patterns of as-quenched precursor glass (a) and of metal-dielectric composites isothermally annealed for increasing times: (b) 15, (c) 30, and (d) 60 min. The as-quenched glass as well as all composites exhibit haloes typical of amorphous systems and do not show any presence of a crystalline phase. The only observed difference is in the low- 2θ range, where the amorphous haloes become less and less intense with increasing annealing time, as shown in the inset.

embedded in a soda-lime-silicate host glass. The optical-absorption spectra indicated the presence of the surface-plasmon resonance bands of copper nanoparticles. The continuous rise in intensity of the plasmon resonance bands was explained mainly in terms of the increase of the particles' density as a function of the annealing time. The diameter and the concentration of the nanocrystalline phase nucleated in the glass matrix were modified by varying the conditions of isothermal heat treatments. The Raman studies were focused, in particular, on the low-frequency region of scattering. The LoFRS spectroscopy has again emerged as an excellent non-destructive technique permitting the detection of the presence of the nanoparticles (nanoclusters, nanoaggregates) embedded in a solid matrix and the estimation of their mean diameters. In thermally annealed glasses, the LoFRS spectra revealed the presence of very-low-frequency strong scattering peaks located between the boson band and the Rayleigh line. These peaks have been assigned to the acoustic-phonon modes and specifically to the low-energy surface vibrational (symmetric, $l=0$) modes of copper nanoparticles. The increase of the time of isothermal annealings resulted in the growth of nanoparticles, which was confirmed by LoFRS spectroscopy as well as by HRTEM and optical-absorption results. The diameters of the nanocrystals, and their size distribution, estimated from Raman experiments, were confirmed to be slightly larger by HRTEM. In consideration of potential practical applications of the synthesized metal-dielectric nanocomposites, we anticipate to study their non-linear properties, in particular, as a function of particle diameter.

ACKNOWLEDGMENTS

Part of this work was done under financial support of the Advanced Research Institute for Science and Engineering, Waseda University, Tokyo (Japan). The authors acknowledge the Nippon Electric Glass Company, Kyoto (Japan) for technical advice and the use of their facilities for samples preparation. The authors gratefully acknowledge the support from the U.S. Department of Energy Cooperative Agreement No. FC08-01NV14049 with the University of Nevada, Las Vegas.

- ¹A. Stepanov, D. E. Hole, and P. D. Townsend, *J. Non-Cryst. Solids* **260**, 65 (1999).
- ²E. Borsella, E. Cattaruzza, G. DeMarchi, F. Gonella, P. Mazzoldi, G. Battaglin, and R. Polloni, *J. Non-Cryst. Solids* **245**, 1221 (1999).
- ³F. Auzel, K. E. Lipinska-Kalita, and P. Santa Cruz, *Opt. Mater.* **5**, 75 (1996).
- ⁴G. DeMarchi, F. Gonella, and P. Mazzoldi, *J. Non-Cryst. Solids* **196**, 79 (1996).
- ⁵R. F. Haglund, L. Yang, R. H. Magruder, J. E. Wittig, K. Becker, and R. A. Zuhr, *Opt. Lett.* **18**, 37 (1993).
- ⁶T. Tokizaki, A. Nakamura, S. Kaneko, K. Uchida, S. Omi, H. Tanji, and Y. Asahara, *Appl. Phys. Lett.* **65**, 941 (1994).
- ⁷L. Yang, K. Becker, R. H. Magruder, R. F. Haglund, L. Yang, R. Dorsinville, R. R. Alfano, and K. Zuhr, *J. Opt. Soc. Am. B* **11**, 457 (1994).
- ⁸E. Duval, A. Boukenter, and B. Champagnon, *Phys. Rev. Lett.* **56**, 2052 (1986).
- ⁹V. K. Malinovsky, V. N. Novikov, A. P. Sokolov, and V. G. Dodonov, *Solid State Commun.* **67**, 725 (1988).
- ¹⁰G. Mariotto, M. Montagna, G. Viliani, E. Duval, S. Lefrant, E. Rzepka, and C. Mai, *Europhys. Lett.* **6**, 239 (1988).
- ¹¹M. Montagna and R. Dusi, *Phys. Rev. B* **52**, 10080 (1995).
- ¹²M. Ivanda, K. Babocsi, C. Dem, M. Schmitt, M. Montagna, and W. Kiefer, *Phys. Rev. B* **67**, 235329 (2003).
- ¹³K. E. Lipinska-Kalita and G. Mariotto, *J. Mol. Struct.* **267**, 241 (1992).
- ¹⁴K. E. Lipinska-Kalita, F. Auzel, and P. Santa-Cruz, *J. Non-Cryst. Solids* **204**, 188 (1996).
- ¹⁵K. E. Lipinska-Kalita, G. Mariotto, and E. Zanghellini, *Philos. Mag. B* **71**, 547 (1995).
- ¹⁶R. Ceccato, R. DalMaschio, G. Mariotto, M. Montagna, F. Rossi, M. Ferrari, K. E. Lipinska-Kalita, and Y. Ohki, *J. Appl. Phys.* **90**, 2522 (2001).
- ¹⁷R. Ceccato, R. DalMaschio, M. Ferrari, K. E. Lipinska-Kalita, G. Mariotto, M. Montagna, and Y. Ohki, *J. Raman Spectrosc.* **32**, 643 (2001).
- ¹⁸R. Shuker and R. W. Gammon, *Phys. Rev. Lett.* **25**, 222 (1979).
- ¹⁹L. Saviot, B. Champagnon, E. Duval, I. A. Kudriatsev, and A. I. Ekimov, *J. Non-Cryst. Solids* **197**, 238 (1996).
- ²⁰E. Duval, H. Portes, L. Saviot, M. Fuji, K. Sumitomo, and S. Hayashi, *Phys. Rev. B* **63**, 075405 (2001).
- ²¹R. Doremus, K. Shou-Chen, and R. Garcia, *Appl. Opt.* **31**, 5773 (1992).
- ²²T. Akai, Y. Yamanaka, and H. J. Wakabayashi, *J. Am. Ceram. Soc.* **79**, 859 (1996).
- ²³I. Nakai, C. Numako, H. Hosono, and Y. Yamasaki, *J. Am. Ceram. Soc.* **82**, 689 (1999).
- ²⁴Y. Ito, H. Jain, and D. B. Williams, *Appl. Phys. Lett.* **75**, 3793 (1999).
- ²⁵F. D'Acapito, S. Mobilio, G. Battaglin, E. Cataruzza, F. Gonella, F. Caccavale, P. Mazzoldi, and J. R. Regnard, *J. Appl. Phys.* **87**, 1819 (2000).



ELSEVIER

Available online at www.sciencedirect.com

SCIENCE @ DIRECT®

Physica B 365 (2005) 155–162

PHYSICA B

www.elsevier.com/locate/physb

Effects of high pressure on stability of the nanocrystalline $\text{LiAlSi}_2\text{O}_6$ phase of a glass–ceramic composite: A synchrotron X-ray diffraction study

Kristina E. Lipinska-Kalita^{a,*}, Gino Mariotto^b, Patricia E. Kalita^c,
Yoshimichi Ohki^d

^aHigh Pressure Science and Engineering Center, Department of Physics, University of Nevada Las Vegas, Las Vegas, NV 89154, USA

^bDipartimento di Fisica, Università di Trento, 38050 Povo (Trento), Italy

^cDepartment of Physics, University of Nevada Las Vegas, Las Vegas, NV 89154, USA

^dDepartment of Electrical Engineering and Bioscience, Waseda University, Shinjuku, Tokyo 169-8555, Japan

Received 5 January 2005; received in revised form 1 May 2005; accepted 9 May 2005

Abstract

Synchrotron X-ray diffraction studies, under pressures up to 50 GPa, have been performed on a lithium–aluminosilicate glass–ceramic composite with nanometer-sized $\text{LiAlSi}_2\text{O}_6$ crystals embedded in a host matrix. The pressure-induced evolution of X-ray diffraction patterns was followed in a diamond anvil cell on compression and decompression cycles with the aim of probing the effect of high-pressure compression on the nanocomposite structure. On the compression cycle from ambient pressure up to 20 GPa the unit cell volume of the $\text{LiAlSi}_2\text{O}_6$ phase decreased by about 22%. The diffraction patterns also revealed the presence, at high pressures, of the ZrTiO_4 phase that was nucleated in the matrix prior to the crystallization of the main $\text{LiAlSi}_2\text{O}_6$ phase. After quenching from 50 GPa to close to ambient conditions the diffraction pattern indicated that the high-pressure phase was retained to some extent although the decompressed structure still carried the signature of the initial ambient $\text{LiAlSi}_2\text{O}_6$ phase. A Birch–Murnaghan fit of the unit cell volume as a function of pressure yielded a zero pressure bulk modulus $K_0 = 71 \pm 2$ GPa and its pressure derivative $K'_0 = 4.4 \pm 0.6$ GPa for the nanocrystalline phase.

© 2005 Elsevier B.V. All rights reserved.

PACS: 61.10.–I; 61.46.+w; 61.82.Rx; 62.50.+p

Keywords: High-pressure; Synchrotron X-ray diffraction; Nanocrystals; Glass–ceramics; Composites

*Corresponding author. Tel.: +1 7028952536; fax: +1 7029850804.

E-mail address: kristina@physics.unlv.edu (K.E. Lipinska-Kalita).

1. Introduction

Composite materials consisting of nanosized crystals or quantum dots embedded in solid matrices currently inspire considerable research interest. Crystalline particles or clusters, dispersed in optically transparent matrices, such as glasses, belong to three-dimensional quantum-confined systems and their properties are affected by the confinement processes in the nanosized volumes (electrons, holes, excitons, phonons) [1–7].

High-pressure techniques offer the extraordinary possibility to synthesize novel solids with unique thermo-mechanical, electronic, magnetic or optical properties—what is nowadays a major challenge in materials research [8–15]. High-pressure studies of nanostructured analogs of bulk materials, that is of nanosized structures, are critical for identifying new equilibrium and metastable states, that can be accessed as these materials are compressed to very small volumes. In particular, pressure-driven modifications of crystalline nanostructures embedded in solid matrices are attractive from both a fundamental physics point of view as well as the exciting prospect of fabricating novel materials [12–15].

Many technological applications require a substrate material with a close to zero coefficient of thermal expansion, as well as an excellent chemical and shock resistance. Lithium-aluminosilicate glass-ceramics have gained considerable commercial attention because of their very low thermal expansion, transparency, high chemical durability, and strength [16–19]. Some of many widespread applications of such ceramics are telescope mirror blanks, ring-laser gyroscopes and optically stable platforms.

The material investigated in this study belongs to the low thermal expansion $\text{Li}_2\text{O}-\text{Al}_2\text{O}_3-\text{SiO}_2$ glass-ceramic system with a double-layered nanocrystalline phase composed of ZrTiO_4 core phase and $\text{LiAlSi}_2\text{O}_6$ shell phase homogeneously dispersed within the glass matrix. The goal of this work was to examine the resistance to high-pressure compressibility and potential structural transformations in the nanocrystalline phase of the composite system where the metastability of the amorphous phase was partially relieved by crystal

nucleation and growth process. Using a diamond anvil cell and synchrotron X-ray radiation techniques, we followed the pressure-induced structural changes in the nanocrystalline phase of the $\text{Li}_2\text{O}-\text{Al}_2\text{O}_3-\text{SiO}_2$ glass-ceramic system. The studies were performed on compression up to 50 GPa and subsequent decompression down to ambient conditions.

To the best of our knowledge, this work is the first attempt to measure the equation of state of $\text{LiAlSi}_2\text{O}_6$ nanocrystals embedded in a lithium-aluminosilicate, glass-based composite system.

2. Experimental

The investigated nanocomposite belongs to the glass-ceramic system of $\text{Li}_2\text{O}-\text{Al}_2\text{O}_3-\text{SiO}_2$ that is well known to exhibit very low thermal expansion. The mixture for the glass precursor material of the glass-ceramic composite had composition represented by 65 SiO_2 :22 Al_2O_3 :5 Li_2O :2 Na_2O :2 K_2O (wt%) with 2 TiO_2 and 2 ZrO_2 added as nucleation agents. This composition is close to commercially available Schott glass-ceramics. The high-purity batch components were sintered at low temperature and afterwards melted in a platinum crucible at 1600 °C in air. The liquid melt was cast into a brass mold resulting in an optically transparent glass. To induce nucleation in the glass matrix, double thermal treatments below the glass transition temperature were performed. The first treatment (750 °C) resulted in the creation of the ZrTiO_4 nuclei and the second (850 °C) in the growth of $\text{LiAlSi}_2\text{O}_6$ crystals around the nuclei. In the final material, the nanocrystalline phase, with an average diameter of approximately 50 ± 5 nm as determined by high-resolution transmission electron microscopy, was homogeneously dispersed in the host glass matrix.

For in situ X-ray diffraction studies the powdered sample was compressed in a Mao-Bell-type diamond anvil cell (DAC). A rhenium gasket was preindented to a thickness of 45 μm using diamonds with 300 μm diameter culets. The sample chamber consisted of a 150 μm diameter hole drilled in the preindented rhenium gasket. A few grains of ruby powder were included and used to

measure the pressure. No pressure-transmitting medium was used in this experiment. The time gap between a pressure raise and the subsequent X-ray measurement was about 10 min. All X-ray diffraction patterns were collected at the 16-ID-B undulator beamline at the High Pressure Collaborative Access Team (HPCAT), sector 16 of the Advanced Photon Source of Argonne National Laboratory, using a monochromatic beam of 0.3888 Å wavelength. The diffracted X-rays were collected with an image plate (Mar-345) detector placed at 353 mm from the samples. The $10\ \mu\text{m} \times 10\ \mu\text{m}$ X-ray beam was achieved by microfocusing with two Kirkpatrick-Baez mirrors and a $30\ \mu\text{m}$ diameter Mo cleanup pinhole to eliminate the beam tails. The collected diffraction patterns were analyzed by integrating of images as a function of 2θ angle using the program FIT2D [20] in order to obtain conventional, one-dimensional diffraction profiles. The diffraction patterns were subsequently processed with programs like Powder Cell 2.4 [21], Jade 6.5 [22], and General Structure Analysis System (GSAS) [23,24].

3. Results and discussion

A typical Rietveld profile refinement [23,24] of a diffraction pattern collected in situ (DAC) at 0.2 GPa, the lowest pressure investigated, is presented in Fig. 1. This pattern is consistent with a hexagonal unit cell. The identified space group is $P6_22$ and the refined unit cell constants for this low-pressure phase of $\text{LiAlSi}_2\text{O}_6$ are: $a = 5.17 \pm 0.02\ \text{Å}$ and $c = 5.44 \pm 0.02\ \text{Å}$, with the calculated cell volume $V = 125.9 \pm 0.9\ \text{Å}^3$ and density $d = 2.45\ \text{g/cm}^3$.

The full-profile Rietveld fit is excellent and explains all diffraction lines present. The hexagonal structure can be fitted to all diffraction data collected from 0.2 GPa pressure up to about 20 GPa.

High-pressure compression of the glass-ceramic composite was investigated in situ (in the DAC) from close to the ambient pressure up to 50 GPa. The X-ray diffraction patterns on the compression sequence from 0.2 to 50 GPa are presented in Fig. 2. As shown in Fig. 2, at low pressures the

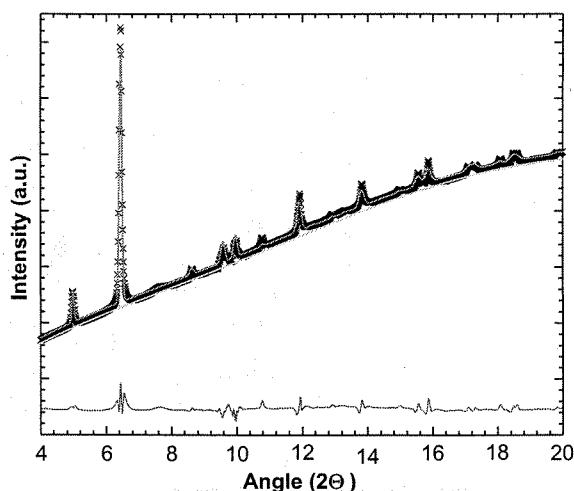


Fig. 1. Typical Rietveld full-profile refinement performed using the GSAS program [23,24] of the X-ray diffraction pattern collected in DAC at 0.2 GPa. The refinement was carried out using the hexagonal space group $P6_22$. The solid red line and black stars represent modeled and experimental patterns, respectively. The blue solid line represents the difference between the observed and the refined profile.

patterns are dominated by Bragg lines corresponding to the hexagonal $\text{LiAlSi}_2\text{O}_6$ phase.

With pressure increase the positions of these lines systematically shift towards higher 2θ angles, lower d spacings as can be clearly seen in Figs. 2 and 4. Over the entire pressure range the profiles of the diffraction lines assigned to the $\text{LiAlSi}_2\text{O}_6$ nanocrystalline phase undergo gradual broadening. New diffraction lines appear starting from about 2 GPa and have been attributed to the ZrTiO_4 phase nucleated in the glass matrix in the first thermal treatment (Fig. 2 (a) and (b)). More specifically, as pressure rises up to about 2 GPa a small intensity line of the ZrTiO_4 phase (111) is observed at the angle of 7.8° (Fig. 2(a)). An increase in pressure up to 17 GPa introduces another new line that could most probably be attributed to the 002 line of ZrTiO_4 phase. With further pressure raise the intensity of the 111 ZrTiO_4 line increases markedly and at about 20 GPa it becomes comparable to what we attributed to be the main 101 line of the $\text{LiAlSi}_2\text{O}_6$ phase (Fig. 2(b)). This line disappears above 22 GPa while both the 111 and 002 lines of

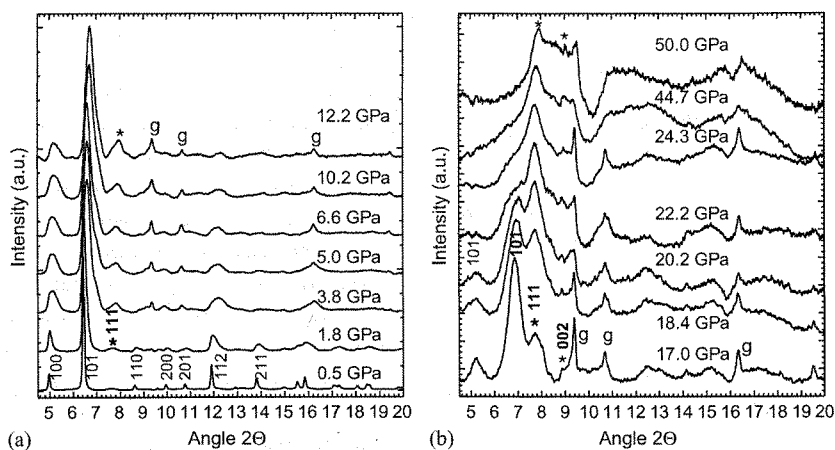


Fig. 2. (a) and (b) X-ray diffraction patterns collected on compression from 0.2 to 50 GPa. Miller indices are labeled for each reflection. New lines of the ZrTiO_4 phase are marked by asterisks. Gasket lines are indicated by the letter g.

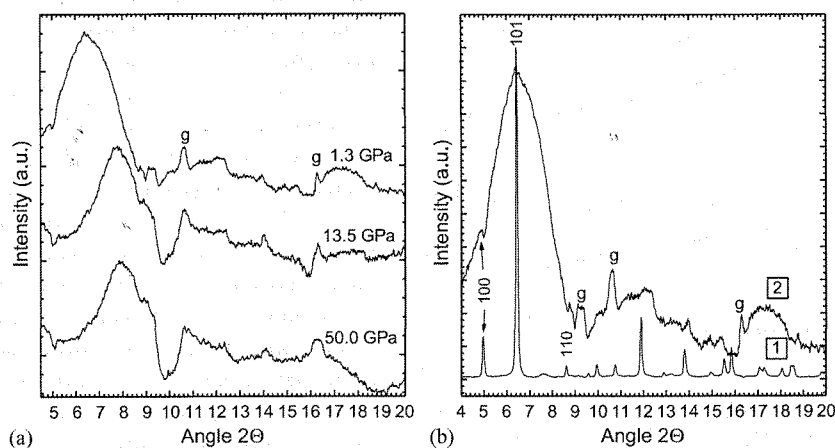


Fig. 3. (a) X-ray diffraction patterns collected on decompression from 50 GPa down to 0.8 GPa. Miller indices are labeled for relevant reflections. Gasket lines are indicated by the letter g. (b) Comparison of the pattern collected at the beginning of the compression sequence (0.2 GPa, plot 1) and at the end of the decompression (plot 2).

the ZrTiO_4 phase persist up to 50 GPa and show a significant pressure-induced broadening. Fig. 3 shows the diffraction patterns of the glass–ceramic nanocomposite on decompression from 50 GPa down to 0.8 GPa. All the diffraction patterns are dominated by the strong intensity, broad band that increases in intensity and shifts gradually to lower 2θ angles with decrease of pressure (Fig. 3(a)). Remarkably on decompression to 0.8 GPa the maximum of this main band returns to what

was the position of the 101 line of the $\text{LiAlSi}_2\text{O}_6$ phase at the beginning of the compression cycle (Fig. 3(b)). Since the width of the main band covers a wide 2θ angle range (between 4° and 9°) we could consider this band as being a blend of the 100 and 101 lines of the $\text{LiAlSi}_2\text{O}_6$ phase mixed with the 111 and 002 lines of the ZrTiO_4 phase.

In order to discuss the impact of high-pressure compression on the structure of the nanocrystalline phase of the composite, we have to keep in

mind that inside of the glass matrix there is a complex nanocrystalline phase, built of ZrTiO_4 cores, each wrapped by a shell of $\text{LiAlSi}_2\text{O}_6$. In the most plausible scenario the surrounding isotropic glass matrix distributes the impact of high pressure to the matrix–nanoparticle interface, however it does not substitute entirely for a hydrostatic pressure transmitting medium. The first effect of the compression is that the unit cell of the shell layer structure decreases, what is well illustrated by the initial shift of all $\text{LiAlSi}_2\text{O}_6$ diffraction lines towards higher angles, lower d spacings (Fig. 2 and 4). Further, the compression process causes partial amorphization of the shell layer and reveals more and more of the core material. This is confirmed by the appearance of the diffraction lines attributed to the core ZrTiO_4 phase in the patterns above 2 GPa (Fig. 2). The pressure-induced amorphization of the nanoparticles' shell, accompanied by line broadening, continues up to about 22 GPa at which pressure the only lines present in the diffractograms are those of the core phase. With pressure increase above 22 GPa the lines of the ZrTiO_4 phase become broad indicating that the core phase is also undergoing a pressure-induced amorphization.

In the decompression cycle (Fig. 3), the broad diffraction band dominating the pattern shifts towards lower angles reaching at the end of the decompression sequence the position that was of the shell $\text{LiAlSi}_2\text{O}_6$ phase at 0.5 GPa, the initial pressure in this experiment (Fig. 3(b)). It is plausible to hypothesize that this band is composed of the broadened lines of $\text{LiAlSi}_2\text{O}_6$ (100 and 101) overlapped with the lines of the ZrTiO_4 core phase (111 and 002). If this is the case, the large bandwidth suggests that both structures contributing to this diffraction band are highly disordered. In analogy to what happens with flexible structures exposed to pressure, we may also argue that in the compression mechanism of the investigated nanocomposite the bond lengths and angles may vary temporarily without breaking of the bonds and display X-ray detectable amorphization, comparable to a plastic deformation of the parent lattice. Based on the above discussion, we postulate that after pressure releases down to 0.8 GPa the high-pressure phase is retained to

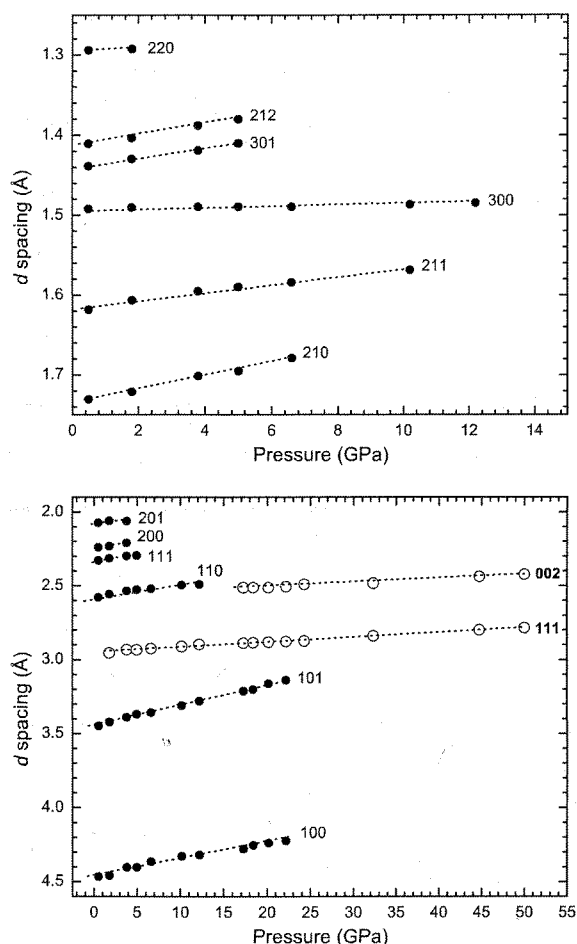


Fig. 4. Pressure dependence of the interplanar d spacings. Compression decreases the interplanar d spacings inducing a progressive densification of the nanocrystals. The filled and the empty circles indicate the $\text{LiAlSi}_2\text{O}_6$ and the ZrTiO_4 phases, respectively. Miller indices are labeled for each reflection. Dotted lines are guides for the eye.

some extent, although the decompressed structure still carries the signature of the initial (0.2 GPa) $\text{LiAlSi}_2\text{O}_6$ phase.

The pressure dependence of the d spacings and the calculated unit cell parameters of the $\text{LiAlSi}_2\text{O}_6$ nanocrystalline phase are shown in Figs. 4 and 5, respectively. Compression decreases the interplanar d spacings inducing a progressive densification of the nanocrystals. The pressure dependence of the density of the $\text{LiAlSi}_2\text{O}_6$ phase is shown in Fig. 6. On compression from 0.2 to

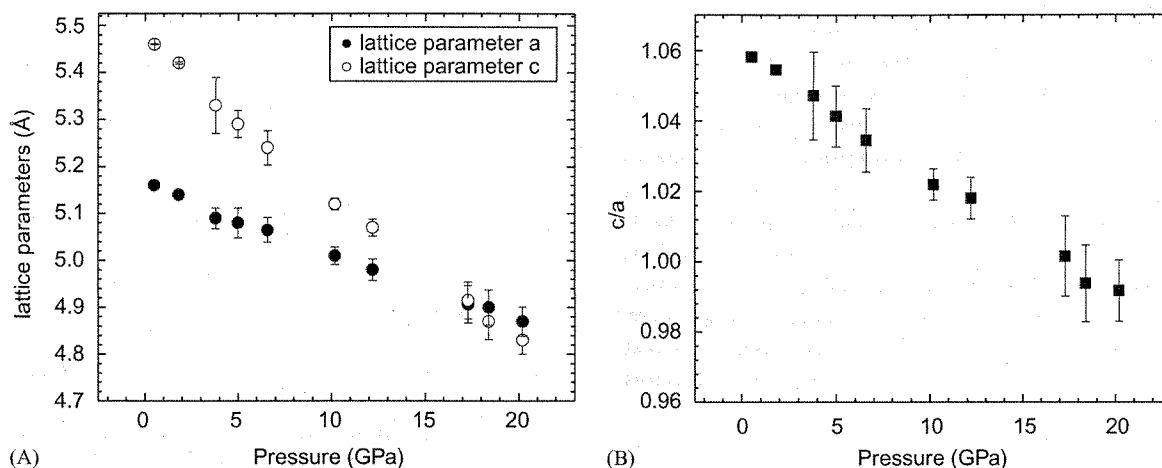


Fig. 5. (A) Pressure dependence of lattice parameters a and c of the hexagonal $\text{LiAlSi}_2\text{O}_6$ phase and (B) pressure evolution of c/a ratio.

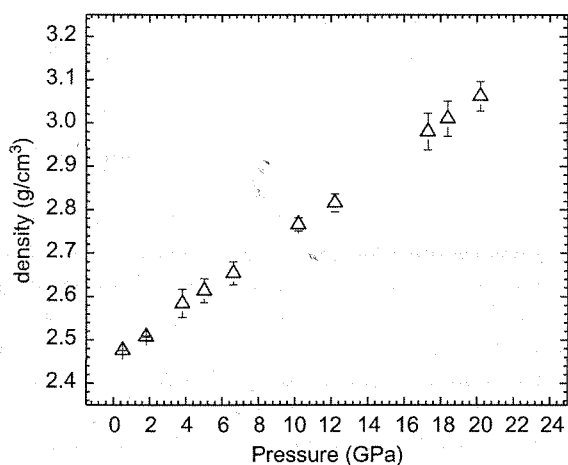


Fig. 6. Pressure evolution of the density of the $\text{LiAlSi}_2\text{O}_6$ phase. On compression from 0.2 to 20 GPa the calculated density of the $\text{LiAlSi}_2\text{O}_6$ phase increased by about 22%.

20 GPa, the calculated density of the $\text{LiAlSi}_2\text{O}_6$ phase increased by about 26%.

Volume was calculated from diffraction patterns up to 20 GPa only since above this pressure it was no longer possible to fit the crystal structure due to considerable line broadening. When pressure is applied to the glass–ceramic composite, the volume of nanocrystalline clusters gradually decreases, which results in a decrease of the unit cell volume to about 22%. This can be seen in Fig. 7

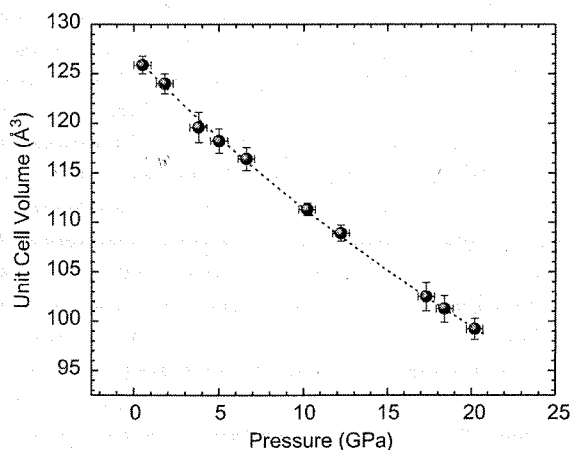


Fig. 7. Unit cell volume of the $\text{LiAlSi}_2\text{O}_6$ phase as a function of pressure, determined from the lattice parameters in the range from 0.2 to 20 GPa. The calculated decrease in the unit cell volume is about 22%. The dotted line is the Birch–Murnaghan [23] fit to the experimental data.

where the pressure dependence of the unit cell volume was determined from the lattice parameters on compression from 0.2 to 20 GPa.

In order to estimate the bulk modulus of the nanocrystalline phase the pressure–volume data was analyzed in terms of the Birch–Murnaghan [25] (Eulerian finite strain) equation of state:

$$F_V = K_0[1 - 1.5(4 - K'_0)f_V], \quad (1)$$

where f_V is the negative of the Eulerian strain measure

$$f_V = 0.5 \left[\left(\frac{V}{V_0} \right)^{-2/3} - 1 \right] \quad (2)$$

and F_V is the normalized pressure

$$F_V = P [3f_V(1 + 2f_V)^{2.5}]^{-1}. \quad (3)$$

The unit cell volume at zero pressure V_0 was measured to be $125.9 \pm 0.9 \text{ \AA}^3$. The pressure–volume data was recast as F – f and the intercept and slope of the data yielded, respectively, the bulk modulus K_0 and its pressure derivative K'_0 at zero pressure. The fit resulted in $K_0 = 71 \pm 2 \text{ GPa}$ and $K'_0 = 4.4 \pm 0.6$, and with K'_0 constrained to be 4, $K_0 = 114 \pm 7 \text{ GPa}$. For comparison the bulk modulus of commercially available glass–ceramic of similar composition is reported to be 60 GPa [26].

4. Conclusion

We performed in situ synchrotron X-ray diffraction studies of a lithium-aluminosilicate glass–ceramic composite with nanometer-sized $\text{LiAlSi}_2\text{O}_6$ crystals embedded in a host glass matrix. The endeavor of our investigations was to probe the effect of high-pressure compression on the nanocomposite structure and to acquire information on pressure-induced structural transformations that may occur in the lattice of the nanocrystalline phase. The pressure-induced evolution of X-ray diffraction patterns was followed in a diamond anvil cell on compression from 0.2 to 50 GPa and on consecutive decompression. In the compression sequence the observed shift of the diffraction lines assigned to the nanocrystalline $\text{LiAlSi}_2\text{O}_6$ phase indicated the linear compressibility of its lattice parameters accompanied by its progressive densification. At pressures above 20 GPa the diffraction patterns were significantly broadened and indicated a partial amorphization of the $\text{LiAlSi}_2\text{O}_6$ crystal lattice. With pressure increase on compression the patterns also revealed the presence of the ZrTiO_4 phase that was nucleated in the glass matrix before the crystal-

lization of the main nanocrystalline phase $\text{LiAlSi}_2\text{O}_6$. The diffraction pattern of the glass–ceramic composite quenched from 50 to 0.8 GPa illustrated that the high-pressure phase is at least partially retained on decompression although the decompressed structure still carried the signature of the initial ambient pressure $\text{LiAlSi}_2\text{O}_6$ phase. The pressure–volume data of the nanocrystalline phase ($\text{LiAlSi}_2\text{O}_6$) was analyzed in terms of the Birch–Murnaghan equation of state and yielded a zero pressure bulk modulus $K_0 = 71 \pm 2 \text{ GPa}$ and its pressure derivative $K'_0 = 4.4 \pm 0.6$.

Acknowledgements

The authors gratefully acknowledge the support from the U.S. Department of Energy Cooperative Agreement No. FC08-01NV14049 with the University of Nevada Las Vegas. We also thank the HPCAT staff at the APS for assistance in the measurements, especially Dr. Haozhe Liu for help with the X-ray diffraction experiments. HPCAT is a collaboration among the Carnegie Institution of Washington, Lawrence Livermore National Laboratory, the University of Hawaii, the University of Nevada Las Vegas, and the Carnegie/DOE Alliance Center. Use of the Advanced Photon Source is supported by the U.S. Department of Energy, Office of Science, Office of Basic Energy Sciences, under Contract No. W-31-109-Eng-38. Part of this work was done under financial support of the Advanced Research Institute for Science and Engineering, Waseda University, Tokyo (Japan). The authors acknowledge the Nippon Electric Glass Company, Kyoto (Japan) for technical advice and the use of their facilities for samples preparation.

References

- [1] Y. Wang, J. Ohwaki, Appl. Phys. Lett. 63 (1993) 3268.
- [2] P.A. Tick, N.F. Borrelli, L.K. Cornelius, M.A. Newhouse, J. Appl. Phys. 78 (1995) 11.
- [3] F. Auzel, K.E. Lipinska-Kalita, P. Santa Cruz, Opt. Mater. 5 (1996) 75.
- [4] M.J. Dejneka, J. Non-Cryst. Solids 239 (1998) 149.

- [5] C. Strohhofer, J. Fick, H.C. Vasconcelos, R.M. Almeida, *J. Non-Cryst. Solids* 226 (1998) 182.
- [6] A. Stepanov, D.E. Hole, P.D. Towsend, *J. Non-Cryst. Solids* 260 (1999) 65.
- [7] R. Ceccato, R. Dalmaschio, A. Gialanella, G. Mariotto, M. Montagna, F. Rossi, M. Ferrari, K.E. Lipinska-Kalita, Y. Ohki, *J. Appl. Phys.* 90 (2001) 2522.
- [8] J.P. Rueff, C.C. Kao, V.V. Struzhkin, J. Badro, J. Shu, R.J. Hemley, H.K. Mao, *Phys. Rev. Lett.* 82 (1999) 3284.
- [9] J. Zhao, G.R. Hearne, M. Maza, F. Laher-Lacour, M.J. Witcomb, T. LeBihan, M. Mezouar, *J. Appl. Phys.* 90 (2001) 3280.
- [10] J.Z. Jiang, J. Staun Olsen, L. Gerward, S. Mørup, *Europhys. Lett.* 44 (5) (1998) 620.
- [11] T. Li, H. Luo, R.G. Greene, A.L. Ruoff, *Phys. Rev. Lett.* 74 (1995) 5232.
- [12] S.H. Tolbert, A.P. Alivisatos, *J. Chem. Phys.* 102 (1995) 4642.
- [13] S.H. Tolbert, A.B. Herhold, L.E. Brus, A.P. Alivisatos, *Phys. Rev. Lett.* 76 (1996) 4384.
- [14] S.H. Tolbert, A.P. Alivisatos, *J. Chem. Phys.* 102 (1995) 4642.
- [15] K.E. Lipinska-Kalita, B. Chen, M. Kruger, Y. Ohki, J. Murowchik, E.P. Gogol, *Phys. Rev. B* 68 (2003).
- [16] K. Kim, S. Lee, H. Ahn, *J. Non-Cryst. Solids* 336 (2004) 195.
- [17] A. Hu, K. Liang, F. Peng, G. Wang, H. Shao, *Thermochim. Acta* 413 (2004) 53.
- [18] D.G. Cahill, J.R. Olson, H.E. Fisher, S.K. Watson, R.B. Stephens, R.H. Tait, T. Ashworth, R.O. Pohl, *Phys. Rev. B* 44 (1991) 12226.
- [19] B. Karmakar, P. Kundu, S. Jana, R. Dwivedi, *J. Am. Ceram. Soc.* 85 (2002) 2572.
- [20] A. P. Hammersley, FIT2D V10.3 Reference Manual V4.0., European Synchrotron Radiation Facility, Grenoble, 1998.
- [21] W. Kraus, G. Nolze, Powder Cell 2.4, Federal Institute for Materials Research and Testing, 12489, Berlin, Germany.
- [22] JADE Materials Data Inc., MDI XRD pattern processing software.
- [23] A.C. Larson, R.B. von Dreele, GSAS manual, Report LAUR86-748, Los Alamos National Laboratory, Los Alamos, 1988.
- [24] B.H. Toby, *J. Appl. Crystallogr.* 34 (2001) 210.
- [25] F. Birch, *J. Geophys. Res.* B-83 (1978) 1257.
- [26] Schott, <http://www.us.schott.com/>